DOCUMENT FLASH THERMOGRAPHY

by

Cory A. Larsen

A thesis submitted in partial fulfillment
of the requirements for the degree

of

MASTER OF SCIENCE

in

Electrical Engineering

Approved:

Dr. Doran J. Baker Major Professor	Dr. Gene A. Ware Committee Member
Dr. Todd Moon Committee Member	Dr. Mark R. McLellan Vice President for Research and Dean of the School of Graduate Studies

UTAH STATE UNIVERSITY
Logan, Utah

2011

Abstract

Document Flash Thermography

by

Cory A. Larsen, Master of Science

Utah State University, 2011

Major Professor: Dr. Doran J. Baker
Department: Electrical and Computer Engineering

This thesis presents the application of flash thermography techniques to the analysis of documents. The motivation for this research is to develop the ability to non-destructively reveal covered writings in archaeological artifacts such as the Codex Selden or Egyptian cartonnage. Current common signal processing techniques are evaluated for their effectiveness in enhancing subsurface writings found within a set of test documents. These processing techniques include: false colorization, contrast stretching, histogram equalization, median filtering, Gaussian low-pass filtering, layered signal reconstruction and thermal signal reconstruction (TSR), several contrast image definitions, differential absolute contrast (DAC), correlated contrast, derivative images, principal component thermography (PCT), dynamic thermal tomography (DTT), pulse phase thermography (PPT), fitting-correlation analysis (FCA), Hough transform thermography (PTHTa), and transmission line matrix fitting algorithm (TLMFa). New processing techniques are developed and evaluated against the existing techniques. The ability of flash thermography coupled with processing techniques to reveal subsurface writings and document strikeouts is evaluated. Flash thermography parameters are evaluated to determine most effective value for the document.

In summary, this thesis reports the following contributions to the existing scientific knowledge:

1. A comprehensive analysis of existing pulsed thermography processing techniques.
2. New pulsed thermography processing techniques that improve upon the results of the existing techniques were developed.
3. A proof-of-concept for detecting subsurface ink writings in documents.
4. Verifies the capability of pulsed thermography techniques to detect document strike-outs.
5. Demonstrates the ability to enhance surface writings based on differences in thermal characteristics when optical characteristics do not differ significantly.
6. Demonstrates that pulsed thermography significantly improves upon multi-spectral imaging for subsurface and surface writing enhancement.
7. Provides an evaluation of flash thermography parameters for the most effective document imaging.

(146 pages)

Acknowledgments

Special thanks to Pedro Sevilla and James Peterson of the Space Dynamics Laboratory for the use of their equipment and helping with the acquisition of the thermal images. Thank you to Dr. Gene A. Ware for his mentorship and guidance throughout the project. Thanks to Dr. Doran J. Baker of the Rocky Mountain NASA Spacegrant Consortium for funding the research and providing assistance as needed. Finally, thanks goes to Dr. Todd Moon and Dr. Jake Gunther of Utah State University for sharing their advice and expertise.

Cory A. Larsen

Contents

List of Tables

List of Figures

Acronyms

NDT&E	Non-destructive Testing & Evaluation
MSI	Multi-Spectral Imaging
IR	Infrared
PDF	Probability Distribution Function
DAC	Differential Absolute Contrast
TSR	Thermal Signal Reconstruction
PCT	Principal Component Thermography
PCM	Primary Contrast Mode
DTT	Dynamic Thermal Tomography
PPT	Pulse Phase Thermography
FCA	Fitting Correlation Analysis
PTHTa	Pulsed Thermography Hough Transform Algorithm
TLM	Transmission Line Matrix
TLMFa	Transmission Line Matrix Fitting Algorithm
TDC	Time-Difference Contrast
MF	Matched Filtering
THD	Total Harmonic Distortion
MEC	Markov Error Contrast
TCA	Time Constant Analysis
GUI	Graphical User Interface
NETD	Noise Equivalent Temperature Difference
SNR	Signal-to-Noise Ratio
MF	Matched Filter
SAM	Spectral Angle Map
ACE	Adaptive Coherence Estimator

Chapter 1

Introduction

1.1 General Background

Flash thermography, a subset of pulsed thermography or pulsed video thermography, is a technique used for non-destructive testing and evaluation (NDT&E) in a variety of materials, including concrete [1–3], high-density polyethylene [4], aerospace composites [5,6], wood and wood-based materials [7], and adhesive bond evaluation [8,9]. Flash thermography uses optical flash lamps to inject heat energy into a material. A high-speed infrared camera records the temperature of the material surface as the heat energy diffuses through the material. The video sequence is then processed to enhance the contrast of relatively "warm" (or "cold") areas on the surface that result from thermal reflections caused by material flaws.

Flash thermography was yet to be applied to documents or archaeological artifacts to reveal covered writings; for instance those found in the Codex Selden or Egyptian cartonnage [10]. The research presented in this thesis was used to develop the theory and application of flash thermography to documents, and lays a foundation for the application of this technology to archaeological artifacts in general. Development of flash thermography for this application provides the capability to non-destructively reveal covered writings — advancing the knowledge about ancient cultures without damaging irreplaceable artifacts.

1.2 Problem Statement

Motivation for this research derives from the desire to analyze ancient archaeological documents with a non-destructive approach. Specifically of interest is the imaging of subsurface writings that may be obscured with a layer of some type of material. Example ancient documents this technology could be applied to include, but are not limited to: palimpsests

from the Roman Empire, Mesoamerican codices, and Egyptian cartonnage. Another interest is the use of flash thermography for detection of textual changes, such as strikeouts, where older ink writings are covered with a more recent layer of ink writing. Finally, the ability of flash thermography to enhance contrast of surface writings through differences in thermal characteristics, rather than optical characteristics, are of interest.

1.3 Research Objectives

This thesis investigates the application of flash thermography to the textual analysis of documents. Areas of interest include revealing subsurface layers of writing, detecting textual changes such as document strikeouts, and enhancing surface writing through differences in materials properties between the ink and the document. A strong engineering basis is provided to facilitate the implementation of the investigations herein reported on other documents and archaeological artifacts. The scope of this research is limited to single-sided, optical flash thermography techniques and the corresponding processing algorithms.

Representative processing algorithms were chosen from the large body of flash thermography literature and applied to flash thermography images of documents with the effectiveness of each algorithm ascertained. In addition, unique new algorithms were investigated. This resulted in a determination of document types for effective application of flash thermography and a toolbox of processing techniques was collated.

A study was performed to evaluate the effectiveness of flash thermography in comparison with the multi-spectral imaging (MSI) standard. Attempts to validate the results were made using samples of Egyptian cartonnage and the Codex Selden. The results obtained are an important contribution to assist anthropology efforts in the non-destructive study of ancient documents. The accompanying graphics could provide significant value in the analysis and understanding of ancient cultures and societies.

1.4 Literature Review

The following literature review is split into two subsections which focus upon: (1) document imaging techniques, and (2) flash thermography processing techniques.

1.4.1 Document Imaging and MSI

Several imaging techniques have been developed to enhance the observation of surface writing and under-writing contained in archaeological artifacts. Infrared (IR) reflectography has been used in the analysis of paintings [11, 12] and papyrus [13]. The main application of IR reflectography is to view under-drawings beneath a layer of paint. With IR reflectography, a constant light source is used to excite the material. An IR imager captures an IR reflectogram detailing the different optical properties of the overlaying paint and the underwriting [14]. In addition to IR reflectography, transient thermographic techniques, including pulsed thermography, have also been used to analyze paint layers in artwork such as frescoes [15, 16] and general artwork [17–20]. A comparative study was performed comparing pulse thermography, lateral heating thermography, and modulated thermography for the analysis of frescoes [16]. Pulsed thermography was shown to be successful in areas where X-radiography, infrared reflectography, and UV examination had been unsuccessful [17]. Pulsed thermography has not yet been applied to the evaluation of ancient documents or other types of archaeological artifacts.

A common technique for analyzing ancient documents is multi-spectral imaging (MSI). MSI has been shown to be effective for enhancing contrast between underwriting, overwriting, and the document substrate [21,22]. MSI is performed by imaging documents in narrow spectral bands of light, allowing the spectral signature of the different document materials to be evaluated. Processing techniques for MSI images include, but are not limited to, the use of Markov random fields [21], spectral clustering [23], principal and independent component analysis [22], and linear spectral mixture analysis [22, 24].

The use of MSI has been successful in revealing obscured writing on the Archimedes palimpsest [24], carbonized scrolls [23], oxyrhynchus papyri [25], and the dead sea scrolls [26, 27]. MSI is most effective in enhancing the observation of writing that appears on or near the surface of the document. For example, the effectiveness of MSI to reveal the under codex within the Codex Selden was shown to be limited [28]. Another technique currently under investigation is X-Ray Fluorescence Imaging (XRF) [29].

1.4.2 Flash Thermography Processing Algorithms

A large body of processing techniques exist for enhancing defect contrast in pulsed thermography data. A thorough investigation of the literature revealed several techniques used for processing flash thermography data. Techniques include enhanced visualization through pseudo-color images [30, 31] and contrast stretching [32]. Spatial image noise reduction include techniques such as median filtering [30, 31, 33] and Gaussian low-pass filtering [30, 31, 33]. Synthetic signal reconstruction techniques are applied to reduce temporal noise and include layered signal reconstruction [34] and thermal signal reconstruction (TSR) [35, 36]. Several contrast image techniques include four contrast image definitions [30], differential absolute contrast (DAC) [37–39], and interpolated differential absolute contrast (IDAC) [40], as well as several similar techniques [41–43]. Analogies to modulated thermography techniques are made through pulse phase thermography (PPT) [44–50].

Other common processing routines include derivative images [33,35,36,45,51–55], principal component thermography (PCT) [56, 57], and dynamic thermal tomography (DTT) [58–60]. Correlation images [61, 62] are obtained by measuring the correlation coefficient between a measured and a desired signal. Hough transform thermography (PTHTa) [63,64] uses a parametric transform to aid in flaw detection. The transmission line matrix fitting algorithm (TLMFa) [65, 66] models thermal diffusion through transmission line theory to characterize material flaws.

Techniques that account for lateral diffusion include inverse scattering techniques [67–69], pulse-echo thermal imaging [70, 71], and point spread functions [72]. Other techniques include neural networks [30, 58, 73], Laplace transform techniques [64, 74] based on thermal quadropole theory [43, 75], flaw detection thermal tomography [58, 76], nonlinear fitting and optimization methods [58, 77, 78], adaptive thermal tomography [58, 79], and learning machines [80]. Image flaw segmentation [81] routines have been explored. In addition, several

tomographic techniques were developed based off the Algebraic Reconstruction Technique (ART) [82–84]; however, a raster-scan of the target using a laser for excitation is required.

Chapter 2

General Pulsed Thermography Considerations

2.1 Terminology

Throughout this thesis, the term *defect* is used in a manner consistent with current NDT&E literature. For applying flash thermography to documents, it is assumed that the ink under-writing can be treated as a defect in the document. Therefore, the terms defect and ink are used interchangeably throughout this research.

2.2 Instrumentation Requirements

Basic instrumentation requirements for performing pulsed thermography include a thermal viewer, an excitation source, and data collection and processing hardware [85]. Typical thermal imagers used in flash thermography applications are high-speed, mid-IR cameras. Using IR cameras, only qualitative thermograms are possible. Quantitative thermograms can be obtained using a radiometer; however, the present research is concerned only with the relative temperature differences between the area of interest and the rest of the document.

An excitation source is required for energy injection into the target sample. It is desired to generate a uniform thermal excitation across the entire surface of the sample. Pulsed sources include flash lamps and pulsed lasers. The present scope of work is limited to optical flash lamps as excitation sources.

The data collection and processing hardware usually consists of a computer to store the data and perform additional processing. However, some cameras include real-time processing within the camera itself. There are several existing software packages available for processing thermal data such as the Altair-Li suite provided by Cedip, RTools by FLIR, the ThermoFitPro software by Innovation Inc., and the open-source IR View Toolbox and GUI for Matlab [86].

A typical flash thermography setup is presented in Figure 2.1. Optical flash lamps provide the necessary energy which the document absorbs as heat and conducts through the document. Infrared energy is radiated from the surface and recorded by a high-speed infrared camera. In document sections containing ink underwriting, heat is reflected back to the surface creating a warm spot. The flash thermography video sequence is sent to a computer to process the images to increase defect visualization.

2.3 Flash Thermography Design Variables

Numerous considerations must be taken into account when applying flash thermography. These variables fall within four broad categories: 1) Characteristics of the thermal imager, 2) Thermal properties of target, 3) Characteristics of the transmitting medium, 4) Excitation source characteristics. Each of these categories are summarized [85].

2.3.1 Thermal Imager Characteristics

Evaluation characteristics of the thermal imager include:

Temperature Sensitivity: Also referred to as the minimum resolvable temperature or noise-equivalent temperature difference (NETD) [87], temperature sensitivity is the measure of the smallest temperature differences a camera is able to detect. The temperature sensitivity of the camera must be greater than the differential temperature

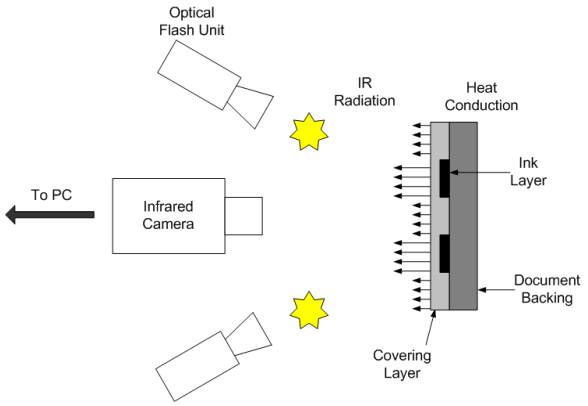

Fig. 2.1: Flash thermography setup.

signal indicating the difference in temperature between a defect-free region and a defect [88].

Image Acquisition Rate: The required image acquisition rate, also referred to as sampling rate or video frame rate, is dependent on the thermal diffusivity of the target material. A higher material thermal diffusivity requires a faster frame rate to properly capture the transient response of the thermal diffusion through the document. Defining τ as the time constant of the system, it can be assumed that a sampling rate of $f \geq \frac{10}{\tau}$ is sufficient [88].

Image Spatial Resolution: The image spatial resolution is a measure of the physical area an individual pixel views. A defect must have an area of at least one pixel in order to be detectable. Generally, the more pixels containing the defect the easier detection becomes.

Spectral Range: Spectral range specifies the wavelengths the camera is able to image. For flash thermography, the desired spectral range is either 2-5 μm or 8-12 μm. The spectral range of a camera can be limited using a bandpass filter [85].

Temperature Range: The temperature ranges determine the maximum and minimum temperatures that are detectable. This is important when there are large temperature differences due to defects or other objects with large differences in material properties in the field of view.

Total Field of View: The total field of view determines the area the camera is able to image at a time. The field of view must be large enough to image the region of interest.

Sensor Environment: The sensor environment includes the environmental properties of the experiment setup such as atmospheric temperature, pressure, humidity, or any other environmental variables that may affect the camera's ability to image properly.

2.3.2 Thermal Properties of the Target

Certain thermal properties of the target surface will affect the effectiveness of flash thermography. Properties to consider regarding the target surface include:

Thermal Emissivity: The thermal emissivity is a measure of the ability of the surface material to exchange thermal energy with its surroundings. Targets with high and uniform surface emissivity are most effective. The effects of surface emissivity non-uniformities can be reduced by differencing a pre-flash image from the data set. In addition, the surface can be coated with washable black paint to increase emissivity, although this is unfeasible for documents or archaeological artifacts [89].

Thermal Reflectivity: The reflectivity of the surface determines the amount of the initial energy impulse that will be absorbed. Low thermal reflecitivities indicate high amounts of energy absorption into the document from the excitation pulse. A target with a high reflectivity may introduce artifacts in the acquired images created by reflections from gray bodies surrounding the target. The thermal emissivity, reflectivity, and transmitivity of a surface are related through

$$\epsilon + \rho + \tau = 1, \tag{2.1}$$

where ϵ is the thermal effusivity, ρ is the reflectivity, and τ is the transmitivity [85].

Thermal Diffusivity: Thermal diffusivity is inversely proportional to the time constant for thermal diffusion through the target. The higher the thermal diffusivity, the less time it takes for the energy to diffuse through the document, thus requiring faster sampling rates (see Image Acquisition Rate). The lower the thermal diffusivity, the longer the total sampling time required. The total sampling time required to allow for diffusion to the back wall is specified by [90, 91]

$$t_{exp} = \frac{L^2}{\pi\alpha}, \tag{2.2}$$

where L is the thickness of the layer and α is the thermal diffusivity of the material.

2.3.3 Characteristics of the Transmitting Medium

Characteristics of the medium between the source excitation pulse and the target must be considered. In most cases the transmitting medium is air. In air, for short distances up to a few meters, these characteristics can be largely ignored. In addition, when imaging in the 3-5 μm range air is relatively free of significant spectral losses [85].

2.3.4 Excitation Pulse Characteristics

In this text, only pulsed excitation sources are considered. Characteristics of the input pulse such as amplitude, shape, and timing are now discussed.

Pulse Amplitude: The maximum amount of energy able to be inputted into the target has an upper limit determined by the temperature at which the material will begin to be damaged. This is checked when the sample temperature is maximal thus limiting either the amplitude or the duration of the excitation [88].

In order to detect a defect, or the back wall of the document structure, (Figure 2.2), the signal must be above the Noise Equivalent Temperature Difference (NETD), or stated another way, the temperature signal of a defect must have a signal-to-noise (SNR) ratio greater than 1 [88]. It is customary to define the minimum signal detection level to be a multiple of the NETD, with a rule of thumb SNR value of $n = 2$. The temperature difference needed to detect the back wall of the target is given as [87]

$$\Delta T_{wall} = n\sigma, \tag{2.3}$$

where $\sigma =$ NETD and n is the SNR value. The minimum energy required for detecting the back wall is given by

$$Q_{min} = n\sigma\rho CL, \tag{2.4}$$

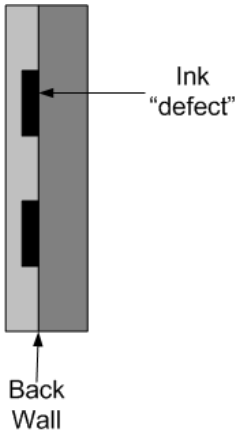

Fig. 2.2: Document structure.

where ρ is the density, C is the specific heat, and L is the thickness of the layer. Note that the thermal diffusivity does not affect the total energy requirement, however it does affect the running time of the experiment (see Thermal Diffusivity).

In order to observe a defect, the signal detection level must be an additional factor greater than the back wall detection level. Thus for a given signal level, $m\sigma$, and a detectability threshold, $n\sigma$, the maximum defect depth able to be detected is given by [87]

$$d_{max} = \frac{m}{m+n}L, m \geq n. \tag{2.5}$$

At the minimum energy level, Q_{min}, the deepest detectable defect is at a depth of $\frac{L}{2}$. The ability to detect deeper defects increases at a logarithmic rate with energy levels.

The amount of thermal energy absorbed by the target is dependent on several parameters, with a best case scenario found to be approximately 25% efficiency. Therefore, the flash electrical energy must be [87]

$$W_{electrical} \geq \frac{Q_{min} \times \text{Area}}{\text{Efficiency}}. \tag{2.6}$$

Note that these detection levels are for an idealized situation and represent a lower limit on energy requirements. However, the processing techniques discussed in Chapter 5 may facilitate defect detection up to and beyond these limitations.

Pulse Shape: The energy pulses inputted into the target are modeled as an impulse function or as a rectangular pulse. However, since the optical pulses are generated from a capacitor discharge, an exponentially decaying tail continues to input energy. This energy tail can obscure the first few frames of the sample surface. It was found that by using a flash controller to shorten the length of the tail, better temperature responses were obtained [92,93]. However, the shortening the tail reduces the amount of energy input into the target creating a trade off. The best results are obtained using the shortest pulse possible but still providing sufficient energy to the system. For low thermally conducive materials, it was shown that using a double pulse [94] or a train of pulses [95] could improve the signal-to-noise ratio leading to improved imaging.

Pulse Timing: Correcting for the timing offset between acquisition time and frame time increases correlation between modeled and experimental results [92]. The camera integration period can have a dramatic effect on the first frame. It was found that this effect could be minimized by using an integration period of less than the frame read-out period in combination with using the sample time measured from the heat pulse to the center of the integration period [92]. These pulse timing methods can often be difficult to accomplish in practice.

Chapter 3

Experiment Setup

3.1 Instrumentation Used

For the experiments performed in this thesis, a Lockheed-Martin/Santa Barbara Focal plane model SBF 180 thermal camera system was used with a custom data collection computer and software. The excitation energy pulses were provided by four SunPak Pro-System 622 Super optical flash units stationed on the sides of the target document. The camera was set horizontally on a table and aimed at an angled mirror. This mirror was used to image the test document laid flat on the surface of a table. Two camera filters were tested, a $3.42 - 4.05$ μm and a $2.65 - 3.24$ μm bandpass filter. Figure 3.1 shows the pulsed thermography test system.

3.2 Target Documents

Test documents were created to simulate challenges that occur in imaging ancient documents and other documents of interest. These documents fall into three broad categories: (1) subsurface imaging, (2) strikeouts, and (3) surface ink enhancement. Subsurface imaging

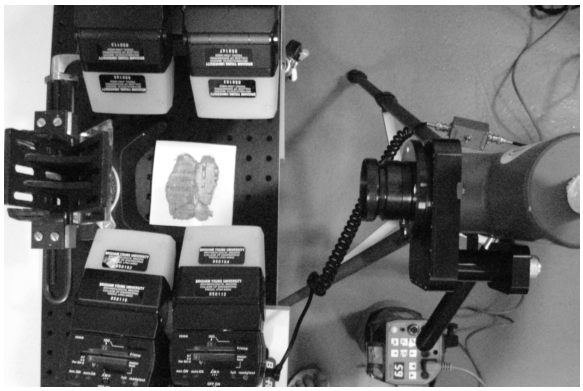

Fig. 3.1: Pulsed thermography test system.

refers to an attempt to image beneath a covering layer. Strikeouts refer to textual changes made to the surface of the target document where two layers of ink overlap. The last category, surface ink enhancement, refers to the attempt to enhance contrast of surface inks through differences in thermal characteristics between the ink and the document backing. Finally, a segment of Egyptian cartonnage was used to validate the method on an artifact of interest. Each of the document types are now discussed in detail.

3.2.1 Subsurface Imaging

There are several covering layers that are of interest to image beneath including papers, papyrus, a layer of mineral gesso, or a layer of paint. Imaging through the covering layer allows the ability to non-destructively reveal subsurface writing that cannot be observed without permanently damaging the document. Common documents of interest in this category are Egyptian cartonnage or pages in ancient manuscripts that have become permanently stuck together.

The mineral gesso covering layer contains a mixture of acrylics and calcium carbonate powder. This is motivated by documents such as the Codex Selden, a Mesoamerican palimpsest where the original codex was covered by a mineral gesso layer and a new codex drawn on the surface.

Imaging through a layer of paint will facilitate imaging Egyptian cartonnage, where old papyrus was used in the mummification process and decoratively painted over the existing writing. Other applications include imaging art works and frescoes.

Test documents were created using three inks applied in a pattern. The inks used were carbon-based, iron gall, and ball-point pen. Covering layers consisted of papyrus, card stock, gesso mixture, and oil-based paints.

3.2.2 Strikeouts

A strikeout test document was used to evaluate whether flash thermography techniques can detect textual changes within a set of writing. It is common in (ancient) documents for changes to be made to the original writing. MSI can be used to detect two layers of writing

that contains two different inks, but is not as effective when the over- and under-inks are spectrally similar. Dual layers of a carbon-based ink, an iron gall ink, a ball-point pen ink, and pencil lead were tested. In addition, a layer of white-out was used to determine the ability to image changes in modern documents and a layer of indentations were used to test surface inhomogeneities.

3.2.3 Surface Ink Enhancement

Surface ink enhancement is an attempt to reveal surface inks that are spectrally similar to the document backing. Detection using flash thermography may enhance the contrast of the inks with the surface through differences in material thermal properties. Ancient iron gall inks are known to fade in the infrared and lack significant spectral differences for MSI to properly enhance. The test document created consisted of a thin red and blue ink on a red card stock backing. Since the red and blue inks should be thermally similar, but spectrally different, it allows for a simple comparison between enhancement using flash thermography and MSI.

3.2.4 Egyptian Cartonnage

Flash thermography will be applied to a piece of Egyptian cartonnage. Used by the ancient Egyptians in the mummification process, cartonnage consists of scraps of papyrus or linen combined with a lime plaster similar to how modern papier-mâché is used. It was then molded into a desired shape and allowed to dry before being decoratively painted. Many of the scraps of papyrus used contained ancient writing that is of interest to scholars. The flash thermography techniques developed through using the test documents was applied to the Egyptian cartonnage in an attempt to reveal such hidden writing. The cartonnage provides a challenge for imaging because of its complex structure. Writings of interest may be buried beneath a layer of paint, gesso, papyrus, or a combination of each. The piece of cartonnage imaged is shown in Figure 3.2.

Fig. 3.2: Egyptian cartonnage.

Chapter 4

Processing Techniques

4.1 Background Theory

The majority of the algorithms herein presented process the image data on a pixel by pixel basis, evaluating the time series of each pixel separately without accounting for lateral diffusion. These time series represent the post-flash surface temperature decay of the material through time. It is often assumed that the diffusion into the material is significantly greater than the lateral diffusion and therefore the lateral diffusion can be neglected. This allows the diffusion into the document to be described using the equation for one-dimensional thermal diffusion as given by

$$\frac{\partial^2 T}{\partial x^2} = \frac{1}{\alpha}\frac{\partial T}{\partial t}, \tag{4.1}$$

where T is the temperature and α is the thermal diffusivity of the material. For an ideal impulsive heat flux, the response for a semi-infinite surface is [96]

$$T(x,t) = \frac{Q}{e\sqrt{\pi t}} e^{-\frac{x^2}{4\alpha t}}, \tag{4.2}$$

where $e = \sqrt{k\rho c}$ is the thermal effusivity of the material as determined by the thermal conductivity, k, mass density ρ, and specific heat c. Q is the quantity of energy absorbed by the surface. Time is represented by t and the depth into the material is given by x. Since the thermal imager can only respond to surface temperatures, (4.2) is evaluated at $x = 0$, resulting in the surface temperature decay modeled by

$$T_{surf}(t) = T(0,t) = \frac{Q}{e\sqrt{\pi t}}. \tag{4.3}$$

However, the thermal imager only gives relative temperatures, therefore let $\Delta T_{surf}(t) = T_{surf}(t) - T_{ambient}$, where $T_{ambient}$ is the pre-flash initial temperature of the sample. The response is thus more accurately described relative to the thermal imager as

$$\Delta T_{surf}(t) = \frac{Q}{e\sqrt{\pi t}}. \tag{4.4}$$

Equation (4.4) provides a basis for many of the algorithms discussed in this section. This equation can be further simplified to [54]

$$\Delta T_{surf}(t) = T_{init}\sqrt{\frac{T_s}{t}}, \tag{4.5}$$

where T_{init} is the value of the surface temperature at one time step, T_s, and is given by

$$T_{init} = \frac{Q}{e\sqrt{\pi T_s}}. \tag{4.6}$$

The techniques described throughout this section were implemented in MATLAB 2010b and a graphical user interface (GUI) was developed to aid in the implementation of the processing techniques. A tutorial for the GUI is given in Appendix A and the main algorithm code is given in Appendix B.

4.2 Existing Techniques

The theories behind several existing techniques used to enhance visibility and characterize material defects are outlined in the following sections.

4.2.1 Pseudo-Color Images

Human eyes contain two classes of light receptors: cones and rods. Cones are highly sensitive to color and are able to discern smaller changes in intensity than rods. This is due to the fact that cones, unlike rods, are connected to an individual nerve ending [31]. Therefore, it is useful to provide pseudo-color to the gray-scale intensity images obtained from the thermal cameras. These pseudo-color images are obtained through a process of

intensity slicing and color coding. Intensity slicing is a technique used to separate different intensity values in a gray-scale image. Given a gray-scale image with L intensity levels, the image can be separated into P intensity levels where $0 < P < L - 1$. By color coding the intensity values between regions, a pseudo-color image is created [31]. To avoid creating a mosaic effect within the image, it is better to use a continuous color map. However in some situations, choosing a discrete color mapping scheme may enhance the visibility of a particular feature [30]. Pseudo-color images can be created in MATLAB using the `colormap` command using the *jet* color map parameter.

Pseudo-colorization can be used as an aid to help enhance visualization of defects. Pseudo-colorization is often used as a pre-processing technique to analyze the data before processing. If no defects can be detected, even subtly, from a visual inspection then it is usually an indicator that the processing algorithms will not be able to effectively enhance any under writing. Pseudo-color images can also be used to aid in visualization of the post-processed images.

4.2.2 Contrast Stretching

Contrast stretching is a point processing technique used to expand the dynamic range of an image to increase visibility of image features. This technique is used to enhance visibility of the raw thermal images or as a post-processing step for the other techniques described in this section. The simplest form of contrast stretching is image normalization which is given by

$$I_N = (I - c)\left(\frac{b-a}{d-c}\right) + a, \tag{4.7}$$

where I is the input image with initial range $[c, d]$ and I_N is the normalized output image in the desired range $[a, b]$. Note that the normalization process is used on individual frames within the time sequence. Image normalization is greatly affected by dead pixels and other outliers in pixel values. To compensate, a useful technique is to saturate the top 1% and bottom 1% of pixels. This can be implemented with the MATLAB function `imadjust`.

4.2.3 Histogram Equalization

A histogram of a digital image is a discrete function that counts the number of pixels within given intensity level bins. The histogram is a discrete estimation of the probability density function (PDF) of the image. In histogram equalization, the goal is to transform the histogram of the input image into an output image with a uniformly distributed histogram. This technique enhances the global contrast of an image by adjusting the distribution of intensities within an image. If a defect lies in a region with low local contrast, histogram equalization will increase the contrast of that region allowing for enhanced defect visualization.

The transformation on each pixel intensity value is represented by

$$s = T(r), \tag{4.8}$$

where s is the equalized pixel value, r is the input pixel value, and $T(r)$ represents the transformation performed on r to obtain s. The transformation is given by [31]

$$s = T(r) = (L-1)\int_0^r p_r(w)dw, \tag{4.9}$$

where L represents the number of intensity levels and w is a dummy variable of integration. Equation (4.9) represents the cumulative distribution function of the image. It is proved elsewhere that this transform results in a uniform distribution [31].

For discrete digital images, the transformation function becomes

$$s_k = T(r_k) = \frac{L-1}{MN}\sum_{j=0}^{k} n_j \qquad k = 0, 1, 2, ..., L-1 \tag{4.10}$$

where MN is the total number of pixels in the image, and n_k is the number of pixels that have intensity r_k. A plot of n_k versus r_k results in the histogram of the image [31].

Since the histogram is a discrete approximation of the PDF and no new intensity levels can be created, perfectly flat histograms are rare in practical images [31]. Histogram

equalization can be implemented in MATLAB using the `histeq` function. The histogram equalization process is used to post-process the images after running the other algorithms described in this section or to better evaluate the raw, unprocessed images.

4.2.4 Image Filters

Two image filters have been found to be useful in noise reduction in flash thermography data, namely a median filter [31] and a Gaussian low-pass filter [30]. Median filters are useful for removing salt and pepper noise. The median filter is a nonlinear filter which ranks the pixels within a neighborhood, replacing the center pixel with the median of the intensity values. The median filter has advantages over a mean filter because it is not affected by outliers (such as those caused by dead pixels) and better preserves edges within the image. The median filter is common in imaging software and can be implemented in MATLAB using the `medfilt2` function.

The Gaussian filter is a frequency-domain filter that assumes the image has a limited bandwidth and any spatial frequencies above the given bandwidth are the result of noise. Since image noise tends to be characterized by high spatial frequencies, a low-pass filter can be used to reduce the noise content in the image. A derivation of the Gaussian filter for thermal images can be found elsewhere [30]. The Gaussian filter can be implemented in MATLAB using the `fspecial` command to create the filter and the `imfilter` command to apply the filter to the image.

4.2.5 Synthetic Signal Reconstruction Techniques

Two synthetic signal techniques were employed to reconstruct the signal, namely thermal signal reconstruction (TSR) [36, 52] and layered reconstruction (LR) [34]. Advantages of using reconstructed, synthetic data include (1) significant improvements in sensitivity, (2) a reduction of blurring, (3) increased depth range, (4) decreased memory requirements, and (5) improvements in signal-to-noise performance.

The TSR reconstruction processes each individual pixel's time sequence, rather than each frame as a whole. The time response data can be linearized by transforming to a

logarithmic domain. The logarithmic transform of (4.4) is

$$\ln\left(\Delta T_{surf}(t)\right) = \ln\left(\frac{Q}{e}\right) - \frac{1}{2}\ln\left(\pi t\right). \tag{4.11}$$

This implies that, regardless of the thermal properties of the material, the logarithmic decay response will be a straight line with a slope of $-\frac{1}{2}$ for an ideal, defect-free region. The linearized sequence can be modeled using a least-squares fit to a Nth order polynomial

$$\ln[\Delta T_{surf}(t)] = \sum_{n=0}^{N} a_n[\ln(t)]^n. \tag{4.12}$$

It was found that a fifth or sixth order polynomial effectively acts as a low-pass filter to smooth the data without reconstructing the noise [52]. The data can be reconstructed using [36, 52]

$$\Delta T_{surf} = \exp\left(\sum_{n=0}^{N} a_n[\ln(t)]^n\right). \tag{4.13}$$

In the layered reconstruction (LR) [34] algorithm, a multi-layered approach is taken. It is proposed that the signal can be reconstructed using the following equation:

$$T_{surf}(t) = T_f + \sum_{i=1}^{j} A_i e^{-\frac{t}{\tau_i}}, \tag{4.14}$$

where A_i is the amplitude of each exponential function and T_f is the steady-state temperature. The time constant of each layer is defined as $\tau_i = \frac{-1}{\alpha_i B_i^2}$, where α_i is the thermal diffusivity of the layer and B_i is determined by the boundary conditions. This approach can be further simplified by introducing normalized variables. Let ζ be the normalized time defined as

$$\zeta = \frac{t}{t_f}, \tag{4.15}$$

where t_f is defined as the time it would take the temperature to diminish 99.3%, or 5 time constants. Let θ be the normalized temperature difference, defined as

$$\theta = \frac{T_{surf}(0) - T_{surf}(t)}{T_{surf}(0) - T_{surf}(t_f)}. \tag{4.16}$$

Equation (4.14) can be normalized using the definitions of ζ and θ as follows:

$$\theta(\zeta) = 1 - \sum_{i=1}^{j} \beta_i e^{-\frac{\zeta}{\psi_i}}, \tag{4.17}$$

where $\beta_i = \frac{A_i}{T_{surf}(0) - T_{surf}(f)}$ and $\psi_i = \frac{\tau_i}{t_f}$. A least-squares method can be used to solve for the β_i and ψ_i of each layer, both of which are normalized between 0 and 1. The synthetic signal can be reconstructed using the fitted coefficients and (4.17).

In addition to performing a pure reconstruction, the synthetic signal can be modified. For example, the time points used to reconstruct the signal can be altered to effectively upsample, downsample, or interpolate the data [97].

4.2.6 Contrast Definitions

Four commonly used definitions of contrast are: absolute, running, normalized, and standard contrast. Each of the techniques are outlined below and are summarized [30]. The absolute contrast is defined as the excess temperature over a defect-free region at a given time t and is given by

$$C_{abs}(t) = T_{defect}(t) - T_{defectFree}(t), \tag{4.18}$$

where T is the temperature over a defect region and a defect-free region, respectively. This increases the contrast and improves the visibility of the defective region over the defect-free region.

The running contrast reduces the effects of differences in surface emissivities and is defined as

$$C_{run}(t) = \frac{C_{abs}(t)}{T_{defectFree}(t)}. \tag{4.19}$$

Note that if the contrast images are post-processed with the contrast stretching techniques given previously, then the absolute contrast and running contrast are the same.

The normalized contrast can be computed with respect to the end of the thermal process, at time t_{end}, or the time of temperature max, t_{max} (for pulsed thermography, this is the first frame). The normalized contrast is defined as

$$C_{norm}(t) = \frac{T_{def}(t)}{T_{def}(t_{max})} - \frac{T_{defectFree}(t)}{T_{defectFree}(t_{max})}, \tag{4.20}$$

where t_{max} can be replaced with t_{end}.

Finally, the standard contrast was developed to eliminate contributions from the surrounding environment by subtracting pre-flash information given at time t_0

$$C_{std}(t) = \frac{T_{defect}(t) - T_{defect}(t_0)}{T_{defectFree}(t) - T_{defectFree}(t_0)}. \tag{4.21}$$

Each of these contrast images requires selection of a defect-free area.

4.2.7 Differential Absolute Contrast (DAC)

The contrast methods described previously are greatly affected by non-uniform heating of the surface and requires selection of a defect-free area. Differential Absolute Contrast (DAC) [37] removes the need for manual selection of a defect-free area and is therefore more robust when non-uniform surface heating occurs. Let t' be the time at which the defect begins to appear in the sequence and $\Delta T(t)$ represent the frame at time t. Define the defect-free area as

$$\Delta T_{snd}(t') = \Delta T(t'). \tag{4.22}$$

From (4.2), the value of $\frac{Q}{e}$ can be solved to obtain

$$\frac{Q}{e} = \sqrt{\pi t'}\Delta T(t'). \tag{4.23}$$

Using this result in (4.2), the ideal defect-free area can be found as

$$\Delta T_{snd}(t) = \sqrt{\frac{t'}{t}}\Delta T(t'). \tag{4.24}$$

By the definition of the defect-free region combined with the definition of absolute contrast given in (4.18), the DAC image is given by

$$DAC(t) = \Delta T(t) - \sqrt{\frac{t'}{t}}\Delta T(t'). \tag{4.25}$$

Since the input pulse is not an ideal impulse, small differences in pulse length can be accounted for within different parts of the image. Defining t_e to be the amount of error in pulse length, a fit can be made in the logarithmic domain to find t_e and compensate for the error. The error-compensated DAC image is then found as

$$DAC(t - t_e) = \Delta T(t - t_e) - \sqrt{\frac{t' - t_e}{t - t_e}}\Delta T(t' - t_e), \tag{4.26}$$

where the values of t_e can vary over every pixel. The definition of the defect-free area can also be used with the other definitions of contrast given in Section 4.2.6. A technique called Interpolated Differential Absolute Contrast (IDAC) has been developed to remove the need for manual selection of time t' [40]. In addition, thermal quadrapole theory has been used to extend the validity of DAC to later times [41, 42].

4.2.8 Derivative Images

A defect can theoretically be detected without the use of a reference region by evaluating deviations from the ideal $-\frac{1}{2}$ slope seen in (4.11). To increase defect contrast and limit the effects of blurring caused by lateral diffusion, the derivatives of the analytical model for the data are taken. The derivatives facilitate detection of an earlier time of maximum contrast, thus reducing lateral diffusion blurring. However, the diameter of the subsurface defect must be greater than its depth beneath the surface for the lateral diffusion to be effectively ignored [51].

This algorithm begins by reconstructing the signal using the TSR technique described in Section 4.2.5 to obtain an analytical expression for the data. The pixel time histories are differentiated using the expressions [52]

$$\frac{d\ln(\Delta T_{surf}(t))}{d\ln(t)} = \sum_{n=0}^{N} n a_n \ln(t)^{n-1}, \tag{4.27}$$

$$\frac{d^2\ln(\Delta T_{surf}(t))}{d\ln(t)^2} = \sum_{n=0}^{N} n(n-1) a_n \ln(t)^{n-2}. \tag{4.28}$$

The reconstructed signal and its time derivatives are transformed into the linear time domain through (4.13) and by taking the exponent of the function as shown

$$\frac{d\Delta T_{surf}(t)}{dt} = \exp\left(\sum_{n=0}^{N} n a_n \ln(t)^{n-1}\right), \tag{4.29}$$

$$\frac{d^2\Delta T_{surf}(t)}{dt^2} = \exp\left(\sum_{n=0}^{N} n(n-1) a_n \ln(t)^{n-2}\right). \tag{4.30}$$

The resulting derivative time sequences can be outputted for analysis. Quantitative defect depth analysis can be estimated as described by Omar et al. [45, 53, 54].

4.2.9 Principal Component Thermography (PCT)

Principal Component Thermography (PCT) [56, 57] uses singular value decomposition (SVD) to reduce data to a compact statistical representation of the spatial and temporal variations relating the contrasts associated with underlying material defects [56]. In flash thermography data, a series of 2D image frames are stored sequentially, creating a 3D data set. In order to perform PCT, a raster-like operation must be performed to create a 2D representation of the 3D data. Given that the original data are loaded into an image cube with dimensions N_x, N_y, and N_t, where the N_x and N_y describe the pixel dimensions of each frame and N_t describes the number of frames. This image cube is then transformed into a matrix A with dimensions $M \times N_t$, where $M = N_x N_y$. The column vectors of M are standardized to correct for individual detector pixel characteristics. This standardization

is achieved through

$$\hat{A}(n,m) = \frac{A(n,m) - \mu_n}{\sigma_n}, \tag{4.31}$$

where

$$\mu_n = \frac{1}{N_t}\sum_{n=1}^{N_t} A(n,m), \tag{4.32}$$

$$\sigma_m^2 = \frac{1}{N_t - 1}\sum_{n=1}^{N_t} (A(n,m) - \mu_n)^2. \tag{4.33}$$

Any $M \times N$ matrix can be decomposed through Singular Value Decomposition (SVD) into the following elements

$$A = U\Gamma V^T, \tag{4.34}$$

where Γ is a diagonal matrix containing the singular values of matrix A, and U and V^T contain the left and right singular vectors of A. In this application, the matrix U contains a set of orthogonal basis functions that describe the spatial variations within the data and the matrix V^T contains the corresponding characteristic time behavior which can be used to estimate defect depths. By reversing the raster transformation applied to create A on U, the empirical orthogonal functions (EOF) of the data are produced.

An analysis was performed showing that the first two modes tend to contain 99% of the variance within the data, although some leakage occurs in the higher order modes [57]. The first mode describes a response similar to that of a uniform slab. However, the second mode, characterizes a non-uniform field created by material anomalies, and therefore has been named the primary contrast mode or PCM. A drawback of the original PCT algorithm is that it may enhance some defects at the cost of other defects [60]. The flaw depth may be estimated from the second principal component (PC), contained in the matrix V^T, and by knowing the thermal diffusivities of the material using the technique developed in [56, 98].

4.2.10 Dynamic Thermal Tomography (DTT)

Two versions of the DTT algorithm were implemented, those referred to as classical

DTT and as reference-free DTT [58–60]. The classical algorithm requires the selection of a reference, defect-free region. The frames are first normalized by dividing each frame with the first post-flash frame. The difference between the time sequence of each pixel and the reference signal is taken as

$$\Delta T(x, y, t) = T(x, y, t) - T_{ref}(t). \tag{4.35}$$

Two images can be created from the new ΔT signal: (1) an image of the maximum value of ΔT and (2) the time at which the maximum value occurs. These images are referred to as a maxigram and a timegram, respectively. This creates a synthetic image that is sampled at each pixel's "optimal" time. The corresponding transit times in the timegram can be used to create tomographic slices of the document.

The reference-free approach is similar to the classical approach, but removes the need for manual selection of the defect-free region. Instead, different order polynomials are fitted to the normalized temperature response. The low-order polynomial will only reflect general behavior of the material, whereas higher orders will include the behavior of defects. In this case, a third and a sixth order polynomial was used. The difference for each pixel can be found through

$$\Delta T(x, y, t) = T_h(x, y, t) - T_l(x, y, t). \tag{4.36}$$

The maxigram and timegram are obtained from $\Delta T(x, y, t)$ and outputted. Defect depths can be found using procedures described elsewhere [99].

4.2.11 Pulse Phase Thermography (PPT)

PPT is a combination of two forms of thermography, flash (pulse) thermography and modulated thermography. In flash thermography a pulse of heat energy is deployed into the target and the transient decay of the resulting surface temperature is analysed. Alternately, in modulated thermography the target is subject to a sinusoidal temperature stimulation in which standing thermal waves are created within the material. These standing thermal

waves are analyzed by their magnitude components and phase shifts with respect to the reference modulation. The magnitude images are proportional to local optical and infrared surface features; however, the phase shift images are relatively independent of these features. As a result, the phase images can probe roughly twice the thickness given by the magnitude image and are therefore the output of interest [46].

PPT uses the principle that a pulse of energy in the time domain contains all frequencies in the frequency domain. Since the input pulse is not an ideal delta function, but rather a rectangular pulse, the resulting frequencies are given by a sinc function [30]

$$F(f) = A_p T_s \ \mathrm{sinc}(\pi f T_s), \tag{4.37}$$

where f is the frequency variable, A_p is the pulse amplitude, and T_s is the sampling rate. In effect, all frequencies are analyzed simultaneously in PPT rather than at a single frequency as in modulated thermography [44]. In PPT, the discrete Fourier transform of each pixel's time series is computed using

$$F(u) = \frac{1}{N} \sum_{n=0}^{N-1} h(x) e^{-j2\pi ux/N} = R(u) + jI(u), \tag{4.38}$$

where $R(u)$ and $I(u)$ are the real and imaginary parts, respectively, of the transformed sequence, $F(u)$. The magnitude and phase responses are obtained from the transformed data through

$$\phi(u) = \tan^{-1}\left(\frac{I(u)}{R(u)}\right), \tag{4.39}$$

$$|F(u)| = \sqrt{R(u)^2 + I(u)^2}, \tag{4.40}$$

resulting in a series of magnitude and phase difference output images.

As previously stated, the phase images are usually of interest due to their relative independence of medium surface features. The resulting series of images correspond to frequencies ranging from 0 to $1/\Delta t$, where Δt is the time interval between images. The

lower the frequency, the deeper the image is able to probe. For the phase offset images, it was found most useful if the maximum phase offset, ϕ_{max}, was found for each pixel time history and outputted into a single resulting image [44].

Another form of PPT is computed using the Wavelet Transform (WT) in place of the Fourier Transform (FT). The advantage is that wavelets preserve time information of the signal and are correlated to defect depth, allowing quantitative evaluations [47, 48]. Another technique uses the Hough Transform to retrieve the blind frequencies, which are correlated with the defect depth [49]. It was also found that pre-processing the images with the reconstruction technique given in TSR improved the depth resolution of PPT [50].

4.2.12 Correlation Images

The fitting-correlation algorithm (FCA) [61] begins by reconstructing the signal using the technique specified in TSR (see Section 4.2.5). The reconstructed signals are then evaluated to see how closely they match either an "ideal" signal or a manually selected defect-free signal. The ideal signal can be found using (4.5) or (4.24). Two methods are used to evaluate the closeness of the fit, the correlation coefficient and the angle cosine. The correlation coefficient is calculated as

$$r = \frac{\sum_{i=1}^{n} (x_i - \bar{x})(y_i - \bar{y})}{\sqrt{\sum_{i=1}^{n} (x_i - \bar{x})^2 \sqrt{\sum_{i=1}^{n} (y_i - \bar{y})^2}}}, \tag{4.41}$$

and the angle cosine as

$$\cos\theta = \frac{\sum_{i=1}^{n} x_i y_i}{\sqrt{\sum_{i=1}^{n} x_i^2} \sqrt{\sum_{i=1}^{n} y_i^2}}. \tag{4.42}$$

The resulting correlation coefficient image and the angle cosine image are output.

The correlated contrast technique [62] builds upon the FCA algorithm. Klein argues that the chosen reference signal is irrelevant because differences can be adjusted for by changing the color map. In addition, it is noted that the dynamic range of the correlation coefficient image can be large, thus logarithmic color palettes are more appropriate than liner color palettes for visualizing the images [62]. The correlated contrast implemented in

the IR View toolbox uses a fifth order logarithmic root.

4.2.13 Transmission Line Matrix Fitting Algorithm (TLMFa)

The transmission line matrix is a numerical technique commonly used to model voltages transmitted within transmission lines and has been extended as a method to model forward diffusion. Transmission lines can be modeled using the lossy wave equation, or the telegrapher's equation, as given

$$\nabla^2 v = L_d C_d \frac{\partial^2 v}{\partial t^2} + R_d C_d \frac{\partial v}{\partial t}, \tag{4.43}$$

where $v = v(x, y, z, t)$ and represents the voltage, R_d, C_d, and L_d are the distributed parameters of a lumped transmission line and are the resistance, capacitances, and inductance. Now to begin applying this to thermal diffusion, interpret R_d and C_d as the thermal resistance and capacitance per unit length, respectively. Also let the voltage be analogous to the temperature $v = u$. By making appropriate space and time discretizations, the inductance term will disappear reducing (4.43) to

$$\nabla^2 u = R_d C_d \frac{\partial u}{\partial t}. \tag{4.44}$$

By defining $\alpha = \frac{1}{R_d C_d}$, the equation above can be rewritten as

$$\nabla^2 u = \frac{1}{\alpha} \frac{\partial u}{\partial t}, \tag{4.45}$$

which, letting α represent the thermal diffusivity, is the thermal diffusion equation describing heat flow. Thus, given small enough space and time discretizations, thermal diffusion can be modeled using the telegraphers equation where the voltage is equivalent to the temperature and the current is equivalent to the heat input. The only errors introduced are those imposed by the space and time discretizations [66].

The TLM algorithm can be based off two models for a transmission line, the T-network or Π-network models. These lead to two formulations of the TLM algorithm, referred to

as the link-line TLM node or link-resistor TLM node, respectively. Both methods achieve the same results but have different design approaches. The link-line nodal arrangement is derived in the following paragraphs. From the derivation above, the temperature is analogous to the voltage and the heat energy is analogous to the current. These analogies will be used for the rest of the derivation.

The transmission line can be seen as ideal segments of line with lumped resistance and capacitance. An impulse entering this line will travel unimpeded for time $\frac{\Delta t}{2}$ at which point it encounters a discontinuity. Some of this initial pulse will transmit on and part will be reflected back. This is determined by the reflection and transmission coefficients which are given by

$$\rho = \frac{R}{R+Z}, \tag{4.46}$$

$$\tau = \frac{Z}{R+Z}. \tag{4.47}$$

Assuming two input impulses are given approaching node x at time k. These pulses can be represented as ${}^{i}_{k}V_L(x)$ and ${}^{i}_{k}V_R(x)$ (the i indicates that it is incident on node x). The voltage at the node is given by the sum of the left and right bound pulses

$${}_{k}\phi(x) = {}^{i}_{k}V_L + {}^{i}_{k}V_R. \tag{4.48}$$

The incident pulses are then scattered using the transmission and reflection coefficients given above

$${}^{s}_{k}V_L = \rho\ {}^{i}_{k}V_L + \tau\ {}^{i}_{k}V_R, \tag{4.49}$$

$${}^{s}_{k}V_R = \tau\ {}^{i}_{k}V_L + \rho\ {}^{i}_{k}V_R. \tag{4.50}$$

The scattered pulse then travel along the line until they become incident on adjacent nodes

$${}^{i}_{k+1}V_L(x) = {}^{s}_{k}V_R(x-1), \tag{4.51}$$

$$ {}^{i}_{k+1}V_R(x) \quad = \quad {}^{i}_{k}V_L(x+1). \tag{4.52} $$

The process of summation (4.48), scatter (4.50), and connect (4.52) are repeated to create the link-line TLM algorithm.

Using a least squares fitting method, such as the Levenberg-Marquardt Method, the TLMFa algorithm can be applied to each individual pixels time response sequence and the reflection coefficients can be determined. Since the reflection coefficients are dependent on the thermal properties of the material, outputting images created from the each pixel's reflection coefficient for each node provides a characterization of a defect.

4.2.14 Hough Transform Thermography (PTHTa)

The Hough transform is a geometrical transform that is used in image processing to find geometrical structures within an image. The Hough transform is represented by

$$ \rho = x\cos\theta + y\sin\theta, \tag{4.53} $$

where the points (x, y) are transformed into the Hough space (ρ, θ). The pulse thermography Hough transform algorithm (PTHTa) [63,64] uses the Hough transform to evaluate thermal sequences removing the need for an operator by identifying pixels that follow the -$\frac{1}{2}$ slope shown in (4.11). Each point is transformed pixel-wise into sinusoidal curves in the Hough space. The Hough space acts as an accumulator that sums the votes of all pixels in the sequence providing an indication of the points that follow a -$\frac{1}{2}$ slope. The points that correspond to a -$\frac{1}{2}$ lie in the $\theta \approx 1.1071$ rad column in Hough space [63]. By analyzing the distribution of values in the $\theta \approx 1.1071$ rad column, defective areas can be separated from non-defective areas. This is accomplished by performing a least-squares fit of an exponential function of the form

$$ \zeta(x) = ae^{\left(\frac{x-b}{c}\right)}. \tag{4.54} $$

It has been shown that parameters a and c are highly correlated to the defect depth and

images created from these parameters effectively enhance the contrast between the defect-free and defect regions [63].

4.3 Developed Techniques

In an attempt to improve upon the existing techniques, the following techniques were developed theoretically and algorithms developed to implement each. A description of each technique follows.

4.3.1 Time-Difference Contrast

Time differencing allows for the subtraction of two frames that occur at different times in order to analyze temperature changes between frames. This allows for the analysis of relative changes in temperature between frames. Due to the decay of temperature between time frames, it is assumed that for a defect-free image, the two frames would be related by a multiplicative scale factor α.

$$I_{t_1} = \alpha I_{t_2}, \tag{4.55}$$

where I_{t_1} and I_{t_2} are the images at times t_1 and t_2, respectively. It is assumed that image I_{t_1} is chosen such that the defect has not appeared yet, and could be either a pre-flash image or an image immediately post-flash. Also, it is assumed that image I_{t_2} is an image when the defect has begun to appear. The scale factor α can be determined using a minimum mean square error (MMSE) method to solve

$$\alpha = \min_{\alpha} ||\alpha I_{t_2} - I_{t_1}||. \tag{4.56}$$

After determining α, the two images are then differenced

$$I_d = \alpha I_{t_2} - I_{t_1}, \tag{4.57}$$

where I_d is the difference image or contrast mask. Since the MMSE technique will minimize the average error of the images, I_d will be positive for areas where defects appear and

slightly negative in areas where the defect does not appear. This method can be used to difference two specified images of interest. An automated method found to be effective is to select the images to difference based on the time relation

$$t_2 = t_1 + n \times T_s, \tag{4.58}$$

where n is an integer and T_s is the sampling rate. A value of $n = 5$ was found to be sufficient in most applications.

4.3.2 Total Harmonic Distortion (THD)

Total harmonic distortion is an idea borrowed from microelectronics and quantizes the amount of harmonic distortion, or noise, in a signal. THD can be defined as the ratio of the sum of powers to the power of the fundamental frequency.

$$THD_P = \frac{\sum_{n=2}^{\infty} P_n}{P_1} = \frac{\sum_{n=2}^{\infty} V_n^2}{V_1^2}, \tag{4.59}$$

where P_n and V_n represents the power and voltage of the nth harmonic, respectively. An alternative measure of harmonic distortion is given by amplitude ratio rather than the power ratio and is defined by

$$THD_A = \frac{\sqrt{\sum_{n=2}^{\infty} V_n^2}}{V_1}. \tag{4.60}$$

To apply this to flash thermography, first inspect the Laplace transform of an ideal diffusion as given by (4.4). The Laplace transform is

$$F(s) = \frac{Q}{e\sqrt{\pi}} \frac{\Gamma(0.5)}{\sqrt{s}}. \tag{4.61}$$

By defining $C = \frac{\Gamma(0.5)}{2\sqrt{\pi}} \frac{q}{e}$, (4.61) can be rewritten as

$$F(s) = C \frac{1}{\sqrt{s}}. \tag{4.62}$$

This is the frequency response of an ideal, defect free region. Treating thermal reflections

due to defects back to the surface as noise, the amount of noise can be quantized using THD resulting in a measurement of the degree in which a subsurface defect causes a deviation from the defect-free response. From inspection of (4.62), the fundamental frequency is chosen as the first frequency off zero. Using both definitions of THD as given by (4.59) and (4.60), the extent which a subsurface defect causes deviations from an ideal response can be measured. Note that by dividing by the first harmonic effectively normalizes the images and thus is not affected by differences in surface emissivities.

In addition to the THD, an alternate definition of signal-to-noise ratio can be calculated as

$$SNR = \frac{\mu}{\sigma}, \tag{4.63}$$

where μ and σ are the mean and standard deviation in the frequency domain. The resulting images tend to have a high spatial frequency and can be improved by using the image filters described in Section 4.2.4 or by using a 2D Weiner filter.

4.3.3 Markov Error Contrast (MEC)

In MEC, each individual pixel's time sequence is treated like a Markov chain, where the next temperature in time is only a function of the current temperature. Recall (4.5) describes the simplified response of a homogeneous slab given an impulse. Modifying this equation, it can be shown that the next point is equal to

$$T_{est} = T_{current}\sqrt{\frac{t_c}{t_c + T_s}}, \tag{4.64}$$

where T_{est} is the estimated next temperature state at time $t_c + T_s$, $T_{current}$ is the measured current temperature state, t_c is a scalar of the current time, and T_s is the sampling rate. The next temperature state is then estimated until every point has been evaluated and a synthetic signal has been reconstructed. Note that every estimation is based off the current measured value, not the estimated value for the current state. The error between the actual

and the estimated values for the entire sequence is found

$$E(t) = T(t) - T_{est}(t). \tag{4.65}$$

The value of $E(t)$ can be output for each pixel, creating a series of error images containing the difference between the actual data and the Markov estimation.

4.3.4 Time Constant Analysis (TCA)

The TCA algorithm is based off the apparent exponential decay of the thermal sequence. It performs a least-squares fit of the temperature decay data to the model

$$T_{surf} = ae^{\frac{-t}{\tau}} + c \tag{4.66}$$

to describe the cooling of each pixel through time, where T_{surf} represents the pixel temperature at time t. The pixel's rate of decay is described by the parameter τ, the pixel's time constant. An output image of each pixel's time constant is created. Areas with defects will have a slower time constant than sound regions.

4.3.5 Signal Detection and Matched Filtering (MF)

Matched filtering is used to increase visibility of defect areas while minimizing the visibility of defect-free areas thus increasing the contrast of the material defects. Matched filtering has been successfully used in MSI images to combine information across spectral bands and enhance surface writings in ancient documents [100]. The method derived below has been adapted and summarized [100, 101].

The MF technique is based off the following model

$$T_{obs} = \epsilon\, T_{refl} + T_{ideal}, \tag{4.67}$$

where T_{obs}, T_{ideal}, and T_{refl} is the observed temperature decay sequence, the ideal temperature decay sequence of a defect-free area, and the temperature profile caused by reflections

from defects, respectively. The value ϵ is indicative of the strength of the reflected signal. To simplify notation on the derivations that follow, (4.68) is rewritten as

$$\mathbf{x} = \epsilon\mathbf{s} + \mathbf{w}, \tag{4.68}$$

where $\mathbf{x} = T_{obs}$, $\mathbf{s} = T_{refl}$, and $\mathbf{w} = T_{ideal}$, where the bold font represents vectors. This model requires a known temperature decay profile for a defect-free region. This can be achieved by having an operator manually choose a defect free region. The matched filtering techniques that follow multiply (4.68) by a vector $\mathbf{q}$ that maximizes the influence from the reflected temperature and minimizes the defect-free response. The determination of $\mathbf{q}$ is determined by the constraints

$$\max_{\mathbf{q}} ||\mathbf{q}^T\mathbf{s}||_2 \text{ subject to } \min_{\mathbf{q}} ||\mathbf{q}\mathbf{w}||_2. \tag{4.69}$$

All of the matched filter detectors accomplish the objective above, but use different methods in determining $\mathbf{q}$. The different matched filter detectors are outlined in the following paragraphs. For each of the filters, a known reflection sequence, T_{refl}, and the ideal temperature sequence, T_{ideal}, must be known. As previously stated, T_{ideal} can be determined by an operator choosing a background pixel or by using (4.5). Obtaining T_{refl} can be a difficult, however the following method is proposed. First, the target pixels must be selected. Then T_{refl} is calculated by subtracting the ideal response from the observed response leaving only the response from the reflection

$$T_{refl} = T_{obs} - T_{ideal}. \tag{4.70}$$

It was found that when an operator picked a signal, better signal-to-noise (SNR) ratio was obtained if several signals were picked and the results were averaged. Several matched filtering methods were implemented and the effectiveness of each evaluated.

The simplest matched filter technique is the **Simple Matched Filter (SMF)**. The SMF detector uses the known T_{refl} sequence as $\mathbf{q}$. This provides a correlation between the

known reflection response and the observed temperature profile of each pixel, resulting in a correlation image. The resulting SMF image is defined as

$$\text{SMF} = \mathbf{s}^T \mathbf{x}_{ij}, \tag{4.71}$$

where the subscript i, j indicate the process is repeated over all the pixel's time sequences to create a single resulting image.

The **Spectral Angle Map (SAM)** detector builds upon the SMF detector through normalizing by the vector magnitudes of the target and observed signals. The resulting SAM image is given by

$$\text{SAM} = \frac{\mathbf{s}^T \mathbf{x}_{ij}}{\sqrt{\mathbf{s}^T \mathbf{s}} \sqrt{\mathbf{x}_{ij}^T \mathbf{x}_{ij}}}. \tag{4.72}$$

The SAM image is the cosine of the angle between $\mathbf{s}$ and $\mathbf{x}$. Note the SMF and SAM images are similar in concept to the correlation techniques described in Section 4.2.12.

The **Clutter Matched Filter (CMF)** technique incorporates information arising from the document structure by introducing the covariance matrix C. A derivation of this filter using the probabilities of a defect-free and a defect containing region using the Likelihood Ratio Test to develop a threshold on target presence is shown elsewhere [101]. The CMF image is given by

$$\text{CMF} = \mathbf{s}^T C^{-1} \mathbf{x}_{ij}, \tag{4.73}$$

where C is the covariance matrix of the ideal diffusion process

$$C = \frac{1}{m} \sum_{i=1}^{m} \mathbf{w}\mathbf{w}^T. \tag{4.74}$$

The **Adaptive Coherence Estimator (ACE)** builds upon the CMF by normalizing by the vector magnitudes, similar to how SAM builds upon SMF.

$$\text{ACE} = \frac{\mathbf{s}^T C^{-1} \mathbf{x}_{ij}}{\sqrt{\mathbf{s}^T C^{-1} \mathbf{s}} \sqrt{\mathbf{x}_{ij}^T C^{-1} \mathbf{x}_{ij}}} \tag{4.75}$$

The **Matched Subspace Filter (MSF)** is used to detect subsurface defects that may have different intensity reflections or when detecting different subsurface defects but want a single statistic to analyze the entire image. The matrix H is formed, where the columns of H are the chosen target signals

$$H = [\mathbf{s_1}, \mathbf{s_2}, \mathbf{s_3}, ..., \mathbf{s_n}]. \tag{4.76}$$

The measurement of energy of the observed signal projected into the target space, H can be shown to be

$$\text{MSF} = \mathbf{x}^T H(H^T H)H^T \mathbf{x}. \tag{4.77}$$

The **t-statistic** and **F statistic** methods come from regression literature and the derivations for both can be found elsewhere [101]. The t-statistic is simply the square root of the F statistic. The equations for both are shown

$$\text{tstat} = \frac{\mathbf{s}^T R^{-1}\mathbf{x}_{ij}}{\sqrt{\mathbf{x}_{ij}^T R^{-1}\mathbf{x}_{ij} - \rho^2(\mathbf{s}^T R^{-1}\mathbf{x}_{ij})^2}}\rho\sqrt{d-1}, \tag{4.78}$$

$$\text{Fstat} = \frac{(\mathbf{s}^T R^{-1}\mathbf{x}_{ij})^2}{\mathbf{x}_{ij}^T R^{-1}\mathbf{x} - \rho^2(\mathbf{s}^T R^{-1}\mathbf{x}_{ij})^2}\rho^2(d-1), \tag{4.79}$$

where $\rho = \frac{1}{\sqrt{s^T R^{-1} s}}$.

Other matched filter definitions implemented include: the **Distance Matched Filter (DMF)** given by

$$\text{DMF} = \frac{(\mu_s - \mu_b)^T R_b^{-1}(x - \mu_b)}{(\mu_s - \mu_b)^T R_b^{-1}(\mu_s - \mu_b)}, \tag{4.80}$$

the **Constrained Energy Minimization (CEM)** given by

$$CEM = \frac{s^T \Gamma_x^- 1 x_{ij}}{s^T \Gamma_x^{-1} s}, \tag{4.81}$$

and the **Minimum Variance Distortionless Response (MVDR)** is given by

$$MVDR = \frac{(s - \mu_x)^T R_x^{-1}(x - \mu_x)}{(s - \mu_x)^T R_x^{-1}(s - \mu_x)}. \tag{4.82}$$

In addition, other signal detection techniques were implemented such as **RX Anomaly Detection (RX)**

$$\text{RX} = (\mathbf{x} - \mu_b)^T R_b^{-1} (\mathbf{x} - \mu_b), \tag{4.83}$$

the **Quadratic Detector**

$$\text{QD} = (\mathbf{x} - \mu_b)^T R_b^{-1} (\mathbf{x} - \mu_b) - (\mathbf{x} - \mu_s)^T R_s^{-1} (\mathbf{x} - \mu_s), \tag{4.84}$$

and **Quadratic Discriminant Analysis (QDA)**

$$QDA = -\frac{1}{2} \log |R_s| - \frac{1}{2} (x_{ij} - \mu_s)^T R_s^{-1} (x_{ij} - \mu_s). \tag{4.85}$$

Derivations for these techniques can be found elsewhere [100–102]. Each of these techniques were implemented, and evaluated for their effectiveness in processing flash thermography data.

4.3.6 Convex Optimization Signal Detection Technique

In addition to the signal detection techniques described above, a technique using convex optimization was attempted. Let every pixel, $x^i(t)$, be composed of an ideal base signal $c(t)$ and a sum of reflection signals $h(t)$ such that

$$x(t)^i = \sum_{k=0}^{L} a_k h(t-k) + bc(t), \tag{4.86}$$

where b is a scaling factor on c and a_k is a sparse matrix of filter coefficients. Re-writing (4.86) in vector notation

$$\mathbf{x}^i = \mathbf{H}\mathbf{a}^i + \mathbf{e}^i, \tag{4.87}$$

where $\mathbf{e}^i$ is the error,

$$\mathbf{x}^i = [\ \mathbf{c}\ \mathbf{h}(0)\ \mathbf{h}(1)\ ...\ \mathbf{h}(n)\ ], \tag{4.88}$$

and $\mathbf{H}$ consists of a matrix of target vectors. The sparse matrix $\mathbf{a}^i$ can be solved for by

$$\min ||\mathbf{a}^i||_1 \quad \text{subject to} \quad ||\mathbf{H}\mathbf{a}^i - \mathbf{x}^i||_2 \leq \epsilon, \tag{4.89}$$

where ϵ is the allowed error. The values of $\mathbf{a}$ can be shown for every pixel sequence, creating n coefficient images. The values contained in $\mathbf{a}$ will indicate the strength of the target signal.

The difficulty with this method is determining the target signals to fill the $\mathbf{H}$ matrix with. Several options include manual selection of signals, randomly choosing signals, or creating reflection signals from finite element solutions (every unique structure would need to be simulated). This technique is still under development and the results are not included in this thesis.

Chapter 5

Analysis of Results

5.1 Processing Techniques Results

Each of the algorithms discussed in Chapter 4 were implemented and the effectiveness of each was evaluated. Since it is difficult to define general quantitative measures for image quality, subjective measures of effectiveness were used with conclusions developed from the experience of processing a variety of document structures presented. Representative images were chosen to include in this report; however, the conclusions are generalized based upon the experience of processing a variety of constructed data sets using various parameters. Each of the algorithms studied were developed for, and perform best on, homogeneous single-layer materials. Since ancient documents are often constructed with a variety of materials and may have multiple layers, the evaluations were focused on the effectiveness of processing complex structures.

The chapter is split into several parts. First, each technique is applied to a sample data set and the imaging results showing the effectiveness in revealing subsurface inks are presented. Next, techniques which prove applicable to document strikeouts and surface writing enhancement are reviewed. Finally, comparisons are made between the effectiveness of flash thermography and MSI for a variety of test documents. The results presented throughout this chapter will be summarized in Chapter 6.

5.1.1 Subsurface Inks

Throughout this section, several images are presented demonstrating and comparing the effectiveness of the processing routines. The constructed data set used for this technique comparison is given in Figure 5.1. The example document was constructed by using an

adhesive to thermally bond the card stock sheet in Figure 5.1(a) to the card stock sheet in Figure 5.1(b), with the surfaces containing the ink bonded together. Note that Figure 5.1(a) has been mirrored in order to reflect the direction the ink would face when the layers are glued together. Each processing technique will be applied to the flash thermography data of Test Document 1 and the results discussed.

Noise Reduction

Several techniques were used in reducing noise within the images. A median filter was used to remove salt-and-pepper noise. A low-pass Gaussian filter was used to remove high spatial frequency content that is often a result of noise. Finally, temporal noise was reduced using either the thermal signal reconstruction (TSR) or the layered reconstruction (LR) synthetic signal techniques.

It was found that using a 3×3 filter window was sufficient for both the median and the Gaussian filter approaches. In addition, a variance of approximately 0.8 was found to be effective for the Gaussian filter. Finally, the thermal signal reconstruction was found to be preferred over the layered reconstruction.

Although both generally reconstructed the signal adequately, the TSR method was found to be computationally faster (see Table 5.1) and generally reconstructed the signal as good or better than the LR method. For the TSR method, using a sixth order polynomial fit appeared to give sufficient results. In LR, a minimum of three layers were usually required

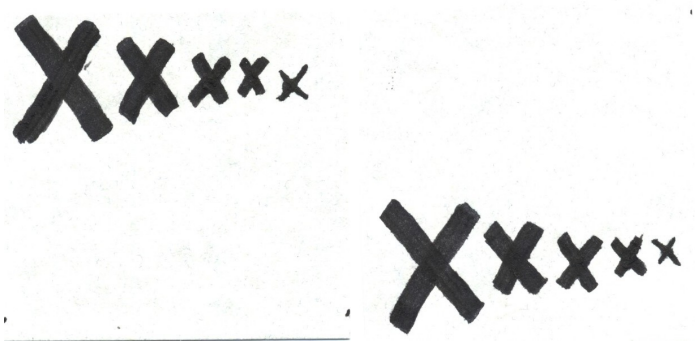

(a) Top Side (Mirrored) (b) Bottom Side

Fig. 5.1: Test document 1.

to give an accurate reconstruction; however, using more layers increased the accuracy (and computation time) of the reconstructed signal. Figure 5.2 shows the results of the noise reduction process. Note that these images have been normalized to increase contrast.

The images presented throughout this chapter and in Figure 5.2, unless specifically stated otherwise, were pre-processed using the median filter, followed by the low-pass Gaussian filter, followed by the TSR reconstruction. This approach appeared to be the more effective order for application of the noise reduction techniques.

Pseudo-Color Images

Figure 5.3 present the use of pseudo-color images on a sample raw frame. In Figure 5.3(a), very little ink information can be detected. However, using pseudo-color, as shown in Figure 5.3(b), the flaw information can be faintly observed. Consistent with the literature [30], it was found that using a continuous color map was most effective for this application. Pseudo-color images can be used to evaluate the unprocessed frames (as shown in Figure 5.3) or to better visualize the processed data. It was found useful to evaluate the thermal images in both pseudo-color and grayscale.

Contrast Stretching and Enhancement

The techniques discussed in this section, such as image normalization and histogram

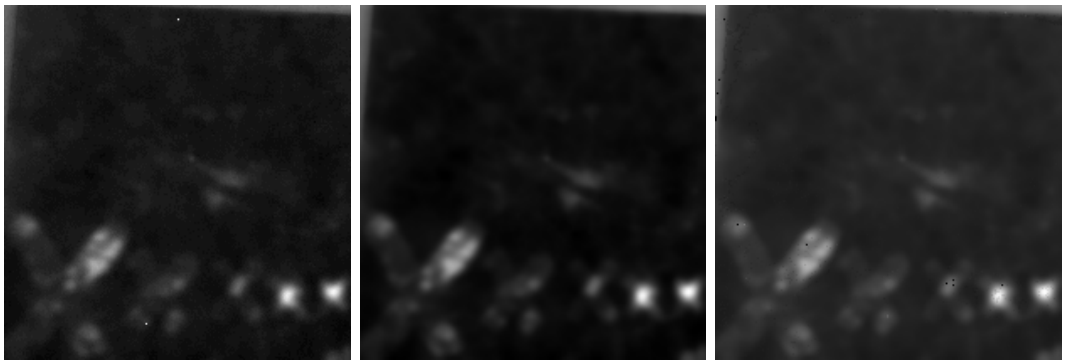

(a) Raw (b) Thermal Signal Reconstruction (TSR) (c) Layered Reconstruction (LR)

Fig. 5.2: Noise reduced images at $t = 228.8$ ms.

Table 5.1: Signal reconstruction wall times.

Algorithm	Wall Time (sec)
TSR	19.12
LR 3	900.3
LR 4	1638

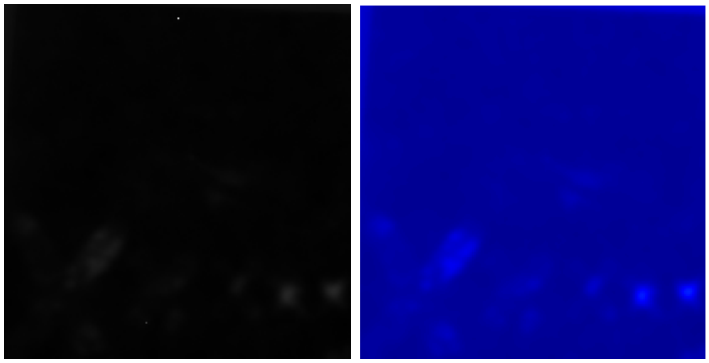

(a) Original (b) Pseudo-Color

Fig. 5.3: Pseudo-color image at $t = 228.8$ ms.

equalization, can be used to successfully process the raw images. However, the thermal-based processing algorithms discussed in the following sections usually provide better defect visualization. The advantage of contrast stretching techniques is highest when used as a post-processor to the thermal techniques discussed later.

Figure 5.4 compares the results of the same frame contrast enhanced using normalization, normalization with end saturation, and histogram equalization. An increased amount of subsurface ink is observed in Figure 5.4 compared with the non-contrast enhanced image shown in Figure 5.3(a). Figure 5.4(c) demonstrates that histogram equalization can be a very useful image enhancement technique; unfortunately, undesirable image deformations may occur.

Contrast Definitions and Differential Absolute Contrast

The Differential Absolute Contrast (DAC) technique was found to be a very effective contrast technique, depending on differential frame, t', selected. The advantage of this technique is that by choosing t' values relating to defects at different depths, specific defects

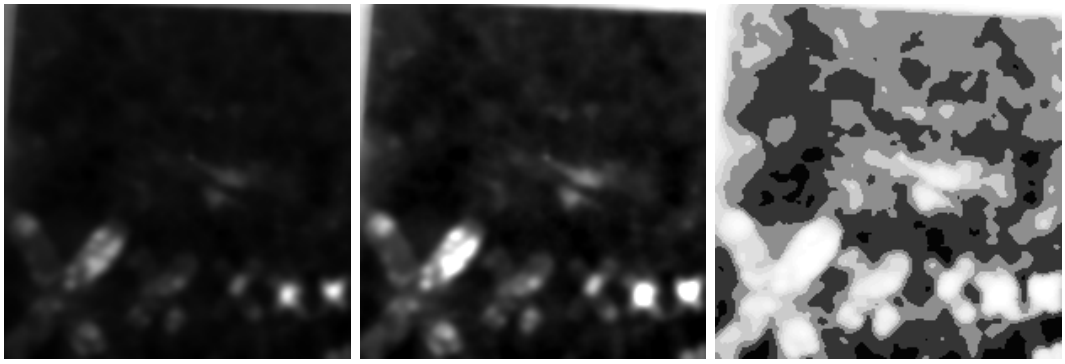

(a) Normalization (b) Normalization with End Saturation (c) Histogram Equalization

Fig. 5.4: Contrast stretching at $t = 228.8$ ms.

can be emphasized in contrast with others. This is advantageous when applied to documents with complex structures because the writing layer can be selected and emphasized as illustrated in Figure 5.5. Figure 5.5(a) shows an effective choice of sample frame and differential contrast image choice to reveal the top layer of ink. On the other hand Figure 5.5(b) better reveals the bottom layer of ink.

The images from the other contrast definitions are presented in Figure 5.6. It is apparent that the DAC technique outperforms the standard contrast definitions. Note that using the first post-flash frame, instead of the final sample frame, resulted in more effective contrast when using normalized contrast approach.

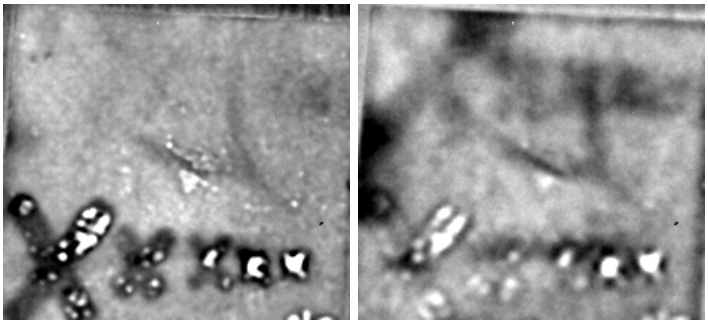

(a) Frame at $t = 46$ ms shown using differential image at $t' = 286$ ms (b) Frame at $t = 515$ ms shown using differential image at $t' = 572$ ms

Fig. 5.5: Differential absolute contrast (DAC) images.

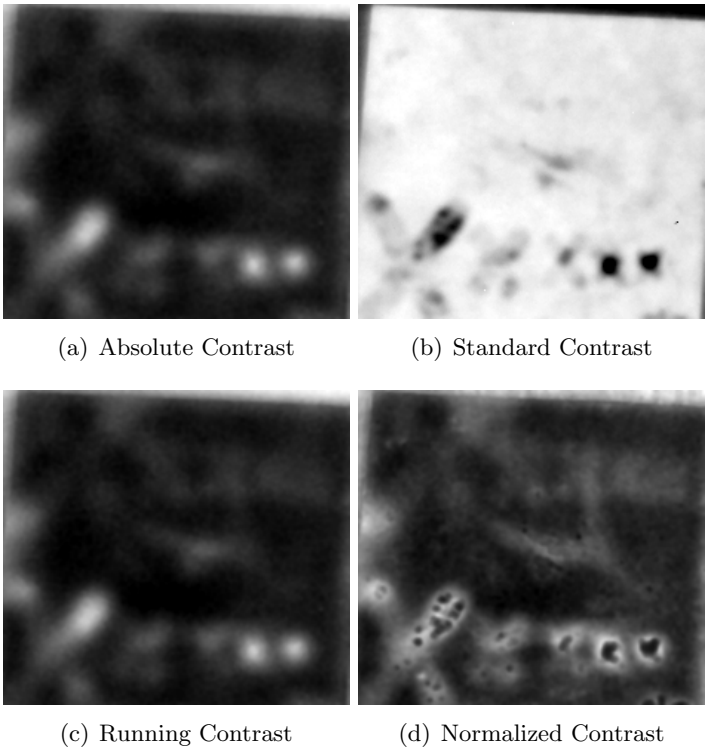

(a) Absolute Contrast (b) Standard Contrast

(c) Running Contrast (d) Normalized Contrast

Fig. 5.6: Contrast definitions.

Thermal Signal Reconstruction (TSR) and Derivative Images

The signal reconstruction and noise reduction of using the TSR technique proved to be beneficial in processing. The derivative images were found to be one of the techniques which provided consistently good defect contrast enhancement. The technique was also able to reveal some of the deep-seated defects. Figure 5.7 presents effective first and second derivative images.

Principal Component Thermography (PCT)

For single-layer homogeneous materials, PCT is effective in revealing a subsurface layer of ink. For great structural complexity of documents, the PCT algorithm tends to enhance some ink areas at the cost of others. The result was that obtaining good results was inconsistent in revealing subsurface ink. However, the PCT technique is an effective technique as illustrated in Figure 5.8. It was found useful to inspect only the first five to ten principal component images.

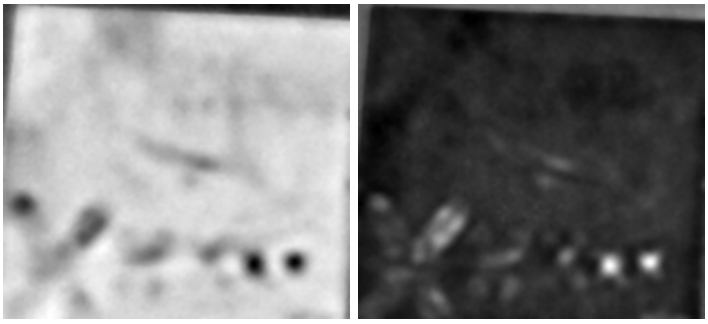

(a) First Derivative (b) Second Derivative

Fig. 5.7: Derivative images.

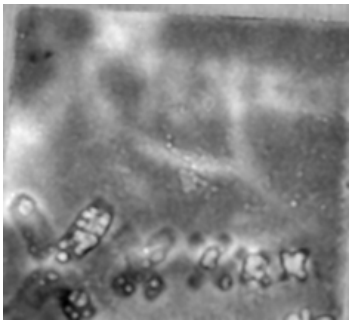

Fig. 5.8: Principal component thermography (PCT) images.

Dynamic Thermal Tomography (DTT)

The DTT approach proved to be mediocre in revealing subsurface inks. The DTT algorithm was able to reveal the ink of the top layer, but was unable to reveal the deep-seated layer of ink as shown in Figure 5.9. In addition, it was found that the reference-free technique is preferred because it enhances the ink as well or better than the classical technique without the need for manually selecting a defect-free region.

Pulse Phase Thermography (PPT)

The PPT phase images consistently revealed the subsurface defects. Due to the increased independence to surface features, the PPT phase images also were found to be effective in revealing the subsurface writing for complex document structures. As expected, the low frequency phase images reveal deep-layered defects better than do the high frequency phase images. Therefore, PPT is an essential processing tool for analyzing documents. Fig-

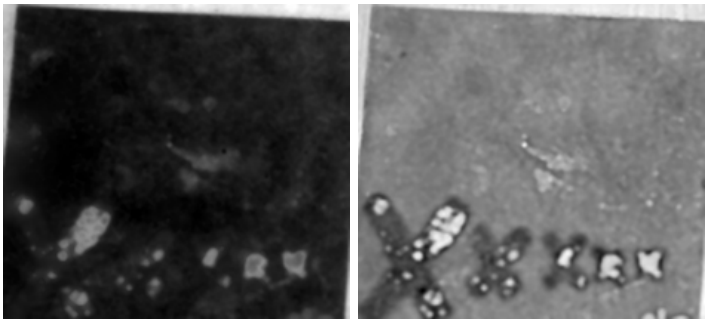

(a) Classical Maxigram (b) Reference-Free Maxigram

Fig. 5.9: Dynamic thermal tomography (DTT) images.

ure 5.10 presents the PPT phase image corresponding to 1.2 Hz. However, PPT algorithm still is unable to reveal the bottom ink layer effectively in this document.

Correlation Images

The FCA algorithm performed moderately well in each test. In general, techniques such as PPT, DAC, THD, MEC, or derivative images outperformed the FCA algorithm or the correlated contrast image. The correlation images are presented in Figure 5.11.

Transmission Line Matrix Fitting Algorithm (TLMFa)

The transmission line matrix model fitting algorithm (TLMFa) proved to be computationally intensive without providing significant improvements in subsurface ink enhancement. Therefore, the TLMFa algorithm is not recommended as a document thermography algorithm. Only a simplified, 1D version of the algorithm was implemented. Implementing

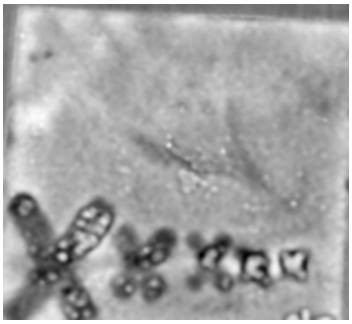

Fig. 5.10: Pulse phase thermography (PPT) image at 1.2 Hz.

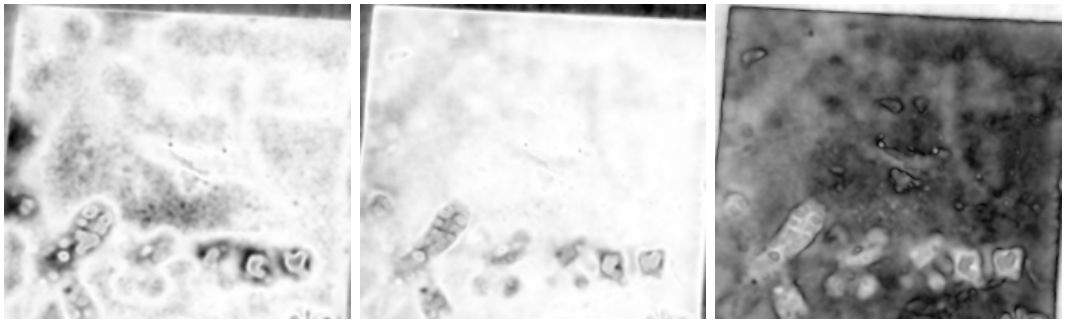

(a) Angle Cosine (b) Correlation Coefficient (c) Correlated Contrast

Fig. 5.11: Correlation images.

a higher dimensional transmission line matrix would further increase the computational expense, but could possibly provide better detail and be of interest for further research. A detailed reflection coefficient image is shown in Figure 5.12. It was found that at least 25 transmission line nodes are required to create an effective fitting.

Hough Transform Thermography (PTHTa)

The PTHTa algorithm was found to be useful in detecting the subsurface inks although it was computationally intensive. The images corresponding to the coefficients of the exponential fit are presented in Figure 5.13. The B coefficient image shown in Figure 5.13(b) reveals the deepest layer of subsurface inks. The PTHTa technique is an effective technique; however, due to its computationally intensive nature use of alternate techniques is suggested.

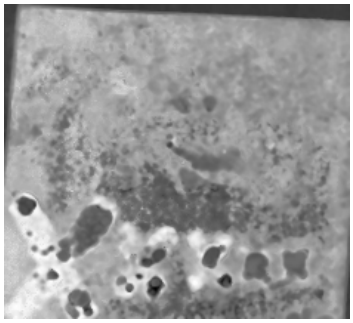

Fig. 5.12: Transmission line matrix fitting algorithm (TLMFa) image.

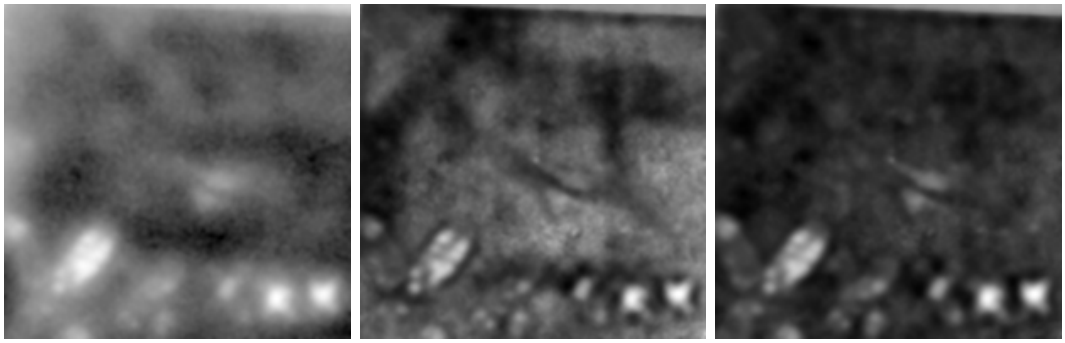

(a) A Coefficient Image (b) B Coefficient Image (c) C Coefficient Image

Fig. 5.13: Hough transform coefficient images.

Time-Difference Contrast

The time-difference contrast technique was found to be among the more effective techniques. This technique works effectively when differencing each frame from the fifth previous frame. Results from this technique are given in Figure 5.14, where Figure 5.14(a) shows the top layer of ink effectively and Figure 5.14(b) reveals the bottom layer of ink effectively.

Total Harmonic Distortion (THD)

The THD technique proved to be an effective technique as illustrated in Figure 5.15. The THD technique is able to reveal the deep-seated layers of ink as effectively or more so than the other methods used. Both the THDa and THDp versions yield similar results and are able to reveal the deep-seated inks better than the SNR image. An advantage that THD has over the contrast images is that it is able to reveal the top and bottom layers

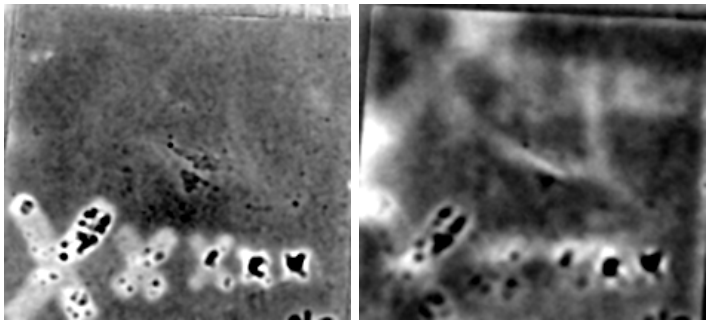

(a) $t = 114$ ms (b) $t = 515$ ms

Fig. 5.14: Time-difference contrast images.

of ink effectively in a single image. The disadvantage of THD is that the visualization of the inks are affected by lateral diffusion more than in techniques such as PPT, causing an increase in blurriness of the detected subsurface inks.

Markov Error Contrast (MEC)

The Markov Error Contrast (MEC) technique was able to effectively reveal both surface and deep-seated layers of writing as well or better than alternate techniques as can be seen in Figure 5.16. The MEC technique provides a new useful tool for processing flash thermography data. The MEC technique has an advantage over the DAC technique, both of which give similar results, in that the MEC technique does not require selection of a differential frame.

Time Constant Analysis (TCA)

The time constant analysis (TCA) technique performed effectively on single-layer document structures. It proved to be an effective technique for analyzing flash thermography video streams as can be seen from the results shown in Figure 5.17. Because of the computational expense of TCA, other techniques with similar effectiveness, such as PPT, MEC, or DAC, are often preferable.

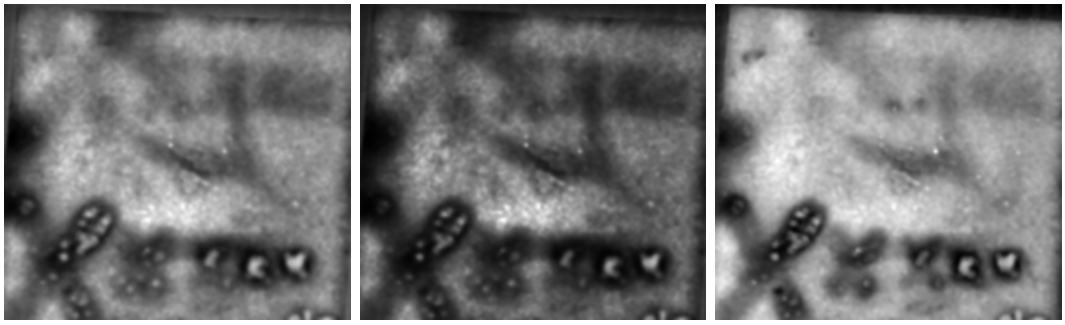

(a) THDa (b) THDp (c) SNR

Fig. 5.15: Total harmonic distortion (THD) images.

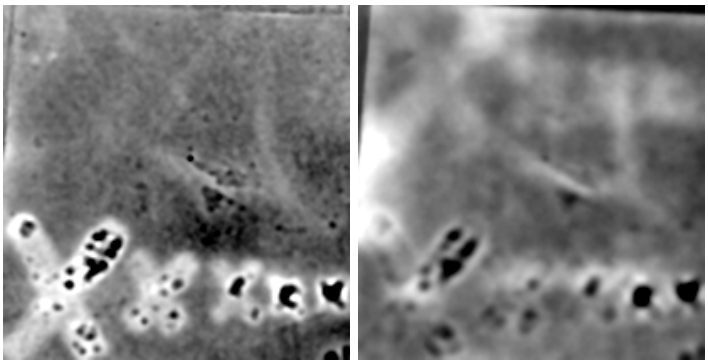

(a) $t = 114$ ms (b) $t = 572$ ms

Fig. 5.16: Markov error contrast (MEC) images.

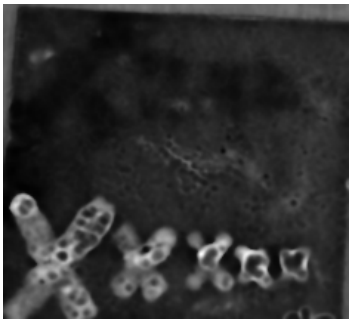

Fig. 5.17: Time constant analysis (TCA) image.

Signal Detection and Matched Filtering

Four of the matched filter methods consistently performed well in the tests: the Spectral Angle Map (SAM), Adaptive Coherence Estimate (ACE), the t-statistic, and the F-statistic. The results for using each of the four filters are presented in Figure 5.18. These techniques are able to effectively reveal both layers of ink in a single image. More effective results are obtained when the deep-seated ink layers are chosen as the target pixels.

5.1.2 Document Strikeouts

The following section presents the results for revealing strikeouts contained in surface writings of a document. Strikeouts refer to areas where two layers of the same ink overlap as a result of textual changes. It is important to note that each image was pre-processed using the noise reduction technique previously described and that the results were manually contrast enhanced.

The document sample shown in Figure 5.19 was constructed to evaluate the effectiveness of imaging document strikeouts. The sample data set was constructed using iron gall ink on a white card stock substrate. It consists of an "X" shaped ink under-layer with horizontal stripes overlaying the "X." The algorithms that performed effectively in revealing strikeouts are discussed and their results demonstrated in this section.

Contrast Definitions and Differential Absolute Contrast (DAC)

Three of the contrast definitions were found useful for evaluating strikeouts: the absolute contrast, running contrast, and normalized contrast. The most effective results for each contrast definition can be seen in Figure 5.20. The absolute and running contrast approaches give very similar images in which half of the general shape of the "X" can be seen. However, the normalized contrast gives the best results of the three methods since the entire ink structure can be seen. Notice in the normalized contrast shown in Figure 5.20(c), the areas appear brighter where the two layers of writing overlap. In the upper right hand corner, the rectangular shape of the underlying "X" can be seen clearly. In addition, the differential absolute contrast also performed well as illustrated in Figure 5.21.

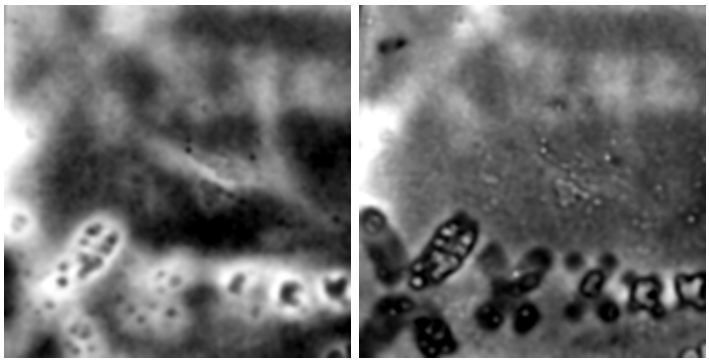

(a) SAM (b) ACE

(c) f-statistic (d) t-statistic

Fig. 5.18: Matched filter images.

Fig. 5.19: Strikeouts test set.

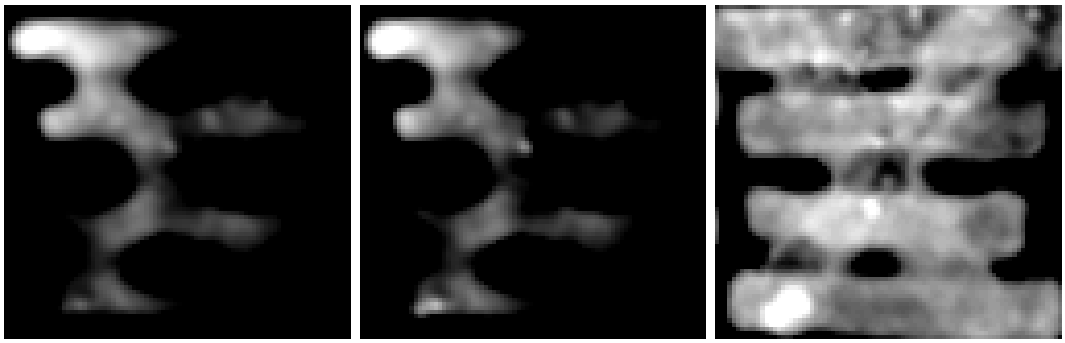

(a) Absolute Contrast (b) Running Contrast (c) Normalized Contrast

Fig. 5.20: Contrast definition strikeout images.

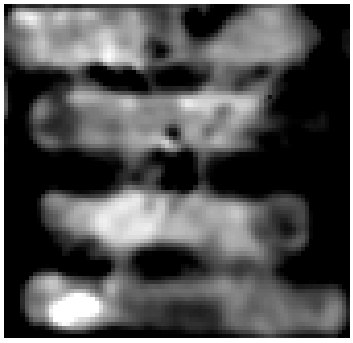

Fig. 5.21: DAC strikeout image with $t' = 11.5$ ms and $t = 57.5$ ms.

Dynamic Thermal Tomography (DTT)

For detecting strikeouts, the classical DTT algorithm significantly outperformed the reference-free DTT algorithm. This is the opposite conclusion that was drawn when detecting subsurface inks. The results of the DTT algorithm can be seen in Figure 5.22.

Markov Error Contrast (MEC)

The Markov Error Contrast (MEC) algorithm proved to be useful in the detection of document strikeouts. The results from MEC are shown in Figure 5.23.

Principal Component Thermography (PCT)

For the PCT algorithmic approach, it was found that decreasing the total time for sampling improved the PCT results. Figure 5.24(a) shows the results for a sampling time of 2.2 s, where Figures 5.24(b) and 5.24(c) show the results for the reduced total sampling time of 172.4 ms. For PCT, reducing the number of frames increased the detectibility of the strikeouts.

Pulse Phase Thermography (PPT)

The PPT algorithmic approach, using the amplitude images rather than the phase images was found to be beneficial in analyzing strikeouts. In addition, it was found higher frequencies were more useful for revealing strikeouts. The result of PPT corresponding to 43.7 Hz is shown in Figure 5.25.

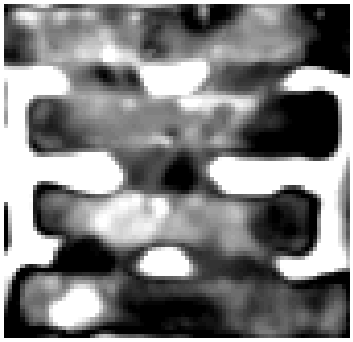

Fig. 5.22: DTT classical maxigram.

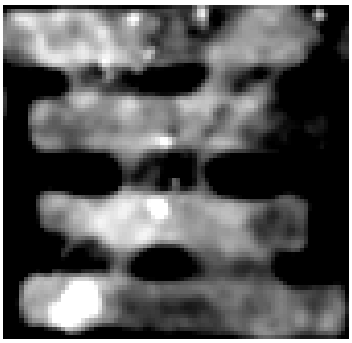

Fig. 5.23: Markov error contrast (MEC) strikeout image.

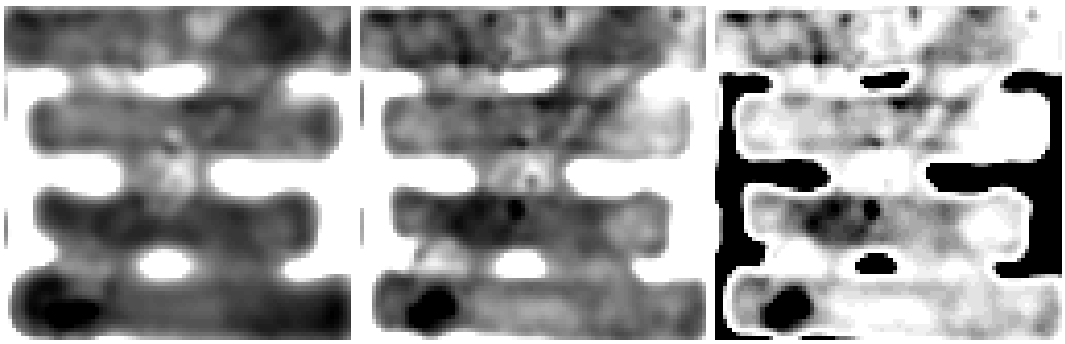

(a) PCM (sampled For 2.2 s) (b) PCM (sampled For 172.4 ms) (c) First principal component (sampled For 172.4 ms)

Fig. 5.24: Principal component thermography (PCT) strikeout images.

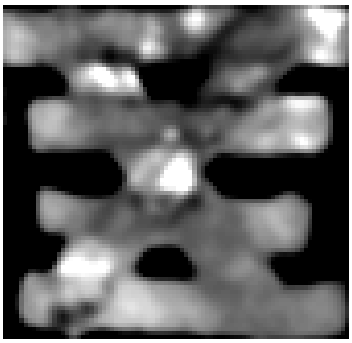

Fig. 5.25: Pulse phase thermography (PPT) amplitude strikeout image.

Transmission Line Matrix Fitting Algorithm (TLMFa)

The results from using the transmission line matrix fitting algorithm (TLMFa) are shown in Figure 5.26. Despite being able to effectively reveal the strikeouts, the extreme computational expense of this technique makes other methods preferred.

Time Constant Analysis (TCA)

The results of the TCA approach can be significantly improved for document strikeouts using a shortened total sampling length. The images in Figure 5.27 were obtained using a total sampling time of 172.4 ms.

Time-Difference Contrast

The results of the time-differencing contrast approach are given in Figure 5.28. The time-difference contrast images are effectively able to reveal the strikeouts.

Derivative Images

It was found that using a shortened total sampling time improved the results of the TSR images for document strikeouts. The first and second derivative images can be seen in Figure 5.29.

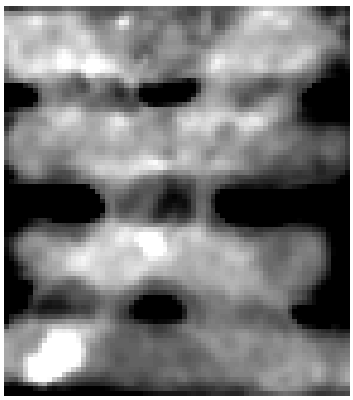

Fig. 5.26: Transmission line matrix fitting algorithm (TLMFa) strikeout image.

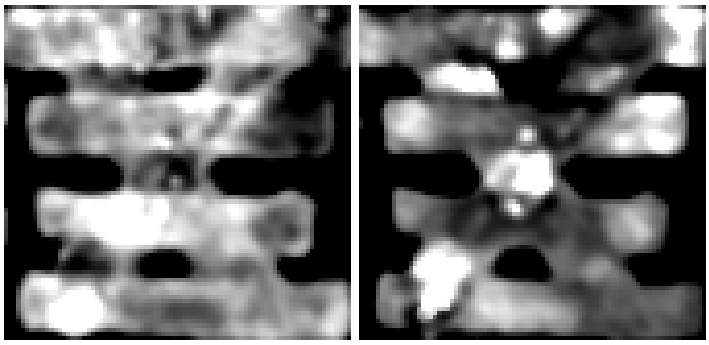

(a) Time Constant (b) Amplitudes

Fig. 5.27: Time constant analysis (TCA) strikeout image.

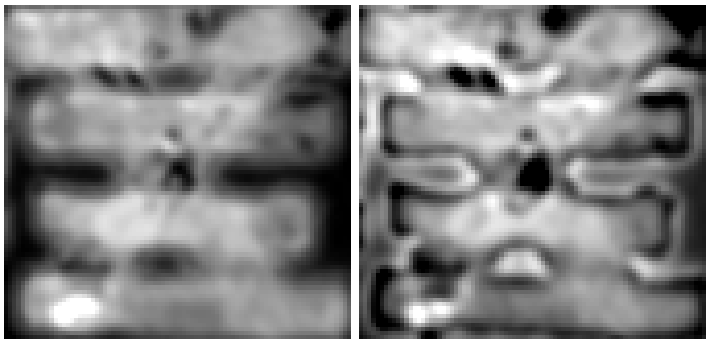

(a) Frame at 69 ms (b) Frame at 287.4 ms

Fig. 5.28: Time-difference contrast strikeout images.

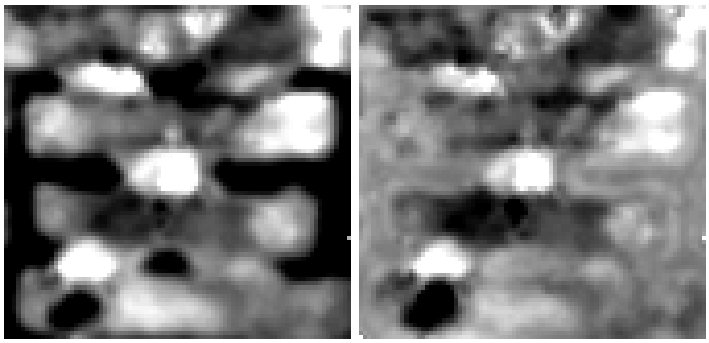

(a) First Derivative (b) Second Derivative

Fig. 5.29: Strikeout derivative images

5.2 Comparison of Algorithm Wall Times

A study was performed comparing processing wall times of each algorithm. The wall time is a measure of the amount of chronological time it takes for a process to complete. The tests were performed on a Intel® Core™ 2 Quad 2.4Ghz CPU Q6600 with 4 GB of memory. The data set used to test the algorithm wall times consisted of 189 frames with each individual frame having dimensions of 72 by 81 pixels. The code was implemented in Matlab with four parallel working nodes. Figure 5.30 shows a bar graph of the wall times created from the data in Table 5.2. The algorithm numbers in Figure 5.30 correspond to the algorithms listed in Table 5.2. Due to their significant computational cost and lack of significant improvements, the TLMFa, PTHTa, and TCA algorithms are not recommended. The contrast images tend to perform well and have minimal computational cost; as such, they are a recommended starting point when processing flash thermography data.

5.3 Comparison with Multi-Spectral Imaging (MSI)

A comparative study was conducted to determine the effectiveness of MSI versus flash thermography techniques. Each tested document type is discussed in the following sections.

5.3.1 Subsurface Inks

Several examples of subsurface inks using a variety of covering layers were tested. Figure 5.31 shows a comparison of MSI images with the flash thermography images for a textured card stock layer. For depth penetration in MSI, the 950 nm image proved to give the best contrast as shown in Figure 5.31(a). Figures 5.31(b), 5.39(c), 5.39(d) show the processed flash thermography images for comparison. Although the MSI approach is able to faintly reveal the subsurface writing, the flash thermography method significantly outperforms the MSI image method in enhancing the contrast of the subsurface inks. In addition, the flash thermography data set can reveal relative depth information for the inks, which MSI is unable to accomplish. Each image in Figure 5.31 have been contrast stretched using image normalization.

Additional comparisons of MSI results versus pulsed thermography results for each of

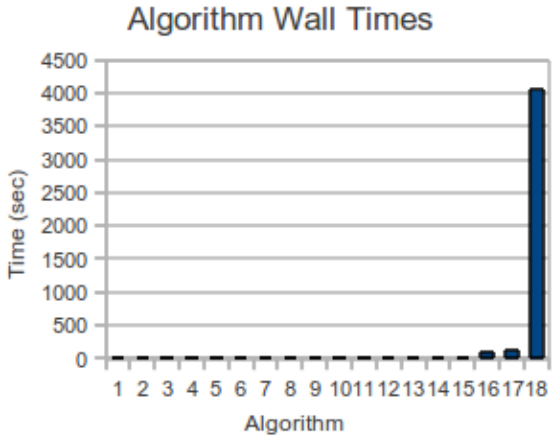

Fig. 5.30: Algorithm wall times.

Table 5.2: Algorithm wall times.

Number	Algorithm	Average Wall Time (sec)
1	DAC	0.03191
2	Absolute Contrast	0.03244
3	Normalized Contrast	0.03979
4	Standard Contrast	0.04003
5	Running Contrast	0.04579
6	MEC	0.1597
7	THD	0.3365
8	PPT	0.3465
9	PCT	0.7850
10	MF	1.075
11	TDC	1.357
12	DTT (Classical)	2.948
13	TSR	4.037
14	DTT (Reference-free)	6.843
15	Correlation Images	10.76
16	TCA	99.96
17	PTHTa	125.9
18	TLMFa	4044

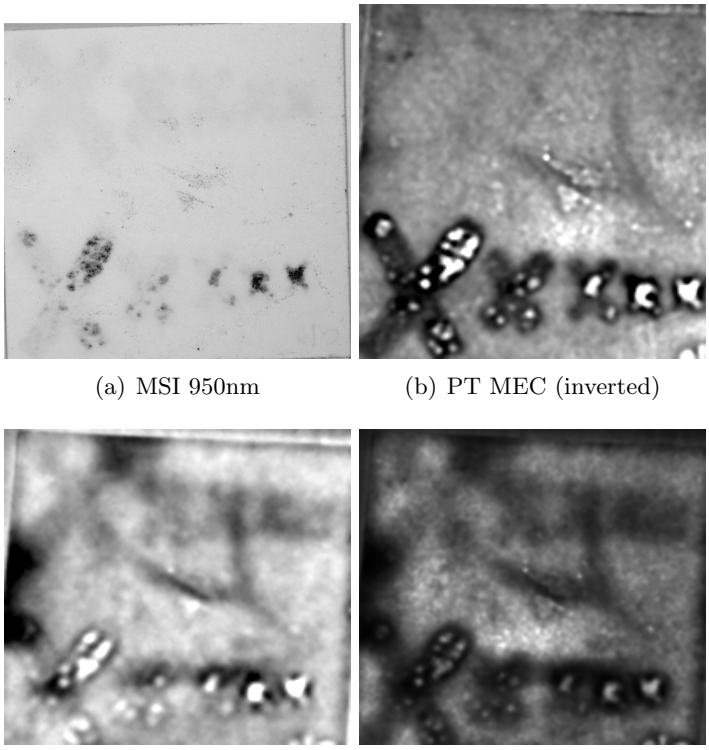

(a) MSI 950nm

(b) PT MEC (inverted)

(c) PT Time-Difference (inverted)

(d) PT THDp

Fig. 5.31: MSI vs. FT strikeout results.

the subsurface document classes are shown in Figures 5.32-5.39. Three inks were tested: (1) ball point (upper right), (2) carbon (upper right and lower left), and (3) iron gall (lower right). Figure 5.32 shows the under-writing for two test documents covered with a sheet of white card stock. Figure 5.33 shows the flash thermography results for the ink underwriting. Unfortunately, an MSI comparison is not available for this data set. However, Figure 5.34 compares the detection of an Edmunds Optics Resolution Chart placed underneath a white card stock layer. It can be seen that the flash thermography images are better able to reveal the optics card.

The papyrus test document is shown in Figure 5.35. For the papyrus covering layer, shown in Figure 5.36, the MSI image provides a cleaner result than the PT images. This is expected for thin layers, such as this particular sheet of papyrus.

Figure 5.37 shows the paint test document and the imaging results are presented in

(a) Ink Layer (b) Optics Card

Fig. 5.32: Cardstock test document under-layers.

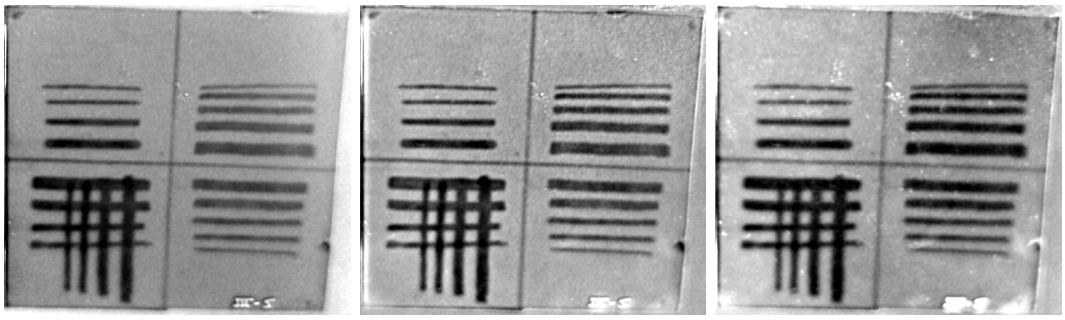

(a) PT MEC (inverted) (b) PT PCT (c) PT MF-ACE (inverted)

Fig. 5.33: MSI vs. PT cardstock results.

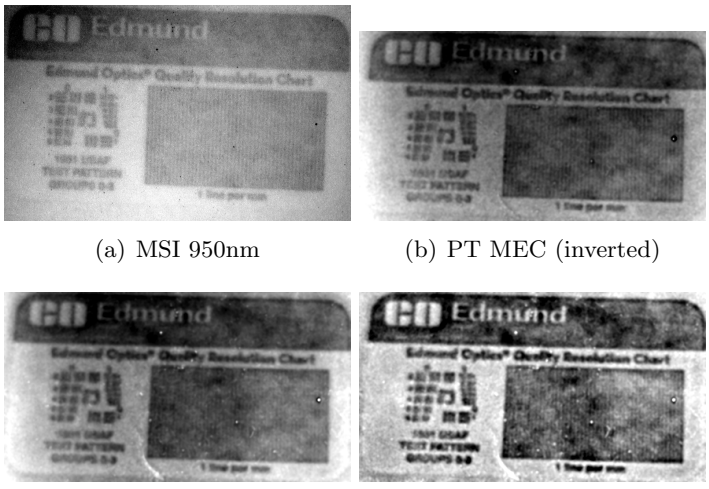

(a) MSI 950nm (b) PT MEC (inverted)

(c) PT TDC (inverted) (d) PT PPT

Fig. 5.34: MSI vs. FT cardstock 2 results.

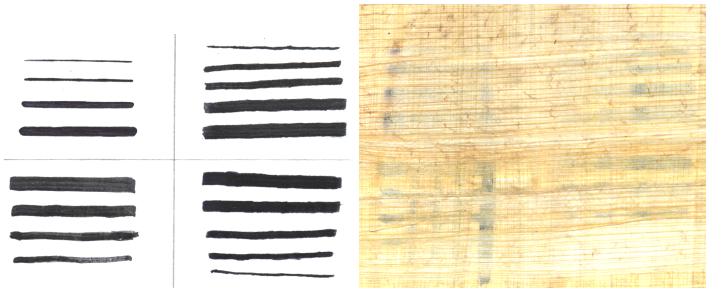

(a) Ink Layer (b) Papyrus Covering

Fig. 5.35: Papyrus test document.

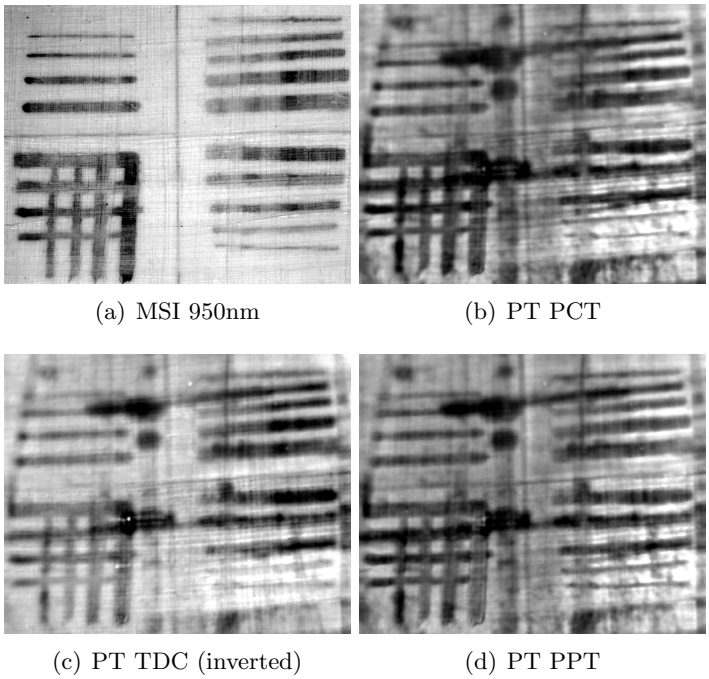

(a) MSI 950nm (b) PT PCT

(c) PT TDC (inverted) (d) PT PPT

Fig. 5.36: MSI vs. FT papyrus results.

Figure 5.38. Both the MSI and the PT methods are able to reveal the majority of the ink underneath the painted layer. However, the PT techniques are able to reveal the writings beneath the black paint which the MSI fails to reveal. This indicates that PT can be used to reveal writings underneath a layer that has similar spectral properties but different thermal properties.

Figure 5.39 demonstrates the ability of flash thermography to reveal subsurface inks beneath a layer of gesso. In this case, the MSI technique performs poorly. The results presented in this section demonstrate the ability of flash thermography to image subsurface inks beneath a variety of covering materials.

5.3.2 Document Strikeouts

For document strikeouts, MSI fails completely to reveal the under-layer of writing as shown in Figure 5.40(a). However, Figures 5.40(b) and 5.40(c) prove the ability of flash thermography to detect document strikeouts. The ability of flash thermography to detect document strikeouts is a significant result that can allow for the evaluation of documents that have previously been unable to analyze effectively.

5.3.3 Surface Writing Enhancement

The purpose of the test document shown in Figure 5.41(a) is to evaluate the ability of flash thermography to enhance surface inks that have poor spectral contrast. Figures 5.41(b) and 5.41(c) show the results of two different wavelength MSI images. In the 950 nm

(a) Ink Layer (b) Paint Covering

Fig. 5.37: Paint test document.

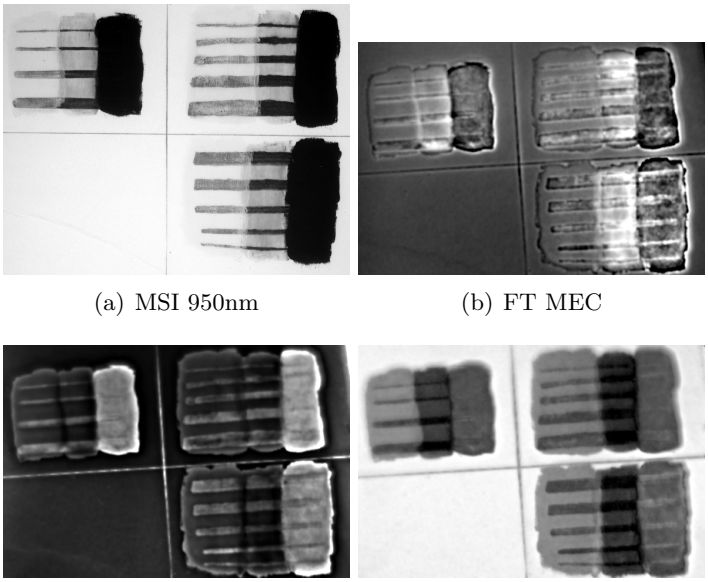

(a) MSI 950nm (b) FT MEC

(c) FT THDp (d) FT PPT

Fig. 5.38: MSI vs. FT painted images.

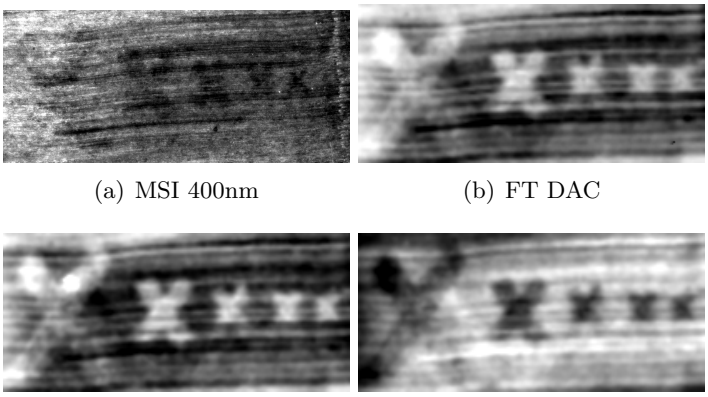

(a) MSI 400nm (b) FT DAC

(c) FT PPT (d) FT Time-Difference Contrast

Fig. 5.39: MSI vs. FT gesso images.

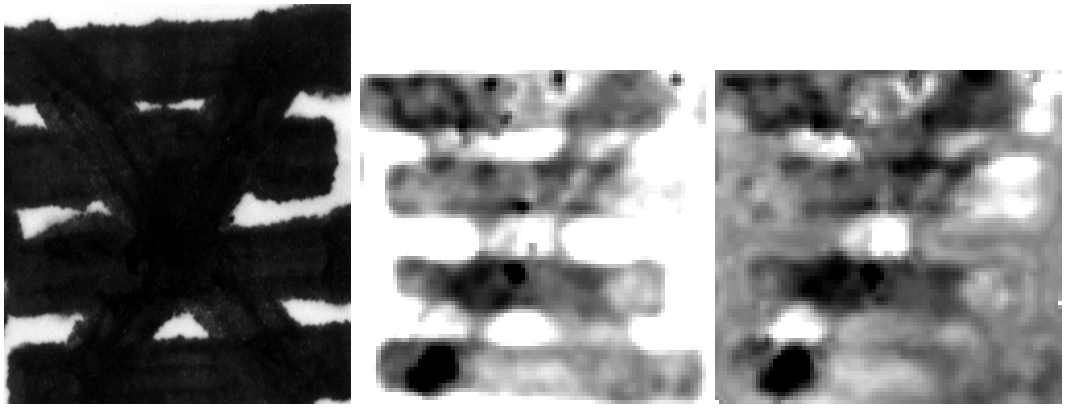

(a) MSI 950nm (b) PT MEC (inverted) (c) PT 2nd Derivative

Fig. 5.40: MSI vs. FT strikeout results.

image, the surface inks have poor contrast; however, in the 600 nm they have significant contrast. The two ink writings can also be seen in the flash thermography images shown in Figures 5.41(d)-5.41(f). Although both the red and blue inks can be seen in both MSI and FT images, the important difference is the MSI images are comparing differences in optical properties whereas the FT images are comparing the differences in thermal properties. This indicates that flash thermography can be used to enhance the writings of surfaces that contain poor spectral contrast but have a large differences in thermal properties of materials.

5.4 Feasibility of Application to Archaeological Artifacts

The methodology presented in this thesis was validated by applying the developed flash thermography techniques to a piece of Egyptian cartonnage and the Codex Selden.

5.4.1 Egyptian Cartonnage

The cartonnage is an ancient document with a complex structure, containing overlapping areas of ink, papyrus, gesso, and paint. Further imaging challenges arise from the significant material inhomogeneities and internal flaws contained within the cartonnage. Figures 3.2 and 5.42 provides comparisons between standard imaging, MSI techniques, and flash thermography techniques.

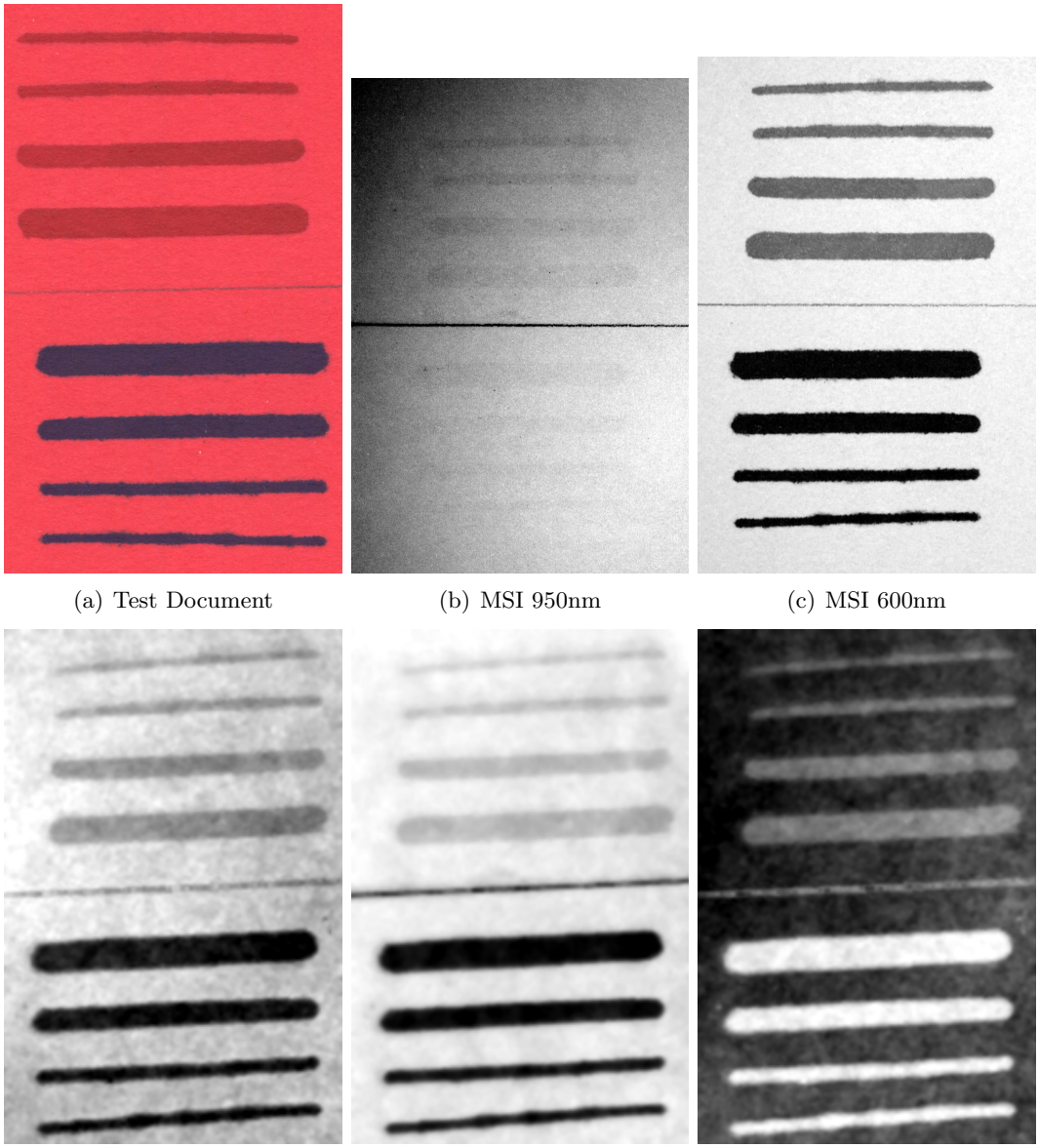

(a) Test Document (b) MSI 950nm (c) MSI 600nm

(d) PT PPT (e) PT 2nd Derivative (f) PT MF-ACE

Fig. 5.41: MSI vs. FT red surface results.

From these figures, several conclusions may be reached. First, both the MSI images and the flash thermography images are comparable in their ability to significantly enhance the cartonnage surface writing. The important difference between the two methods is the technique used to enhance the surface writing. MSI enhances this text through differences in the spectral characteristics of ink and the papyrus background. On the other hand, flash thermography enhances the surface writing through differences in the thermal properties of the ink and the papyrus background.

To illustrate that the ink is not enhanced due to spectral characteristics in flash thermography, a pre-flash cartonnage image is shown in Figure 5.43. In the pre-flash image, the surface ink cannot be observed, indicating that differences in spectral characteristics have a insignificant contribution to the visualization of the ink. Thus text on ancient documents that previously were not effectively imaged using MSI because of poor spectral contrast between inks and document backings, can now be imaged using flash thermography to reveal these obscure writings.

A second important conclusion from this study is the improvement flash thermography provides over MSI imaging when applied to ink just below the document structure. This is illustrated in Figure 5.42(c). A red arrow points to a subsurface ink line that is not observed in Figure 5.42(a). This indicates that flash thermography successfully revealed shallow subsurface ink that MSI could not show.

5.4.2 Codex Selden

The Codex Selden is a Mesoamerican manuscript book that is a recognized palimpsest [103–105]. The original pictograph drawings were covered with a gesso layer, and a new set of pictographs were drawn on the surface. The Codex Selden presents several unique imaging challenges including: (1) an unknown thickness of the gesso layer, (2) an unknown extent to which the original writing has been removed, and (3) internal flaws within the gesso that may obscure detectability of under-inks.

The Codex Selden data was collected using a ThermaCAM Phoenix 600 camera operating in the 1.5-5.0 μm range with a data acquistion rate of 67 frames/second. Two Sunpak

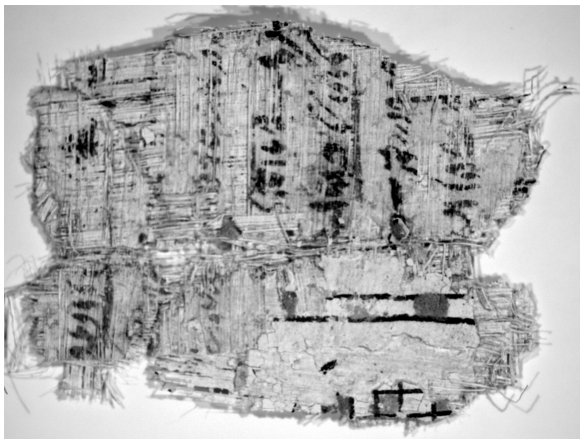

(a) MSI 950nm

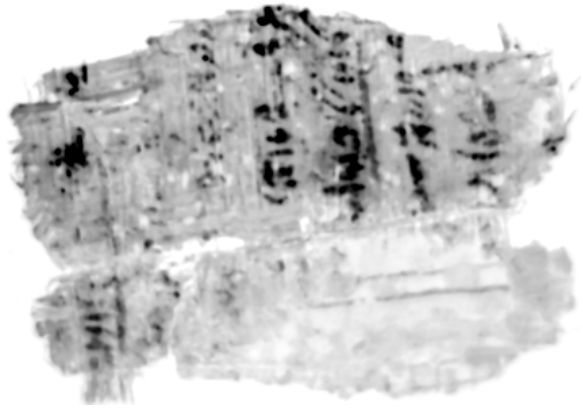

(b) FT PPT Amplitude Image (Inverted)

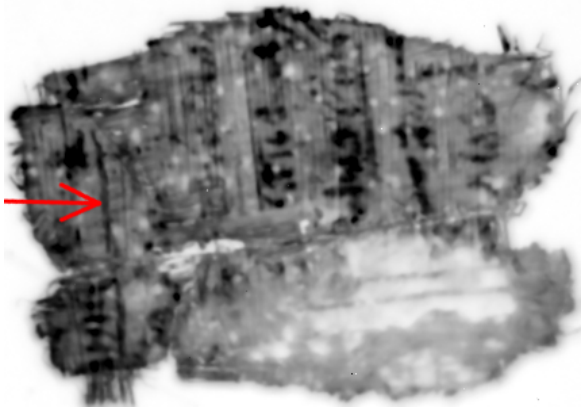

(c) FT Standard Contrast

Fig. 5.42: MSI vs. FT cartonnage images.

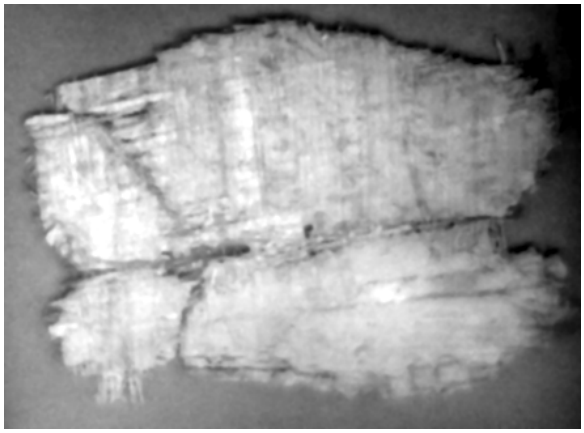

Fig. 5.43: Pre-flash FT cartonnage image.

Pro System 622 flash units provided the impulse energy [106]. Imaging access to the Codex Selden was limited and the images presented were obtained early in this research before the most efficient flash thermography parameters had been established.

The results of imaging three sections of the Codex Selden are presented in Figures 5.44, 5.45, and 5.46. In Figure 5.46(b), the vertical and horizontal line discontinuities within the image are an artifact of combining several images. Deeper document structural defects can be detected using flash thermography techniques over MSI as illustrated by the examples given. It is too premature to conclude if any of these areas are potentially subsurface inks. In addition, flash thermography enhances the thin surface inks, demonstrating that ancient inks as well as modern ink can be enhanced using flash thermography techniques. It is reasonable to assume sufficient thermal bonding between the gesso and the subsurface inks. Re-obtaining the data set with larger amplitude excitation pulse is recommended.

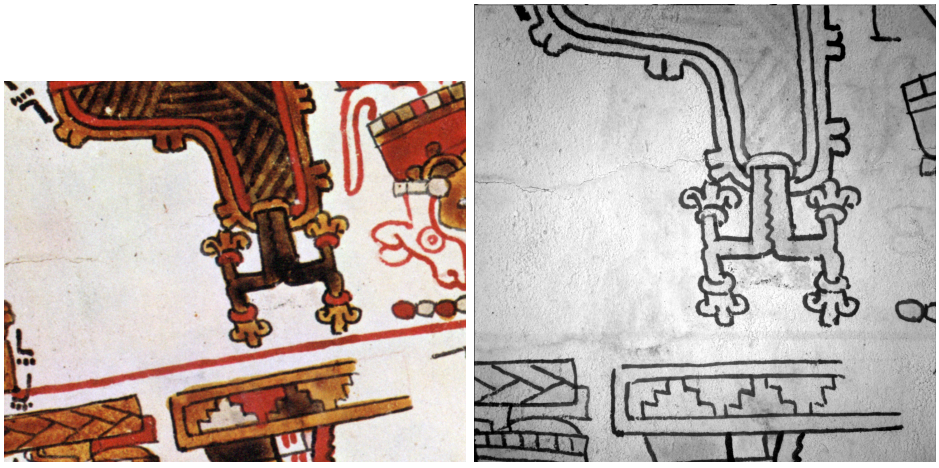

(a) Visible Image (b) MSI 1000 nm

(c) FT PPT (d) FT PCT

Fig. 5.44: MSI vs. FT Codex Selden images data set 1.

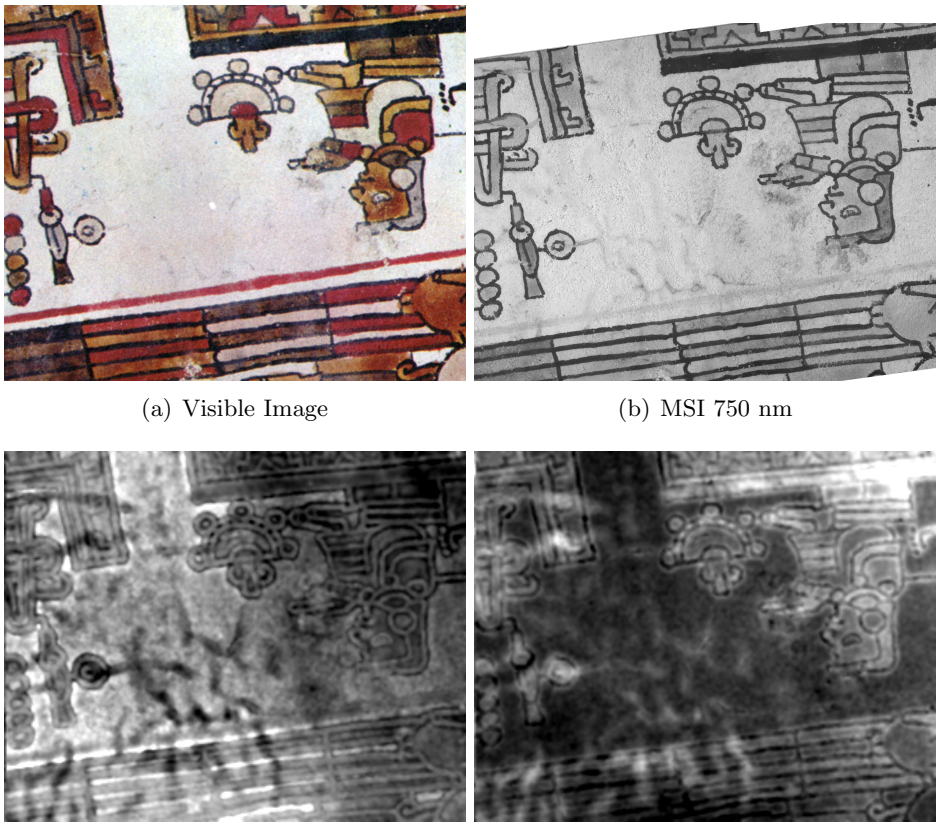

(a) Visible Image (b) MSI 750 nm

(c) FT PPT (d) FT MEC

Fig. 5.45: MSI vs. FT Codex Selden images data set 2.

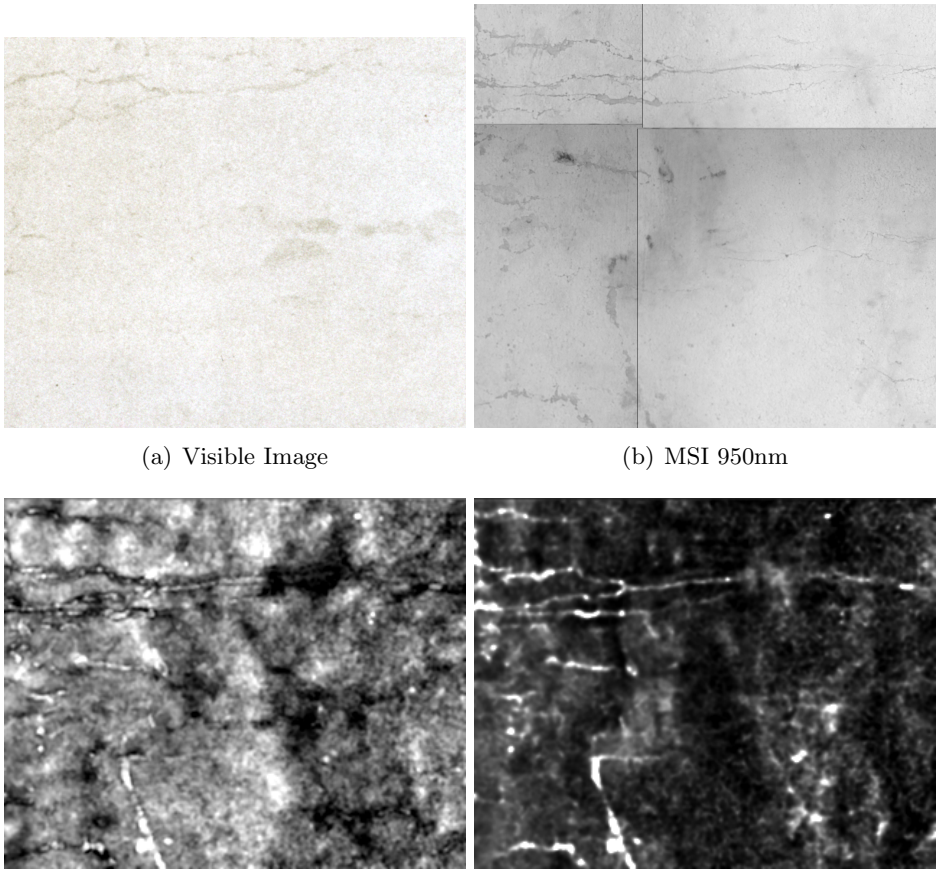

(a) Visible Image (b) MSI 950nm

(c) FT PPT (d) FT MF t-statistic

Fig. 5.46: MSI vs. FT Codex Selden images data set 3.

Chapter 6

Conclusions and Recommendations

The conclusions developed from the results presented in Chapter 5 are summarized in this chapter. The flash thermography parameters for effective flash thermography data acquisition are outlined. A summary of methods for pre-processing, processing, and post-processing the data to increase ink visualization are given. The ability of flash thermography to image a variety of materials are discussed. Finally, this thesis concludes with recommendations for future research.

6.1 Thermography Data Acquisition Parameters

Several flash thermography parameters were evaluated during the acquisition of the data sets. Recommended values are discussed below.

Pulse Amplitude Four synchronized flash units were sufficient to reveal subsurface layers of ink (after processing) through paper, card stock, papyrus, and thin gesso layers. Large pulse amplitudes are desirable, but care must be taken to reduce the residual heating from the flash bulb which may occur. For document strikeouts or enhancing surface writing, a large pulse amplitude is unnecessary.

Pulse Duration Residual heating from flash pulse tails were not found to have a strong negative effect on the detection process for deep-seated subsurface writings, provided the tail decayed relatively quickly and absorbed uniformly into the document. For document strikeouts and surface ink enhancement, a minimal input pulse length that closely approximates an impulse is desired.

Sampling Frequency A sampling frequency of 87 Hz was found adequate for subsurface defects; however, a faster sampling rate is recommended for document strikeouts and surface ink enhancement.

Lens Filters The $3.42 - 4.05$ μm filter greatly outperformed the $2.65 - 3.24$ μm filter.

6.2 Pre-Processing

The following techniques were found useful for pre-processing flash thermography data when applied in the following order:

1. Subtraction of a pre-flash image to each frame in order to reduce effects of non-uniform surface emissivities;
2. A 3×3 pixel median filter applied to each frame for removing outliers caused by dead pixels;
3. A 3×3 Gaussian low-pass filter, with a variance parameter of 0.8, applied to reduce spatial image noise in each frame;
4. Thermal signal reconstruction (TSR), using a sixth order polynomial fitting, for reducing temporal noise.

6.3 Processing

Effective processing techniques for each document class are presented. Table 6.1 outlines a rating system used in classifying the algorithms. Table 6.2 evaluates the pre-existing and developed algorithm techniques used for processing flash thermography data of documents. Note that due to the similarities between processing strikeouts and surface ink enhancement, the ratings for strikeouts also apply to surface writing enhancement.

6.4 Post-Processing

Essential post-processing methods include the following contrast stretching techniques:

1. Manual histogram manipulation,
2. Image normalization,
3. Image normalization with ends saturation,

Table 6.1: Algorithm rating system.

Value	Definition	Explanation
3	Highly Recommended	Consistently gives great results with minimal computational expense.
2	Recommended	Performs well but inconsistently. May only work for simple document structures or computational expense is moderate.
1	Moderately Recommended	Performs well occasionally or has a significant computation expense.
0	Not Recommended	Either fails to perform well or computational expense is prohibitive.

4. Pseudo-color images.

Other techniques which may be useful, depending on the situation, include:

1. Histogram equalization,
2. Image filter (median or Guassian),
3. Absolute and running contrast definitions.

6.5 Materials

This research demonstrated that flash thermography can be used to detect three types of inks: carbon-based, iron gall, and modern ball-point. These inks were detected beneath several covering layers including card stock, papyrus, paint, a gesso mix, and the ink itself.

6.6 Significant Contributions

This research resulted in the following significant contributions.

1. A comprehensive analysis of existing pulsed thermography processing techniques applied to documents, the magnitude of which does not exist in the literature. Pre-existing techniques investigated include pseudo-color images, contrast stretching, synthetic signal reconstruction, median and Gaussian low-pass filters, four contrast definitions, differential absolute contrast (DAC), derivative images, principal component

thermography (PCT), classical and reference-free implementations of dynamic thermal tomography (DTT), pulse phase thermography (PPT), correlation images, transmission line matrix fitting algorithm (TLMFa), and pulsed thermography Hough transform algorithm (PTHTa).

2. New pulsed thermography processing techniques that improve upon the results of the existing techniques were developed. These techniques include Markov error contrast (MEC), time-difference contrast, total harmonic distortion (THD), time constant analysis (TCA), and four matched filter definitions including spectral angle map (SAM), adaptive coherence estimator (ACE), t-statistic, and F-statistic.

3. A proof-of-concept for detecting subsurface ink writings in documents.

4. Verification of the capability of pulsed thermography techniques to detect document strikeouts.

5. Demonstrates the ability to enhance surface writings based on differences in thermal characteristics when spectral characteristics do not differ significantly.

6. Demonstrates that pulsed thermography significantly improves upon multi-spectral imaging for subsurface and surface writing enhancement.

7. Provides an evaluation of flash thermography parameters for the most effective document imaging.

8. Validates the findings presented through application of flash thermography techniques to a piece of Egyptian cartonnage and the Codex Selden.

9. A Pulsed Thermography Toolbox was developed providing a graphical user interface in MATLAB for the straight-forward application of the presented processing techniques to flash thermography data.

6.7 Recommendations for Future Research

There are two principal directions suggested for future research. The first recommendation is the development of advanced thermal models that account for the uneven, multiple layers which are often found in ancient documents. From these advanced thermal models, processing techniques with greater effectiveness can be developed specific to this application. The second recommendation is research into alternate heating methods to facilitate for greater excitation energy. Methods of future research could explore step heating, thermal transfer heating, or modulated thermography techniques. For document strikeouts, it is recommended that the experiments be repeated using a thermal camera capable of significantly faster frame rates. Investigation of techniques which account for the lateral diffusion through the ink would also be beneficial.

Table 6.2: Processing algorithms summarized.

Processing Technique	Subsurface Rating	Strikeout Rating	Wall Time (Sec)	Comments
Contrast Definitions	1	1	0.03951	Can be used as a post-processor. (4.2.6)
Differential Absolute Contrast (DAC)	3	3	0.03191	Requires parameter selection. (4.2.7)
Derivative Images	2	3	4.037	Use limited time sequence for strikeouts. (4.2.8)
Principal Component Thermography (PCT)	2	2	0.7850	May enhance some features over others. Use limited time sequence for strikeouts. (4.2.9)
Classical Dynamic Thermal Tomography (DTT)	1	2	2.948	Performs moderately for detecting strikeouts. (4.2.10)
Reference-free Dynamic Thermal Tomography (DTT)	2	1	6.843	Unable to reveal the deepest defects and has a moderate computational load. (4.2.10)
Pulsed Phase Thermography (PPT)	3	3	0.3465	Consistently performs well. (4.2.11)
Correlation Images	0	0	10.76	Generally poor performance. (4.2.12)
Transmission Line Matrix Fitting (TLMFa)	0	0	4044	Prohibitively large computational expense. (4.2.13)
PT Hough Transform (PTHTa)	1	0	125.9	Large computational expense. (4.2.14)
Time-Difference Contrast (TDC)	3	3	1.357	Differencing each frame from the fifth previous is effective. (4.3.1)
Total Harmonic Distortion (THD)	2	2	0.3365	Works best with simple document structures. (4.3.2)
Markov Error Contrast (MEC)	3	3	0.1597	Performs consistently well. (4.3.3)
Time Constant Analysis (TCA)	1	1	99.96	Limited to simple documents and has a large computational expense. (4.3.4)
Matched Filters (SAM, ACE, t/F-statistic)	3	3	1.075	Requires proper selection of deepest defect area. (4.3.5)

References

[1] F. C. Sham, N. Chen, and L. Long, "Surface crack detection by flash thermography on concrete surface," *Insight*, vol. 50, no. 5, pp. 240–243, April 2008.

[2] J. Sham Fung Chu, *Studies of Using Infrared Flash Thermography (FT) for Detection of Surface Cracks, Subsurface Defects and Water-Paths in Building Concrete Structures*. Ph.D. dissertation, City University of Hong Kong, July 2008.

[3] H. Nayeb-Hashemi, D. Swet, and A. Vaziri, "New electrical potential method for measuring crack growth in nonconducive materials," *Measurements*, vol. 36, pp. 121–129, 2004.

[4] M. A. Omar, Y. Zhou, R. Parvataneni, and E. Planting, "Calibrated pulse-thermography procedure for inspecting HDPE," *Research Letters in Materials Science*, vol. 2008, no. 186427, p. 4, 2008.

[5] K. T. Wan and C. K. Y. Leung, "Fiber optics sensor for the monitoring of mixed mode cracks in structures," *Sensors and Actuators*, vol. 135, pp. 370–380, 2007.

[6] C. Ibarra-Castanedo, M. Genest, P. Servais, X. P. V. Maldague, and A. Bendada, "Qualitative and quantitative assessment of aerospace structures by pulsed thermography," *Nondestructive Testing and Evaluation*, vol. 22, no. 2-3, pp. 199–215, June-September 2007.

[7] P. Meinlschmidt, "Thermographic detection of defects in wood and wood-based materials," *14th International Symposium of Nondestructive Testing of Wood*, May 2005.

[8] M. Y. Y. Hung, Y. S. Chen, S. P. Ng, S. M. Shepard, Y. Hou, and J. R. Lhota, "Review and comparison of shearography and pulsed thermography for adhesive bond evaluation," *Optical Engineering*, vol. 46, no. 5, p. 051007, 2007 [Online]. Available: `http://link.aip.org/link/?JOE/46/051007/1`.

[9] J. A. Schroeder, T. Ahmed, B. Chaudhry, and S. Shepard, "Non-destructive testing of structural composites and adhesively bonded composite joints: pulsed thermography," *Composites Part A: Applied Science and Manufacturing*, vol. 33, no. 11, pp. 1511–1517, 2002 [Online]. Available: `http://www.sciencedirect.com/science/article/B6TWN-47YXF1T-6/2/bc71b40b35ddc50e5ea83126db42480d`.

[10] D. A. Scott, M. Dennis, N. Khandekar, J. Keeney, D. Carson, and L. S. Dodd, "An Egyptian cartonnage of the Graeco-Roman period: examination and discoveries," *Studies in Conservation*, vol. 48, no. 1, pp. 41–56, 2003.

[11] D. Bomford, *Art in the Making: Underdrawings in Renaissance Paintings*, ser. National Gallery London Publications. New Haven: Yale University Press, 2002.

[12] B. Berrie, E. R. de la Rie, R. Hoffman, J. Tomlinson, T. Wiesel, and J. Winter, *Scientific Examination of Art: Modern Techniques in Conservation and Analysis*. Washington DC: National Academy of Sciences, 2002.

[13] L. MacDonald, *Digital Heritage: Applying Digital Imaging to Cultural Heritage*. Amsterdam: Elsevier, 2006.

[14] C. M. Falco, "High resolution digital camera for infrared reflectography," *Review of Scientific Instruments*, vol. 80, no. 7, pp. 071 301–071 309, July 2009.

[15] A. H. Bendada, S. Sfarra, D. Ambrosini, D. Paoletti, C. Ibarra-Castanedo, and X. Maldague, "Active thermography data processing for the NDT&E of frescoes," in *Quantitative Infrared Thermography 2010*, pp. 961–966, Quebec City, Canada, July 2010.

[16] G. M. Carlomagno and C. Meola, "Comparison between thermographic techniques for frescoes NDT," *NDT & E International*, vol. 35, no. 8, pp. 559–565, 2002.

[17] K. Blessley, C. Young, J. Nunn, J. Coddington, and S. M. Shepard, "The feasibility of flash thermography for the examination and conservation of works of art," *Studies in Conservation*, vol. 55, pp. 107–120, 2010.

[18] D. Gavrilov, C. Ibarra-Castanedo, E. Maeva, O. Grube, X. Maldague, and R. Maev, "Infrared methods in noninvasive inspection of artwork," *9th International Conference on Non-destructive Testing of Art*, 2008.

[19] C. Ibarra-Castanedo, S. Sfarra, D. Ambrosini, D. Paoletti, A. Bendada, and X. Maldague, "Subsurface defect characterization in artworks by quantitative PPT," *Quantitative Infrared Thermography*, 2008.

[20] D. Ambrosini, C. Daffara, R. D. Biase, D. Paoletti, L. Pezzati, R. Bellucci, and F. Bettini, "Integrated reflectography and thermography for wooden paintings diagnostics," *Journal of Cultural Heritage*, vol. 11, no. 2, pp. 196–204, 2010.

[21] M. Lettner and R. Sablatnig, "Multispectral imaging for analyzing ancient manuscripts," *17th European Signal Processing Conference*, August 2009.

[22] K. Rapantzikos and C. Balas, "Hyperspectral imaging: potential in non-destructive analysis of palimpsests," in *IEEE International Conference on Image Processing*, vol. 2, pp. II–618–21, Sept. 2005.

[23] G. A. Ware, D. M. Chabries, and R. W. Christiansen, "Multispectral document enhancement: Ancient carbonized scrolls," *IEEE Proceedings on Geoscience and Remote Sensing Symposium*, pp. 2486–2488, 2000.

[24] R. J. Easton, K. Knox, and W. Christens-Barry, "Multispectral imaging of the Archimedes palimpsest," in *Applied Imagery Pattern Recognition Workshop*, pp. 111–116, Oct. 2003.

[25] D. Obbink, "A new Archilochus poem," *Zeitschrift für Papyrologie und Epigraphik*, vol. 156, pp. 1–9, 2006.

[26] B. Zuckerman, "Bringing the Dead Sea scrolls back to life: A new evaluation of photographic and electric imaging of the Dead Sea scrolls," *Dead Sea Discoveries*, vol. 3, no. 2, pp. 178–207, 1996.

[27] G. Bearman, B. Zuckerman, K. Zuckerman, and J. Chiu, "Multi-spectral digital imaging of Dead Sea scrolls and other ancient documents," Jet Propulsion Laboratory, Tech. Rep., 1993.

[28] J. Monaghan, G. Ware, J. Pohl, and S. Houston, "A codex imaging project at the Bodleian library: the recovery of lost mixtec writing," *Foundation for the Advancement of Meso-American Studies*, 2004.

[29] U. Bergmann and K. T. Knox, "Pseudo-color enhanced X-ray fluorescence imaging of the Archimedes Palimpsest," *Proceedings Document Recognition and Retrieval*, vol. XVI, pp. 1–10, Jan. 2009.

[30] X. P. Maldague, *Theory and Practice of Infrared Technology for Nondestructive Testing.* Hoboken: John Wiley & Sons, Inc., 2001.

[31] R. C. Gonzalez and R. E. Woods, *Digital Image Processing.* Upper Saddle River: Pearson Education, Inc., 2008.

[32] J. Zalameda, N. Rajic, and W. Winfree, "A comparison of image processing algorithms for thermal nondestructive evaluation," *SPIE Proc. Thermosense XXV*, vol. 5073, pp. 374–385, 2003.

[33] C. Ibarra-Castanedo, D. Gonzalez, M. Klein, M. Pilla, S. Vallerand, and X. Maldague, "Infrared image processing and data analysis," *Infrared Physics & Technology*, vol. 46, pp. 75–83, Apr. 2004.

[34] J. Ramirez-Granados, G. Paez, and M. Strojnik, "Reconstruction and analysis of pulsed thermographic sequences for nondestructive testing of layered materials," *Applied Optics*, vol. 49, no. 9, Mar. 2010.

[35] S. Shepard, J. Lhota, B. Rubadeux, T. Ahmed, and D. Wang, "Enhancement and reconstruction of thermographic data," *Proceedings SPIE*, vol. 4710, pp. 531–535, 2002.

[36] S. M. Shepard, "Temporal noise reduction, compression and analysis of thermographic image data sequences," Patent, 02 2003, uS 6516084 [Online]. Available: `http://www.patentlens.net/patentlens/patent/US_6516084/en/`.

[37] M. Pilla, M. Klein, X. Maldague, and A. Salerno, "New absolute contrast for pulsed thermography," *Proceedings of Quantitative Flash Thermography*, pp. 53–58, 2002.

[38] D. Gonzalez, C. Ibarra-Castanedo, M. Pilla, M. Klein, and X. Maldague, "Automated differential absolute contrast," *Quantitative Infrared Thermography*, 2004.

[39] M. Susa, H. Benitez, C. Ibarra-Castanedo, H. Loaiza, H. Bendada, and X. Maldague, "Phase contrast using a differentiated absolute contrast method," *Quantitative Infrared Thermography*, vol. 3, pp. 219–230, 2006.

[40] D. Gonzalez, C. Ibarra-Castanedo, M. Pilla, M. Klein, J. Lopez-Higuera, and X. Maldague, "Automatic interpolated differentiated absolute contrast algorithm for the analysis of pulsed thermographic sequences," in *Quantitative Infrared Thermography 7*, D. Balageas, J. Buchlin, G. Carlomagno, and G. Busse, Eds., pp. H.16.1–H.16.6, Bruxelles, Belgique, July 2004.

[41] H. Benitez, C. Ibarra-Castanedo, A. Bendada, X. Maldague, H. Loaiza, and E. Caicedo, "Definition of a new thermal contrast and pulse correction for defect quantification in pulsed thermography," *Infrared Physics & Technology*, vol. 51, pp. 160–167, 2008.

[42] C. Ibarra-Castanedo, H. Benitez, X. Maldague, and A. Bendada, "Review of thermal-contrast-based signal processing techniques for the nondestructive testing and evaluation of materials by infrared thermography," *International Workshop on Imaging Nondestructive Evaluation*, 07.

[43] H. Benitez, X. Maldague, C. Ibarra-Castanedo, H. Loaiza, A. Bendada, and E. Caicedo, "Modified differential absolute contrast using thermal quadrupoles for the nondestructive testing of finite thickness specimens by infrared thermography," in *Electrical and Computer Engineering, 2006. CCECE '06. Canadian Conference on*, pp. 1039–1042, may 2006.

[44] X. Maldague and S. Marinetti, "Pulse phase infrared thermography," *Journal of Applied Physics*, vol. 79, no. 5, pp. 2694–2698, mar 1996.

[45] M. A. Omar and Y. Zhou, "A quantitative review of three flash thermography processing routines," *Infrared Physics & Technology*, vol. 51, no. 4, pp. 300–306, 2008 [Online]. Available: `http://www.sciencedirect.com/science/article/B6TJ9-4R0643G-2/2/1012d8792b0b432e3dfd2514330f125c`.

[46] G. Busse, D. Wu, and W. Karpen, "Thermal wave imaging with phase sensitive modulated thermography," *Journal of Applied Physics*, vol. 71, no. 8, pp. 3962–3965, apr 1992.

[47] X. Maldague, F. Galmiche, and A. Ziadi, "Advances in pulsed phase thermography," *Infrared Physics & Technology*, vol. 43, pp. 175–181, 2002.

[48] C. Ibarra-Castanedo and X. Maldague, "Defect depth retrieval from pulsed phase thermographic data on plexiglas and aluminum samples," *SPIE Proc. Thermosense XXVI*, vol. 5405, 2004.

[49] D. Gonzalez, C. Ibarra-Castanedo, F. Madruga, and X. Maldague, "Differentiated absolute phase contrast algorithm for the analysis of pulsed thermographic sequences," *Infrared Physics & Technology*, vol. 48, pp. 16–21, 2006.

[50] M. Klein, A. Bendada, C. Ibarra-Castanedo, and X. Maldague, "A hybrid pulsed thermography processing technique for the depth estimation of subsurface defects combining TSR and PPT," *10th International Conference on Quantitative Infrared Thermography*, 2010.

[51] S. M. Shepard. (2007, October) Flash thermography of aerospace composites [Online]. Available: http://www.ndt.net/article/panndt2007/papers/132.pdf.

[52] S. M. Shepard, J. R. Lhota, B. A. Rubadeux, D. Wang, and T. Ahmed, "Reconstruction and enhancement of active thermographic image sequences," *Optical Engineering*, vol. 42, no. 5, May 2003.

[53] J. G. Sun, "Analysis of pulsed thermography methods for defect depth prediction," *Journal of Heat Transfer*, vol. 128, no. 4, pp. 329–338, 2006.

[54] S. M. Shepard, "Understanding flash thermography," *Materials Evaluation*, pp. 460–464, May 2006.

[55] S. M. Shepard, J. Hou, J. R. Lhota, and J. M. Golden, "Automated processing of thermographic deriviatives for quality assurance," *Optical Engineering*, vol. 46, no. 5, May 2007.

[56] N. Rajic, "Principal component thermography for flaw contrast enhancement and flaw depth characterisation in composite structures," *Composite Structures*, vol. 58, no. 4, pp. 521–528, 2002 [Online]. Available: http://www.sciencedirect.com/science/article/B6TWP-472841H-9/2/4c29e1491d0beb293d9a3811ed9498b8.

[57] N. Rajic, "Principal component thermography," Defense Science and Technology Organisation Victoria (Australia) Aeronautical and Maritime Research Laboratory, Tech. Rep. 012-294, Apr. 2002.

[58] V. Vavilov, D. Nesteruk, V. Shiryaev, A. Ivanov, and W. Swiderski, "Thermal (infrared) tomography: terminology, principal procedures, and application to nondestructive testing of composite materials," *Russian Journal of Nondestructive Testing*, vol. 46, no. 3, pp. 151–161, 2010.

[59] V. P. Vavilov, "Dynamic thermal tomography: perspective field of thermal NDT," S. A. Semanovich, Ed., vol. 1313, no. 1, pp. 178–182. SPIE, 1990 [Online]. Available: http://link.aip.org/link/?PSI/1313/178/1.

[60] W. Swiderski, "The characterization of defects in multi-layered composite materials by thermal tomography methods," in *Proceedings of the Tenth Annual Conference of the Materials Research Society of Serbia*, vol. 115, no. 4, pp. 800–804, 2009.

[61] B. Sun, Q. Ma, and H. Zhao, "Fitting-correlation analysis of pulsed thermographic sequence data," in *Proceedings of the 2007 IEEE International Conference on Mechatronics and Automation*, Aug. 2007.

[62] M. Klein, C. Ibarra-Castanedo, A. H. Bendada, and X. Maldague, "Thermographic signal processing through correlation operators in pulsed thermography," in *Thermosense XXX, SPIE Defense and Security Symposium*, V. P. Vavilov and D. D. Burleigh, Eds., vol. 6939, p. 693915, Orlando, Florida, USA, Vol. 6939, March 16-20 2008.

[63] D. Gonzalez, C. Ibarra-Castanedo, J. Lopez-Higuera, and X. Maldague, "New algorithm based on the Hough transform for the anlaysis of pulsed thermographic sequences," *Nondestructive Testing and Evaluation International*, vol. 39, pp. 617–621, 2006.

[64] C. Ibarra-Castanedo, D. Gonzalez, F. Galmiche, X. Maldague, and A. H. Bendada, "Discrete signal transforms as a tool for processing and analyzing pulsed thermographic data," in *SPIE - The International Society for Optical Engineering, Thermosense XXVIII*, vol. 6205, pp. 620 514–1–620 514–12, Orlando, FL, 2006.

[65] D. de Cogan, A. Soulos, and K. Chichlowski, "Sub-surface feature location and identification using inverse TLM techniques," *Microelectronics Journal*, vol. 29, pp. 215–22, 1998.

[66] D. de Cogan, W. J. O'Connor, and S. Pulko, *Transmission Line Matrix in Computational Mechanics*. Boca Raton: Taylor and Francis, 2006.

[67] D. Crowther, L. Favro, P. Kuo, and R. Thomas, "Inverse scattering algorithm applied to infrared thermal waves," *J. Appl. Phys.*, vol. 74, no. 9, pp. 5828–5835, Nov 1993.

[68] Favro, L. D., Han, X., Kuo, P. K., and Thomas, R. L., "Improving the resolution of pulsed thermal wave images with a simple inverse scattering technique," *Journal De Physique IV France*, vol. 04, pp. C7–545–C7–550, 1994.

[69] L. Favro, D. Crowther, P. Kuo, and R. Thomas, "Inversion of pulsed thermal-wave images for defect sizing and shape recovery," *Thermosense XIV: An International Conference on Thermal Sensing and Imaging Diagnostic Applications*, vol. 1682, pp. 178–181, 1992.

[70] N. S. Goel and F. Gang, "A simple method for pulse-echo thermal wave imaging of arbitrary shaped subsurface scatterers in heterogeneous materials," *International Communications in Heat Mass Transfer*, vol. 23, no. 1, pp. 45–54, 1996.

[71] R. Thomas, L. Favro, and P. Kuo, "Thermal wave imaging of hidden corrosion," Wayne State University, Tech. Rep. F49620-96-1-0166, Mar. 1998.

[72] M. Omar, H. Hassan, and K. Saito, "Optimizing thermography depth probing with a dynamic thermal point spread function," *Infrared Physics & Technology*, vol. 46, pp. 506–514, 2005.

[73] T. D'Orazio, C. Guaragnella, M. Leo, and P. Spagnolo, "Defect detection in aircraft composites by using a nerual appoach in the analysis of thermographic sequences," *Nondestructive Testing and Evaluation International*, vol. 38, pp. 665–673, 2005.

[74] D. Maillet, J. Batsale, A. Bendada, and A. Degiovanni, "Methodes integrales et controle non destructif par thermographie infrarouge," *Revue Générale de Thermique*, vol. 35, pp. 14–27, 1996.

[75] A. Bendada, F. Erchiqui, and M. Lamontagne, "Pulsed thermography in the evaluation of an aircraft composite using 3D thermal quadrupoles and mathematical perturbations," *Inverse Problems*, vol. 21, pp. 857–577, 2005.

[76] V. Vavilov, *IR Thermography and Nondestructive Testing.* Moscow: Spektr, 2009.

[77] J. Sun, "Method for determining defect depth using thermal imaging," Patent, 04 2002, US 6542849.

[78] N. Rajic, "A quantitative approach to active thermographic inspection for material loss evaluation in metallic structures," *Research in Nondestructive Evaluation*, vol. 12, no. 2, pp. 119–131, 2000.

[79] V. Vavilov, X. Maldague, B. Dufort, and A. Ivanov, "Adaptive thermal tomography algorithm," *Proceedings SPIE Thermosense-XV*, no. 1933, pp. 166–173, 1993.

[80] H. Benitez, H. Loaiza, E. Caicedo, C. Ibarra-Castanedo, A. Bendada, and X. Maldague, "Defect characterization in infrared non-destructive testing with learning machines," *Nondestructive Testing & Evaluation International*, vol. 42, pp. 630–643, 2009.

[81] I. Abdel-Qader, S. Yohali, O. Abudayyeh, and S. Yehia, "Segmentation of thermal images for non-destructive evaluation of bridge decks," *Nondestructive Testing & Evaluation International*, vol. 41, no. 5, pp. 395–405, 2008.

[82] V. F. Bakirov, R. A. Kline, and W. P. Winfree, "Multiparameter thermal tomography," *AIP Conference Proceedings*, vol. 700, no. 1, pp. 461–468, 2004.

[83] V. Bakirov, R. Kline, and W. Winfree, "Diffusion based thermal tomography," *Nondestructive Evaluation and Reliability of Micro and Nonomaterial Systems*, vol. 4703, pp. 219–225, 2002.

[84] V. F. Bakirov and R. A. Kline, "Diffusion-based thermal tomography," *Journal of Heat Transfer*, vol. 127, no. 11, pp. 1276–1279, 2005.

[85] F. Ammirato and P. Zayicek, "Infrared thermography field application guide," Electric Power Research Institute, Inc., Palo Alto, CA, Tech. Rep. TR-107142, Jan. 1999.

[86] M. Klein, C. Ibarra-Castanedo, X. Maldague, and A. H. Bendada, "IR-View: a straightforward graphical user interface for basic and advanced signal processing of thermographic infrared sequences," in *Thermosense XXX, SPIE Defense and Security Symposium*, V. P. Vavilov and D. D. Burleigh, Eds., vol. 6939, p. 693914, Orlando, Florida, USA, Vol. 6939, March 16-20 2008.

[87] S. Shepard, J. Lhota, and T. Ahmed, "Flash thermography contrast model based on IR camera noise characteristics," *Nondestructive Testing and Evaluation*, vol. 22, no. 2-3, pp. 113–126, 2007.

[88] V. Vavilov, "Pulsed thermal NDT of materials: back to the basics," *Nondestructive Testing and Evaluation*, vol. 22, no. 2-3, pp. 177–197, June 2007.

[89] P. Zayicek, "Infrared thermography guide (revision 3)," Electric Power Research Institute, Inc., Tech. Rep. 1006534, 2002.

[90] X. Maldague, *Nondestructive Evaluation of Materials by Infrared Thermography*. London: Springer-Verlag, 1993.

[91] J. Krapez, D. Balegeas, A. Deom, and F. Lepoutre, "Early detection by stimulated infrared thermography," in *Advances in Signal Processing for Nondestructive Evaluation of Materials*, X. Maldague, Ed., pp. 303–321. The Netherlands: Kluwer Academic Published, 1994.

[92] J. R. Lhota and S. M. Shepard, "Critical timing issues in flash thermography," D. O. Thompson and D. E. Chimenti, Eds., vol. 760, no. 1, pp. 1654–1660. AIP, 2005 [Online]. Available: `http://link.aip.org/link/?APC/760/1654/1`.

[93] U. Netzelmann, "Optimized temporal excitation profiles in active thermography," *Analytical Sciences*, vol. 17, pp. 432–435, Apr. 2001.

[94] X. Maldague, Z. Ziadi, and M. Klein, "Double pulse infrared thermography," *Nondestructive Testing and Eval. Int.*, vol. 37, pp. 559–564, 2004.

[95] A. Daniels, "Optimization of pulsed temporal stimulation for thermal nondestructive testing," in *Thermosense XX SPIE*, J. Snell and R. Wurzbach, Eds., vol. 3361, pp. 254–265, 2001.

[96] H. Carslaw and J. Jaeger, *Conduction of Heat in Solids*, 2nd ed. Oxford: Claredon Press, 1986.

[97] K. Wan and Q. Ma, "Data-fitting reconstruction for defect inspection of airplane aluminum structure in infrared thermographic NDT," in *Industrial Electronics and Applications, 2009. ICIEA 2009. 4th IEEE Conference on*, pp. 691–696, may 2009.

[98] H. Ringermacher, D. Mayton, D. Howard, and B. Cassenti, "Towards a flat-bottom hole standard for thermal imaging," *Review of Progress in Quantitative Nondestructive Evaluation*, vol. 17, pp. 425–9, 1998.

[99] M. Omar, M. Hassan, K. Saito, and R. Alloo, "IR self-referencing thermography for detection of in-depth defects," *Infrared Physics & Technology*, vol. 46, pp. 283–289, 2005.

[100] T. A. Griffiths, "Enhancing multispectral imagery of ancient documents," Master's thesis, Utah State University, 2011.

[101] B. Foy, "Overview of target detection algorithms for hyperspectral data," Los Alamos National Laboratory, Tech. Rep. LA-UR-09-00593, June 2009.

[102] D. Manolakis, "Taxonomy of detection algorithms for hyperspectral imaging applications," *Optical Engineering*, vol. 44, no. 6, pp. 066 403–1–066 403–11, June 2005.

[103] M. E. Smith, "Codex selden: A manuscript from the Valley of Nochixlan," in *The Cloud People: Divergent evolution of the Zapotec and Mixtec civilizations*, K. Flannery and J. Marcus, Eds., pp. 248–255. New York: Academic Press, 1984.

[104] M. E. Smith, "Why the second Codex Selden was painted," in *Caciques and their people*, J. Marcus and J. F. Zeitlin, Eds., vol. 89, pp. 111–142. Anthropological Papers, 1994.

[105] P. Dark and J. Plesters, "The palimpsests of Codex Selden: Recent attempts to reveal the covered pictographs," *33rd Annual International Congress of Americanists*, vol. 2, pp. 530–539, 1958.

[106] G. A. Ware, "Codex selden feasibility study: multispectral and infrared images," Brigham Young University, Tech. Rep., 2005.

Appendices

Appendix A

Pulsed Thermography Toolbox

A.1 Pulsed Thermography Toolbox (PTT) Introduction

The Pulsed Thermography Toolbox (PTT) was developed as part of this research to aid in the application of pulsed thermography to ancient documents and archaeological artifacts. The toolbox provides the processing techniques discussed in Chapter 4 in a easy-to-use graphical user interface (GUI). The code was developed and implemented in MATLAB R2010b. The main GUI interface can be seen in Figure A.1. The GUI subcomponents will be discussed in detail throughout this chapter.

A.2 Load Images

The load image sub-panel is shown in Figure A.2. Three data types can be selected: tagged image file format (*.tif* or *.tiff*), a proprietary binary format develop by the Space Dynamics Lab (*.sbf*), or a MATLAB binary (*.mat*) file type.

After selecting the desired image format, click the `Load Images` button and a file selection window (Figure A.3) will appear.

If the `TIF` radial button is selected, it will prompt selection of a directory containing the *.tif* files and will load the files within that directory in alphabetical order. If the `SDL Binary` or `MATLAB Binary (.mat)` options are selected, the file selection window will prompt selection of select a single *.sbf* or *.mat* file, respectively. Note that in order for the MATLAB binary to be properly loaded, it must contain two matrices. The first matrix must be called *imageCube* and contain the pulsed thermography data in a M×N×T array, where M×N are the dimensions of each frame and T is the number of frames. In addition, the MATLAB binary must contain a single M×N matrix containing the pre-flash image

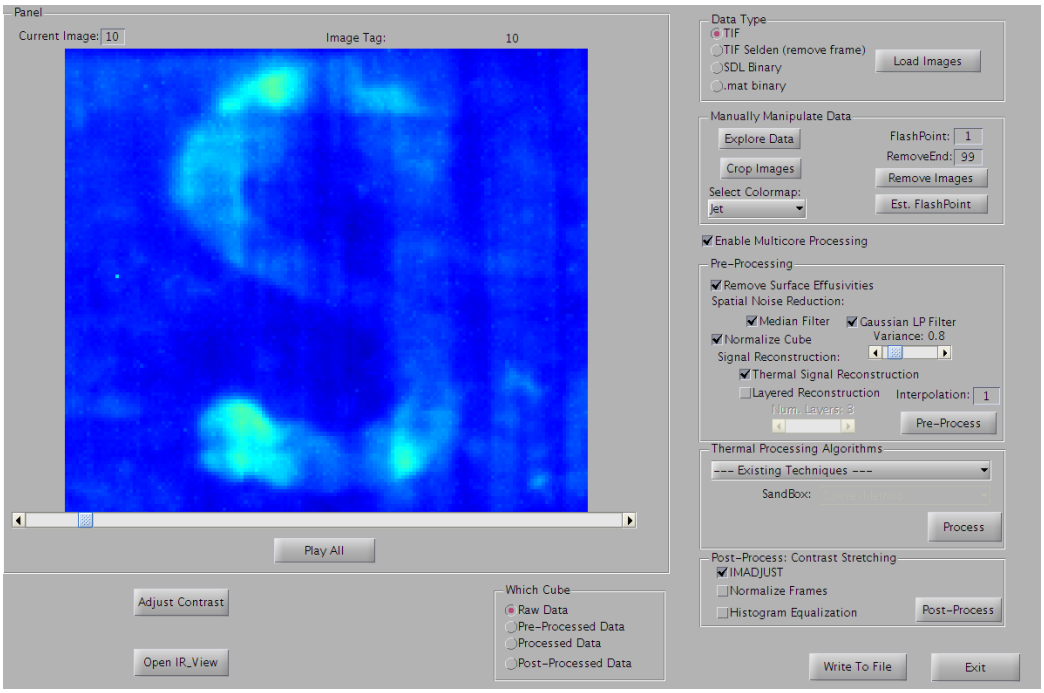

Fig. A.1: Pulsed Thermography Toolbox main GUI.

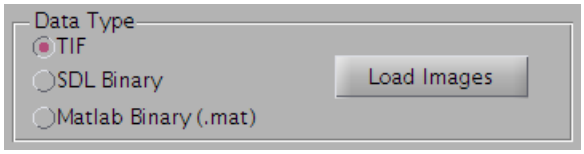

Fig. A.2: Load images panel.

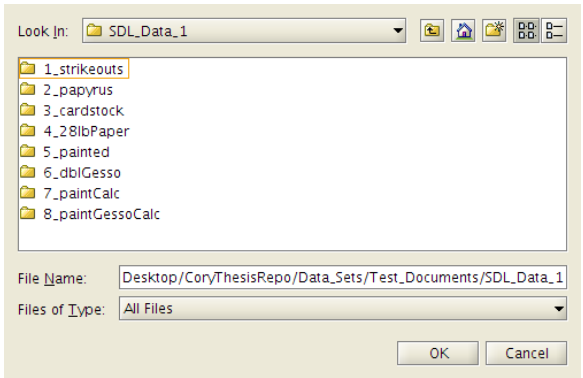

Fig. A.3: Select files interface.

with the variable name *preflash*. After the data are loaded, the first image of the data set will be shown on the Display Panel (Figure A.4).

The Display Panel features a slider that controls which frame is currently displayed. The `Play All` button iterates through every frame showing the video sequence. Finally, the image number is displayed in the upper left, and the image tag information is displayed in the upper right.

A.3 Manually Manipulate Data Panel

The Manually Manipulate Data Panel is shown in Figure A.5 and provides a variety of features for exploring and manipulating the data manually. The `Explore Data` button brings up the Explore Data Sub-GUI as discussed in Section A.8.

The `Crop Images` button allows each frame in the data set to be cropped. After clicking the `Crop Images` button, the image corresponding to the number in the `FlashPoint` edit box will be displayed allowing selection of a rectangular region on the image displayed in the Display Panel. After selecting the region to keep, right-click on the image and select the `Crop Image` item from the drop-down menu. Each image frame will be cropped to the specified dimensions.

The `Select Colormap` drop-down box allows the user to select the colormap to be used in creating the false color images (see Section 4.2.1). To view the original grayscale intensity images, select the `Grayscale` option from the drop-down box.

The `FlashPoint` and `RemoveEnd` edit boxes are initialized with the length of the data. These boxes allow for the data set to be reduced in length. Changing the number in the `FlashPoint` edit box allows removal of any images before that point (pre-flash images). By changing the number in the `RemoveEnd` edit box, the total number of frames can be reduced. After entering the desired parameters, press the `Remove Images` button to apply the actions. Note that when changing the `Flashpoint`, the third previous image will be saved as the pre-flash image used for future calculations. Finally, the `Est. FlashPoint` button can be used to automatically detect the flash point, give an estimation of the length

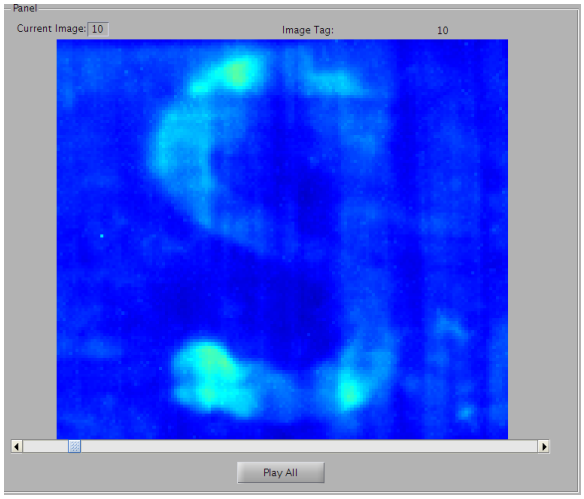

Fig. A.4: Display panel.

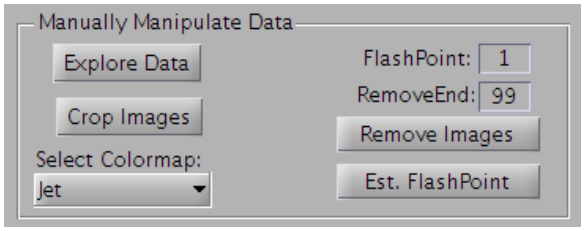

Fig. A.5: Manually Manipulate Data Panel.

of data needed, and update these values in the `FlashPoint` and `RemoveEnd` edit boxes, respectively.

A.4 Pre-Processing Panel

The Pre-Processing Panel, shown in Figure A.6, provides useful pre-processing routines. Recommended settings are pre-selected. The `Remove Surface Effusivities` subtracts the pre-flash image from each image in the data set to reduce the effects of differences in surface effusivity values. The `Spatial Noise Reduction` selects the image filters discussed in Section 4.2.4. Both the filters use a 3×3 window. The variance of the Gaussian filter, which affects the amount of blurring, can be changed using the slider box labeled `Variance`. The `Normalize Cube` checkbox allows for the entire data set to be re-normalized between 0 and 1. This is useful when the data set does not fill the entire range due to the median filter removing dead pixels or other abnormalities. Finally, the `Signal Reconstruction` provides a choice between the synthetic signal reconstruction techniques discussed in Section 4.2.5. When `Layered Reconstruction` is selected, the number of layers to use in reconstruction can be changed using the `Num. Layers` slider. In addition, the reconstructed signal can be modified using the `Interpolation` edit box. An interpolation factor of 2 will up-sample the signal by double. Similarly, an interpolation factor of 0.5 will down-sample the signal by one half. When all the chosen pre-processing techniques have been selected, click the `Pre-Process` button to apply them to the data set.

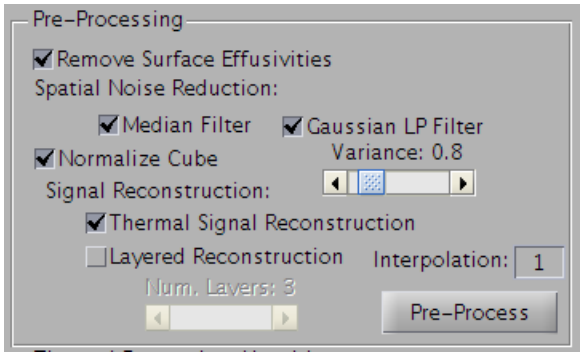

Fig. A.6: Pre-Processing Panel.

A.5 Processing Panel

The Processing Panel is shown in Figure A.7 and allows for the operator to choose a desired processing algorithm as discussed in Chapter 4. When the desired algorithm is chosen, click the `Process` button to apply the algorithm to the data set. One of the options in the drop-down box is `### Sandbox ###`. When this option is selected, the `Sandbox` drop-down menu is enabled. This drop-down menu is automatically populated with any functions located in the *sandbox/* directory. Choose any of the functions in the sandbox drop-down menu and click `Process` to run the selected algorithm. Note that any algorithm placed in the *sandbox/* directory is required to have a standard header with a single input and two outputs. The input is an image cube of the input data with dimensions M×N×T. The outputs are a processed data cube M×N×R and a cell array of string image descriptors of length R. This facilitates straightforward testing of new processing routines which can be easily incorporated into the existing GUI.

A.6 Post-Processing Panel

The Post-Processing Panel is seen in Figure A.8 and provides the three contrast stretching routines discussed in Sections 4.2.2 and 4.2.3. After selecting the desired post-processing technique, click `Post-Process` button to apply to the data set.

A.7 Other GUI Sub-Components

There are several other GUI sub-components. The `Which Cube` panel allows for the selection between data sets at different stages of processing. The `Enable Multicore Processing` makes it possible for MATLAB to use four processors when processing the

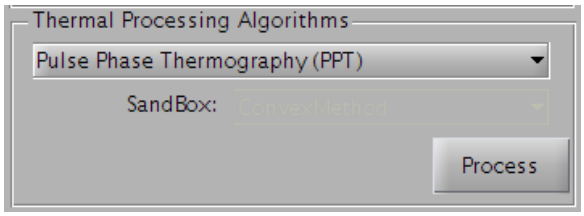

Fig. A.7: Processing Panel.

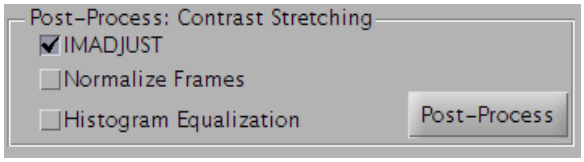

Fig. A.8: Post-Processing Panel.

data. The `Adjust Contrast` button displays the histogram of the currently displayed image frame and allows for manual histogram manipulation. The `Open IR View` passes the data to the IR View toolbox, a previously existing open-source toolbox for processing thermal data. Note that the IR View toolbox was made for a previous version of MATLAB and not all of the functions work correctly. The `Write To File` outputs the currently selected data to file in the *results/[algorithm name]/* directory in *.tif* format. The filenames are generated from the image tag cell array. Finally, the `Exit` button closes the GUI and disables the multi-core processing nodes created by MATLAB.

A.8 Explore Data Sub-GUI

The Explore Data Sub-GUI is launched when the `Explore Data` button is selected in the Manually Manipulate Data Panel. This sub-GUI is shown in Figure A.9 and allows for the visualization of the temperature decay sequences. It contains four image panels: the current frame (upper right), the selected pixel time sequence (upper left), the selected pixel time sequence in log domain (lower left), and the Fourier Transform of the selected pixel time sequence (lower right). Four models for reconstructing or fitting to the data are available for analysis: thermal signal reconstruction, Markov model, layered reconstruction, and reverse transmission line matrix models. Also, the optional `Show Neighbors` check box replaces the Fourier transform with the selected pixel's time sequence and the time sequence of it's immediate spatial neighbors. Selecting the `Run` button will allow the operator to choose a desired pixel to plot. The `Save Series` button will save the currently displayed pixel time series to a MATLAB *.mat* binary. Finally, the `Exit` button will close the sub-GUI.

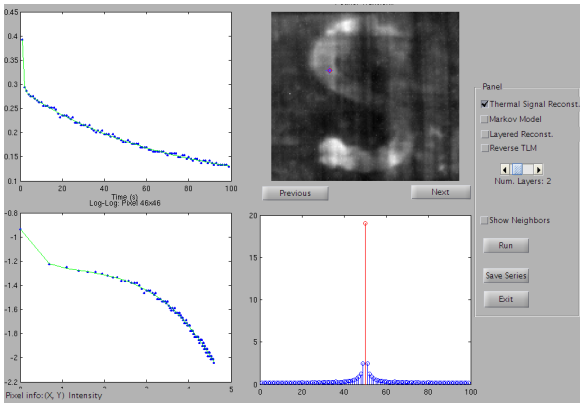

Fig. A.9: Explore Data Sub-GUI.

Appendix B

Code Listings

The listings for the main processing techniques are given.

B.1 Contrast Definitions & Differential Absolute Contrast (DAC)

```
function [ outCube outTags CtrstDef ] = ContrastImages( imageCube
    , T_to)
% CONTRASTIMAGES Allows selection between Absolute, Running,
    Normalized,
% and Standard contrast definitions.  In addition, differential
    absolute
% contrast (DAC) is also selectable.
%
% [U V W] = ContrastImages(X, Y) Input X is a 3D
% imageCube of dimension MxNxT, where MxN are the frame size and
    T is the
% number of frames.  Input Y is a pre-flash frame of dimensions
    MxN. Output
% U is the processed image cube, V is the image tag information
    associated
% with each frame, and W is the selection of which contrast
    definition was
% chosen.
%
% Reference Paper(s):
```

```
% 1) X. P. Maldague, Theory and Practice of Infrared Technology
    for
% Nondestructive Testing. John Wiley & Sons, Inc., 2001.
% 2) M. Pilla, M. Klein, X. Maldague, and A. Salerno, "New
    absolute
% contrast for pulsed thermography," Proceedings of Quantitative
    Flash
% Thermography, pp. 53-58, 2002.
%
%
% See also GETPOSITION.
%
% PULSED THERMOGRAPHY PROCESSING TOOLBOX
% Author: Cory Andrew Larsen

fprintf('Running Contrast Images Algorithm...\n')

[Nx Ny Nt] = size(imageCube);

fprintf('Select Definition of Contrast to Use:\n');
fprintf('1) Absolute Contrast\n');
fprintf('2) Running Contrast\n');
fprintf('3) Normalized Contrast (using final value)\n');
fprintf('4) Normalized Contrast (using maximal value)\n');
fprintf('5) Standard Contrast \n');
fprintf('6) Differentiated Absolute Contrast (DAC)\n');
fprintf('\n');
select = input('Which Definition to Use?\n');
```

```
if(select < 1 || select > 6)
    fprintf('Error: Invalid Selection. Choose a number between 1
       & 7\n');
    select = input('Which Definition to Use?\n');
end

if(select < 6)
    fprintf('Choose Background Pixels: ');
    fprintf('Select 5 Points...');
    Tsnd =  0;
    Tsnd_to = 0;
    for nn=1:5
        h = impoint;
        pos = getPosition(h);
        py = round(pos(1));
        px = round(pos(2));
        Tsnd = Tsnd + imageCube(px,py,:);
        Tsnd_to = Tsnd_to + T_to(px,py);
    end
    Tsnd = permute(Tsnd/5,[3,1,2]);
    Tsnd_to = Tsnd_to/5;
    fprintf('done.\n');
end

if(select == 6)
    tp = input('Enter time index of when first defect appears:  '
       );
    delta_Ttp = imageCube(:,:,tp) - T_to;
```

```
end

tic;

% Define Time Instances
T_f = imageCube(:,:,end);
T_tm = imageCube(:,:,1);

% Initialize Arrays
AbsCtrst = zeros(Nx,Ny,Nt); RunCtrst = AbsCtrst; NormCtrstA =
    AbsCtrst;
NormCtrstB = AbsCtrst; StdCtrst = AbsCtrst; DAC = AbsCtrst; CM =
    AbsCtrst;
for tt=1:Nt
    T = imageCube(:,:,tt);
    switch select
        case 1
            %-- Absolute Contrast --%
            Ca = T-Tsnd(tt);
            idx = Ca < 0;
            Ca(idx) = 0;
            AbsCtrst(:,:,tt) = Ca;
        case 2
            %-- Running Contrast --%
            Cr = (T-Tsnd(tt))/Tsnd(tt);
            idx = Cr < 0;
            Cr(idx) = 0;
            RunCtrst(:,:,tt) = Cr;
```

```
        case 3
            %-- Normalized Contrast A--%
            Cn1 = T./T_f - Tsnd(tt)/Tsnd(end);
            NormCtrstA(:,:,tt) = Cn1;
        case 4
            %-- Normalized Contrast B--%
            Cn2 = T./T_tm - Tsnd(tt)/Tsnd(1);
            NormCtrstB(:,:,tt) = Cn2;
        case 5
            %-- Standard Contrast --%
            Cs = (T-T_to) / (Tsnd(tt) - Tsnd_to);
            StdCtrst(:,:,tt) = Cs;
        case 6
            %-- Differentiated Absolute Contrast (DAC) --%
            delta_T = T - T_to;
            DAC(:,:,tt) = delta_T - sqrt(tp/tt) * delta_Ttp;
    end
end

%-- Store Data for Output --%
switch select
    case 1
        outCube = AbsCtrst;
        CtrstDef = 'Abs';
    case 2
        outCube = RunCtrst;
        CtrstDef = 'Run';
    case 3
```

```
        outCube = NormCtrstA;
        CtrstDef = 'Normf';
    case 4
        outCube = NormCtrstB;
        CtrstDef = 'Normi';
    case 5
        outCube = StdCtrst;
        CtrstDef = 'Std';
    case 6
        outCube = DAC;
        CtrstDef = ['DAC' int2str(tp)];
end

outTags = genNumTags(outCube);

toc;
DisplayTime(toc);
fprintf('Contrast Images Complete!\n');

end
```

B.2 Thermal Signal Reconstruction (TSR) and Derivative Images

```
function [f df ddf] = tsr(imageCube,order)
% TSR Thermal Signal Reconstruction algorithm for pulsed
    thermography
% data. The algorithms removes temporal noise in the data by
    using a log
```

```
% transformation and a polynomial fit.  It then takes the first
    and second
% derivatives of the polynomial functions to increase the
    contrast of
% defects.
%
% [F DF DDF] = TSR(X) Process 3-D image cube X and results
% in F, DF, and DDF.  F, DF, and DDF are the reconstructed images
    , the
% first derivative images, and the second derivative images,
    respectively.
% X, F, DF, and DDF are U by V by W, where U and V are the
    dimensions of
% each image frame and W is the number of frames.
%
% [F DF DDF] = TSR(X,N) Process X using an Nth order polynomial
    fit.
% Default is 6th order.
%
% Reference Paper(s):
% 1) S. M. Shepard, "Temporal noise reduction, compression and
    analysis
% of thermographic image data sequences," Patent, 02 2003, US
    6516084.
% 2) S. M. Shepard, J. R. Lhota, B. A. Rubadeux, D. Wang, and T.
    Ahmed,
% "Reconstruction and enhancement of active thermographic image
    se-
```

```
% quences," Optical Engineering, vol. 42, no. 5, May 2003.
%
% See also POLYFIT,POLYVAL.
%
% PULSED THERMOGRAPHY PROCESSING TOOLBOX
% Author: Cory Andrew Larsen

tic;

% Get Dimensions
[Nx Ny Nt] = size(imageCube);
M = Nx*Ny;

imageMat = reshape(imageCube,M,Nt);

% nth order polynomial for coefficients
if(nargin>2)
    nth_order = order;
else
    nth_order=6;
end

% declare time
t=(1:Nt);
%% Take Natural Logs of pixel and time data
% I(t)_i,j = ln[I(t)_i,j]
logI = zeros(M,Nt);
parfor nn=1:M
```

```
    logI(nn,:) = log(imageMat(nn,:));
end
logt=log(t);

fprintf('Smoothing Data...\n');
%% Least Squares Fit
% ln[I(t)_i,j] = a0 + a1*ln(t) + a2*ln(t)^2 + ... + an*ln(t)^n
Icoeff = zeros(M,nth_order+1);
parfor nn=1:M
    Icoeff(nn,:) =  polyfit(logt,logI(nn,:),nth_order);
end



%% Regenerate f(t)
f = zeros(M,Nt);
parfor nn=1:M
    f(nn,:) = exp(polyval(Icoeff(nn,:),logt));
end

fprintf('Take Derivatives...\n');
%% Find f'(t)
h = 1./t;
df = zeros(M,Nt);
g = zeros(M,Nt);
for nn=1:M
    Icoeff(nn,:) = flipud(Icoeff(nn,:));
    for i=1:nth_order
        g(nn,:) = g(nn,:) + i*Icoeff(nn,i+1)*logt.^(i-1);
```

```
    end
    df(nn,:) = h.*g(nn,:).*f(nn,:);

end



%% Find f''(t)
ddf = zeros(M,Nt);
gp = zeros(M,Nt);
for nn=1:M
        for i=2:nth_order
            gp(nn,:) = gp(nn,:) + i*(i-1)*Icoeff(nn,i+1)*logt.^(i
                -2);
        end
        ddf(nn,:) = h.^2.*f(nn,:).*(g(nn,:).^2-g(nn,:)+gp(nn,:));
end



% Transform back to standard form
f = imnorm(reshape(f,[Nx Ny Nt]));
df = imnorm(reshape(df,[Nx Ny Nt]));
ddf = imnorm(reshape(ddf,[Nx Ny Nt]));

toc;
DisplayTime(toc);
fprintf('TSR Complete!\n');
```

B.3 Principal Component Thermography (PCT)

```
function [outCube outTags] = pct(imageCube)
% PCT Principal Component Thermography algorithm for pulsed
    thermography
% data. The algorithm uses singular value decomposition to reduce
     the data
% to a statistical representation of spatial and temporal
    variations
% relating to the underlying structure of the sample.
%
% [Y TAGS] = PCT(X) Process 3-D image cube X and results in Y, a
    3-D image
% cube containing the first 10 empirical orthogonal functions (
    EOF). X
% is U by V by W, where U and V are the dimensions of each image
    frame and
% W is the number of frames. Y is U by V by 10. TAGS is a vector
    of cell
% arrays containing a text description of each output frame.
%
% Reference Paper(s):
% 1) N. Rajic. Principal component thermography for flaw contrast
     enhancement
% and flaw depth characterisation in composite structures.
    Composite Structures,
% 58(4):521-528, 2002.
%
```

```
% 2) N. Rajic. Principal Component Thermography. Tech note DSTO-
    TR-1298
%
% See also SVD, FIXCUBE.
%
% PULSED THERMOGRAPHY PROCESSING TOOLBOX
% Author: Cory Andrew Larsen
tic;
fprintf('Principal Component Thermography (PCT) Algorithm
    Beginning...\n');
addpath('../lib/');

% find dimensions
[Nx Ny Nt] = size(imageCube);
M = Nx*Ny;
N = Nt;

% Reshape into 2D M*N array
A = reshape(imageCube,M,N)';
clear imageCube

% Standardize
mew = mean(A);
sigma = std(A);
for m=1:M
    A(:,m) = (A(:,m) - mew(m)) / sigma(m);
end
clear mew sigma
```

```
% Make sure there are no NaN or INF in Cube
A = fixCube(A);

% Perform singular value decomposition (SVD)
[U Gamma V] = svd(A', 'econ');

% Transform U into original cube shape
outCube = reshape(U,Nx,Ny,Nt);

outTags = genNumTags(outCube);

toc;
DisplayTime(toc);
fprintf('Principal Component Thermography (PCT) Algorithm
    Complete!\n');
```

B.4 Dynamic Thermal Tomography (DTT)

```
function [outCube outTags] = dtt(imageCube)
% DTT Dynamic Thermal Tomography Algorithm. Performs both the
    classical and the
% reference-free algorithm variants.
%
% [Y T] = IMNORM(X) Processes input 3-D image cube X, and returns
     the
% processed 3-D image cube Y and image description tags in T.  X
    and Y are
```

```
% U by V by W matrix, where U and V are the dimensions of each
    image frame
% and W is the number of frames (for Y, W=4). T is a vector of
    cell arrays containing
% strings describing each image frame and is of length 4.
%
% Reference Papers:
% 1) V. Vavilov, D. Nesteruk, V. Shiryaev, A. Ivanov, and W.
    Swiderski,
% "Thermal (infrared) tomography: Terminology, principal
    procedures, and
% application to nondestructive testing of composite materials,"
    Russian
% Journal of Nondestructive Testing, vol. 46, no. 3, pp. 151-161,
     2010.
% 2) V. P. Vavilov, "Dynamic thermal tomography: perspective
    field of
% thermal ndt," S. A. Semanovich, Ed., vol. 1313, no. 1. SPIE,
    1990, pp.
% 178-182.
% 3) W. Swiderski, "The characterization of defects in multi-
    layered compos-
% ite materials by thermal tomography methods," in Proceedings of
     the
% Tenth Annual Conference of the Materials Research Society of
    Serbia,
% vol. 115, no. 4, 2009.
%
```

```
%
% See also POLYFIT, IMPOINT, IMNORM
%
% PULSED THERMOGRAPHY PROCESSING TOOLBOX
% Author: Cory Andrew Larsen

addpath('../lib/');
fprintf('Running Dynamic Thermal Tomography (DTT) Algorithm...\n'
    );
% tic;
% find dimensions
[Nx Ny Nt] = size(imageCube);

% Normalize with respect to first frame
Tn = zeros(Nx,Ny,Nt);
for nn=1:Nt
    Tn(:,:,nn) = imageCube(:,:,nn)./imageCube(:,:,1);
end
clear imageCube

%% Classical Approach
%Select reference points and average
fprintf('Select 5 Background Points...');
Tref =  0;
for nn=1:5
    h = impoint;
    pos = getPosition(h);
    py = round(pos(1));
```

```
    px = round(pos(2));
    Tref = Tref + Tn(px,py,:);
end
% Tref = permute(Tref,[3,1,2])/5;
Tref = Tref/5;
fprintf('done. Processing...\n');

tic;

% Calculate difference between data and reference
% Find Maxigram and corresponding time gram
ClassicalMaxigram = zeros(Nx,Ny);
ClassicalTimegram = zeros(Nx,Ny);
for px=1:Nx
    parfor py=1:Ny
        deltaT = Tn(px,py,:) - Tref;
        [val idx] = max(deltaT(:));
        ClassicalMaxigram(px,py) = val;
        ClassicalTimegram(px,py) = idx;
    end
end

%-------------------------------------------------------------------------%

%% No Reference Approach
rfMaxigram = zeros(Nx,Ny);
rfTimegram = zeros(Nx,Ny);
Tn = permute(Tn,[3 1 2]);
```

```
t = [1:Nt]';
that = (t - mean(t(:))) / std(t(:));
for px=1:Nx
    parfor py=1:Ny
        coeff3 =  polyfit(t,Tn(:,px,py),3);
        Tl = polyval(coeff3,t);
        coeff6 = polyfit(that,Tn(:,px,py),6);
        Th = polyval(coeff6,that);

        deltaT = Th - Tl;
        [val idx] = max(deltaT(:));
        rfMaxigram(px,py) = val;
        rfTimegram(px,py) = idx;

    end
end

%% Output
outCube(:,:,1) = imnorm(ClassicalMaxigram);
outCube(:,:,2) = imnorm(ClassicalTimegram);
outTags{1} = 'Classical Maxigram';
outTags{2} = 'Classical Timegram';

outCube(:,:,3) = imnorm(rfMaxigram);
outCube(:,:,4) = imnorm(rfTimegram);
outTags{3} = 'Reference Free Maxigram';
outTags{4} = 'Reference Free Timegram';
```

```
DisplayTime(toc);
fprintf('Dynamic Thermal Tomography (DTT) Algorithm Complete!\n')
    ;
```

B.5 Pulse Phase Thermography (PPT)

```
function [outCube outTags ampCube phaseCube] = ppt(imageCube)
% PPT Pulse Phase Thermography algorithm for pulsed thermography
% data. The algorithm uses analogies to modulated thermography
    and the
% Fourier transform to evaluate the amplitude and phase images of
     the
% data.
%
% [Y TAGS AMPCUBE PHASECUBE] = PPT(X) Process 3-D image cube X
    and results
% in Y (finish description). AMPCUBE and PHASECUBE are image
    cubes
% representing the amplitude and phase responses, respectively. X
    , AMPCUBE,
% and PHASECUBE are U by V by W, where U and V are the dimensions
     of each
% image frame and W is the number of frames. TAGS is a vector of
    cell
% arrays containing a text description of each output frame.
%
% Reference Paper(s):
% 1) X. Maldague and S. Marinetti, "Pulse phase infrared
    thermography,"
```

```
% Applied Physics, 1996.
%
% 2) X. P. Maldague, Theory and Practice of infrared technology
    for nonde-
% structive testing. John Wiley & Sons, Inc., 2001.
%
%
% See also POLYSMOOTH, FFT.
%
% PULSED THERMOGRAPHY PROCESSING TOOLBOX
% Author: Cory Andrew Larsen

fprintf('Processing with Pulse Phase Thermography...\n');
tic;

% find dimensions
[Nx Ny Nt] = size(imageCube);
M=Nx*Ny;
imageMat = reshape(imageCube,M,Nt);

% Take Fourier transform
F = zeros(M,Nt);
parfor nn=1:M
        F(nn,:) =  fft(imageMat(nn,:));
end

% Find Amplitude & Phase images
ampCube = reshape(abs(F),Nx,Ny,Nt);
```

```
phaseCube = reshape(angle(F),Nx,Ny,Nt);


outCube = imnorm(phaseCube);
outTags = genNumTags(outCube);


DisplayTime(toc);
fprintf('Pulse Phase Thermography (PPT) Complete!\n');
```

B.6 Time-Difference Contrast (TDC)

```
function [outCube outTags] = TimeDifference(imageCube)
% TIMEDIFFERENCE Subtracts a time difference between every fifth
    image in a
% image cube by first performing a least-squares fit for the
    image
% intensities.
%
% [Y TAGS] = TIMEDIFFERENCE(X) Process 3-D image cube X and
    results in the
% processed output cube Y.  TAGS is a vector of cell arrays
    containing a
% text description of each output frame.
%
% Reference(s):
% Larsen, Cory A. Document Flash Thermography. Master's Thesis.
    Utah State
% University. 2011.
%
%
```

```
% See also POLYSMOOTH, FFT.
%
% PULSED THERMOGRAPHY PROCESSING TOOLBOX
% Author: Cory Andrew Larsen

fprintf('Algorithm Time Difference Beginning...\n');
tic;
addpath('../lib/');

[Nx Ny Nt] = size(imageCube);
options = optimset('Display','off');
I1 = imageCube(:,:,1);

outCube = zeros(Nx,Ny,Nt);
parfor nn=1:Nt
    I2 = imageCube(:,:,nn);
    % Perform Minimization
    hfun = @(alpha)TDfun(alpha,I1,I2);
    alpha = fminunc(hfun,1,options);

    % Remove Negative Values and Contrast Stretch
    Idiff = alpha*I2 - I1;
    method = 2;
    if(method == 1)
        Iout = Idiff;
        Iout(Idiff <= 0) = 0;
        outCube(:,:,nn) = imnorm(Iout);
    else
```

```
            outCube(:,:,nn) = I2+Idiff*alpha;
    end

end

outTags = genNumTags(outCube);
outCube = fixCube(outCube);

toc
DisplayTime(toc);
fprintf('Time Difference Complete!\n');
end

function [f] = TDfun(alpha,I1,I2)
f = norm(alpha*I2-I1)^2;
end
```

B.7 Total Harmonic Distortion (THD)

```
function [outCube outTags] = THD(imageCube)
% THD Total Harmonic Distortion algorithm for pulsed thermography
% data. The algorithm enhances defect contrast by transforming
    each pixel
% sequence in the Fourier domain and evaluating the amount of "
    noise"
% within the signal which is indicative of a defect.
%
% [Y TAGS] = THD(X) Process 3-D image cube X and results
```

```
% in imageCube Y.  Y contains several images including THD power
    definition
% (THDp), THD voltage definition (THDa), and a signal-to-noise
    ratio (SNR)
% image.  TAGS is a cell array containing string descriptions of
    the output
% images contained in Y.
%
%
% Reference(s):
% Larsen, Cory A. Document Flash Thermography. Master's Thesis.
    Utah State
% University. 2011.
%
% See also FFT.
%
% PULSED THERMOGRAPHY PROCESSING TOOLBOX
% Author: Cory Andrew Larsen


fprintf('Algorithm THD Beginning...\n');
tic;
[Nx Ny Nt] = size(imageCube);
M=Nx*Ny;
imageMat = reshape(imageCube,[M Nt]);



% Find Center of Signal
if(mod(Nt,2))
```

```
    C = ceil(Nt/2);
else
    C = ceil(Nt/2)+1;
end

Fpeak = zeros(1,M);
THDp = zeros(1,M);
THDa = zeros(1,M);
SNR = zeros(1,M);
parfor nn=1:M
    % Find Fourier Transform
    I = imageMat(nn,:);
    F = fftshift(abs(fft(I)));

    % Peak Value
    Fpeak(nn) = max(F(:));

    % Calculate Power THD
    P1 = F(C)^2;
    Ptot = sum(F(C+1:end).^2);
    THDp(nn) = Ptot/P1;

    % Calculate Amplitude THD
    THDa(nn) = sqrt(Ptot) / F(C);

    % Calculate SNR???
    SNR(nn) = mean(F(:))/std(F(:));
```

```
end

outCube(:,:,4) = reshape(Fpeak,Nx,Ny);
outTags{4} = 'Peak FFT Magnitude';

outCube(:,:,1) = reshape(THDp,Nx,Ny);
outTags{1} = 'THDp';

outCube(:,:,2) = reshape(THDa,Nx,Ny);
outTags{2} = 'THDa';

outCube(:,:,3) = reshape(SNR,Nx,Ny);
outTags{3} = 'SNR';

outCube = imnorm(outCube);

fprintf('Algorithm THD Finished!\n');
toc
DisplayTime(toc);
```

B.8 Markov Error Contrast (MEC)

```
function [outCube outTags] = MarkovError(imageCube)
% MEC Markov Error Contrast algorithm for pulsed thermography
% data. The algorithm enhances defect contrast by modeling each
    pixel's
% temporal sequence as a Markov chain.
%
% [Y TAGS] = MEC(X) Process 3-D image cube X and results
```

```
% in imageCube Y.  Y contains the resulting contrast images
    created from
% differencing the sequence from the Markov chain estimation.
    TAGS is a
% cell array containing string descriptions of the output images
    contained
% in Y.
%
%
% Reference(s):
% Larsen, Cory A. Document Flash Thermography. Master's Thesis.
    Utah State
% University. 2011.
%
%
% PULSED THERMOGRAPHY PROCESSING TOOLBOX
% Author: Cory Andrew Larsen
tic;
[Nx Ny Nt]  = size(imageCube);
M=Nx*Ny;
imageMat = reshape(imageCube,[M Nt]);

outCube = zeros(M,Nt);
parfor nn=1:M
        T = zeros(1,Nt);
        I = imageMat(nn,:);
        % Calculate Markov Estimate Chain
        T(1) = I(1);
```

```
        for tt=2:Nt
            T(tt) = I(tt-1)*sqrt((tt-1)/tt);
        end

        outCube(nn,:) = I - T;;

end

outCube = imnorm(reshape(outCube,[Nx Ny Nt]));
outTags = genNumTags(outCube);
DisplayTime(toc);
```

B.9 Time Constant Analysis (TCA)

```
function [outCube outTag] = tca(imageCube)
% TCA Finds the time constant of the exponential decay of the
    thermal decay
% signal.
%
% [Y TAGS] = TCA(X) Process 3-D image cube X and results in Y,
    consisting
% of two frames, one containing the amplitude coefficient and the
     other
% containing the time constant image. X is U by V by W, where U
    and V are
% the dimensions of each image frame and W is the number of
    frames. Y is
% U by V by 2. TAGS is a vector of cell arrays containing a text
% description of each output frame.
```

```
%
% Reference(s):
% Larsen, Cory A. Document Flash Thermography. Master's Thesis.
    Utah State
% University. 2011.
%
% See also SVD, FIXCUBE.
%
% PULSED THERMOGRAPHY PROCESSING TOOLBOX
% Author: Cory Andrew Larsen
tic;
% find dimensions
[Nx Ny Nt] = size(imageCube);
M = Nx*Ny;
imageMat = reshape(imageCube,[M Nt]);

% Initialize Fit model
model='a*exp(-x/b)+c';
FT = fittype(model);
t = [1:Nt]';

% Initialize Matrices
Tau = zeros(1,M);
A = zeros(1,M);
% C = zeros(1,M);
parfor nn=1:M
    I = imageMat(nn,:)';
```

```
    % Perform Least Squares Fit
    options = fitoptions('Method','NonlinearLeastSquares');
    options.Lower = [0 1 0];
    options.StartPoint = [.5 7 0];
    F = fit(t,I,FT,options);

    % Get System Parameters
    cv = coeffvalues(F);

    % Save values
    Tau(nn) = cv(2);
    A(nn) = cv(1);
%     C(nn) = cv(3);

end

outCube(:,:,1) = reshape(A,Nx,Ny);
outTag{1} = 'Amplitude';
outCube(:,:,2) = reshape(Tau,Nx,Ny);
outTag{2} = 'Time Constant';
outCube = imnorm(outCube);
DisplayTime(toc);
```

B.10 Matched Filters

```
function [ outCube outTags ] = MatchedFilters( imageCube )
% MATCHEDFILTERS Applies four matched filter defintions to flash
% thermography data set.
%
```

```
% [Y TAGS] = MATCHEDFILTERS(X) Process 3-D image cube X and
    results
% in imageCube Y.  Y contains the images created from the four
    matched
% filter definitions. TAGS is a cell array containing string
    descriptions
% of the output images contained in Y.
%
%
% Reference(s):
% Larsen, Cory A. Document Flash Thermography. Master's Thesis.
    Utah State
% University. 2011.
%
%
% PULSED THERMOGRAPHY PROCESSING TOOLBOX
% Author: Cory Andrew Larsen
fprintf('Running Matched Filters ...\n');


[Nx Ny Nt] = size(imageCube);


%-- Select Pixels from Image and create H, B, and U matrices --%
NumPts = 5;
fprintf('Choose Target Pixels: ');
h = SelectPoints(NumPts,imageCube,1);
pause(1)
fprintf('Choose Background Pixels: ');
b = SelectPoints(NumPts,imageCube,1);
```

```
tic

s = h-b;
st = s';

imageCube = permute(imageCube,[3 1 2]);

% Calc. Data Variances
M = Nx*Ny;
N = Nt;
A = reshape(imageCube,M,N);
Rinv = inv(cov(A));
%-------------------------------------------------------------%
rho = 1/sqrt(st*Rinv*s);
mean_s = mean(s(:));
var_s = var(s(:));
const1 = sqrt(st*Rinv*s);
const3 = sqrt(st*s);

% Initialize Arrays
SAM = zeros(Nx,Ny);
ACE = zeros(Nx,Ny);
tstat = zeros(Nx,Ny); Fstat = zeros(Nx,Ny);
%% Calculate Matched Filter Results
for px=1:Nx
    for py=1:Ny
```

```
            x = imageCube(:,px,py);
            xt = x';

            const2 = xt*Rinv*x;

            % Spectral Angle Map (SAM)
            SMF = st*x;
            SAM(px,py) = SMF / ( const3*sqrt(xt*x) );
            % Clutter Matched Filter (CMF)
            CMF = st*Rinv*x;
            % Adaptive Coherence Estimator (ACE)
            ACE(px,py) = CMF / ( const1*sqrt(const2)  );
            % t statistic
            d = mean_s - mean(x(:)) / ( sqrt( var_s + var(x(:)) )/2 )
                ;
            tstat(px,py) = CMF * rho*sqrt(d-1) / sqrt( const2 - rho
                ^2*CMF^2 );
            % F statistic
            Fstat(px,py) = tstat(px,py)^2;
            %-------------------------------------------------------%


        end
    end

    %-- Store Output --%
    outCube(:,:,1) = imnorm(SAM);
    outTags{1} = 'MF-SAM';
```

```
outCube(:,:,2) = imnorm(ACE);
outTags{2} = 'MF-ACE';
outCube(:,:,3) = imnorm(abs(tstat));
outTags{3} = 'MF-t_Statistic';
outCube(:,:,4) = imnorm(Fstat);
outTags{5} = 'Mf-F_statistic';
%-------------------%
outCube = imnorm(outCube);


fprintf('Matched Filters Processing Complete!\n');
DisplayTime(toc);
end
```